University of Massachusetts Amherst
ScholarWorks@UMass Amherst

Masters Theses | Dissertations and Theses

November 2023

Device Design for Inducing Aneurysm-Susceptible Flow Conditions Onto Endothelial Cells

hans f. foelsche
University of Massachusetts Amherst

Follow this and additional works at: https://scholarworks.umass.edu/masters_theses_2

Recommended Citation

foelsche, hans f., "Device Design for Inducing Aneurysm-Susceptible Flow Conditions Onto Endothelial Cells" (2023). *Masters Theses*. 1372.
https://doi.org/10.7275/35997185.0 https://scholarworks.umass.edu/masters_theses_2/1372

This Open Access Thesis is brought to you for free and open access by the Dissertations and Theses at ScholarWorks@UMass Amherst. It has been accepted for inclusion in Masters Theses by an authorized administrator of ScholarWorks@UMass Amherst. For more information, please contact scholarworks@library.umass.edu.

DEVICE DESIGN FOR INDUCING ANEURYSM-SUSCEPTIBLE FLOW CONDITIONS ONTO ENDOTHELIAL CELLS

A Thesis Presented

By

HANS F. FOELSCHE

Submitted to the Graduate School of the
University of Massachusetts Amherst in partial fulfillment
of the requirements for the degree of

MASTER OF SCIENCE IN MECHANICAL ENGINEERING

September 2023

Mechanical and Industrial Engineering

© Copyright by Hans F. Foelsche 2023

All Rights Reserved

DEVICE DESIGN FOR INDUCING ANEURYSM-SUSCEPTIBLE FLOW CONDITIONS ONTO ENDOTHELIAL CELLS

A Thesis Presented

By

HANS F. FOELSCHE

Approved as to style and content by:

DocuSigned by:
Juan M Jiménez
E366950BE58C4D3...

Juan Jiménez, Chair

DocuSigned by:
Govind Srimathveeravalli
85069377F2594D3...

Govind Srimathveeravalli, Member

DocuSigned by:
Matthew R. Lackner
F54C7DCA58CC414...

Matthew Lackner, Member

DocuSigned by:
Sundar Krishnamurty
3F8496455D304DC...

Sundar Krishnamurty, Department Head

Mechanincal and Industrial Engineering

“[9] What gain has the worker from his toil? [10] I have seen the business that God has given to the children of man to be busy with. [11] He has made everything beautiful in its time. Also, he has put eternity into man's heart, yet so that he cannot find out what God has done from the beginning to the end. [12] I perceived that there is nothing better for them than to be joyful and to do good as long as they live; [13] also that everyone should eat and drink and take pleasure in all his toil—this is God's gift to man.”

-Ecclesiastes 3:9-13

ACKNOWLEDGEMENTS

`

First, I want to thank my loving wife Alison for supporting me in every way throughout my studies. She has been instrumental in not only my degree but every aspect of my life. There is no one in this world I would rather have as a teammate.

I am forever grateful to my parents for their unconditional and persistent love throughout not only my master's degree but my entire life. They have supported me in every way imaginable, and this work would never have been accomplished without their love and support. I would also like to thank all my family and friends for their continual support throughout my time at Umass.

Many thanks to my committee for their support and availability throughout my degree, as well as their clear desire for me to become as good of an engineer as I can be. Specifically, Professor Jimenez for taking the time week after week to ensure my growth and development as a scientist and engineer.

I want to thank the Umass machine shop workers, Rick and Colby, for their continual support when I was machining parts. They were very helpful whenever I had any questions about machining concepts or methods.

Lastly, I would like to thank Kevin Romani for his continual assistance throughout my degree. He took over a challenging role in a difficult time due to the pandemic but has stepped up tremendously and has clarified any question I have ever had regarding any department requirements.

ABSTRACT

DEVICE DESIGN FOR INDUCING ANEURYSM-SUSCEPTIBLE FLOW CONDITIONS ONTO ENDOTHELIAL CELLS

September 2023

HANS F. FOELSCHE

B.S., UNIVERSITY OF MASSACHUSETTS, AMHERST

M.S.M.E, UNIVERSITY OF MASSACHUSETTS AMHERST

Directed by: Professor Juan Jiménez

Aneurysms are a deadly asymptomatic cardiovascular disease that may occur especially where there are bends and bifurcations in the cerebral vasculature. A region where these features are especially prominent is the Circle of Willis (COW) in the brain, where aneurysms are known to occur. In the carotid artery, which feeds into the COW, the Reynolds number of blood flow is typically around 200-500. Even with such a low Reynolds number, turbulent-like flow, or tortuous flow, can occur due to bends, bifurcations and highly pulsatile flow which lower the effective Reynolds number where tortuous flow can occur. Highly pulsatile flow is unsteady flow that is high in magnitude and changes over time.

Endothelial cells (ECs) line the inner wall of the blood vessel and experience the friction force of blood flow. This work is focused on designing a device that can expose ECs to forces they would undergo in an aneurysm-susceptible site. This is accomplished by exposing ECs to physiologically relevant Wall Shear Stress (WSS) and vibrations simultaneously. Vibrations in

the body occur due to flow separation at the vessel wall, which leads to pressure changes. These pressure changes induce vibrations onto ECs.

The fluid flow in the designed Parallel Plate Flow Chamber (PPFC) is laminar to induce a predictable WSS onto the cells, while the vibrations will induce a rapid cyclical force to simulate pressure fluctuations that may occur in vivo. The aneurysm-susceptible flow will simulate a more turbulent-like flow in the carotid artery; higher maximum WSS (around 2.2 Pa) with vibrations. The aneurysm-protective flow will have a lower WSS maximum (around 0.5 Pa).

The PPFC, made of polycarbonate, is small and light enough to be conveniently vibrated using an electromagnetic vibration stage. The PPFC can be driven by a syringe or peristaltic pump, allowing for either steady or transient waveforms. The PPFC's fluid domain will not change upon vibration, isolating the effect of vibration on the cells. Also, two side-by-side glass slide slots were included to allow for both protein and mRNA quantification from the same experiment, increasing experimental efficiency and flow-related consistency between the two cell areas.

Simulations using ANSYS Fluent verified the flow field and WSS waveform on the cells for the designed geometry for 3D and 2D cases, as well as verified equal WSS values throughout all areas of ECs. Then, Particle Image Velocimetry (PIV) was done to verify the predicted flow rate in the machined PPFC given a steady flow rate driven by a syringe pump. Preliminary cell experiments were performed in an incubator under flow and vibration conditions to demonstrate cell survivability.

Table of Contents

List of Tables

List of Figures

Chapter 1

LITERATURE REVIEW

1.1 Introduction

The likelihood that an adult has an unruptured intracranial aneurysm is approximately between 2 and 5% assuming they are otherwise healthy with no other cardiovascular diseases or health conditions.[19,23,60,98,101,120,121] An aneurysm can be defined as an abnormal growth or dilation in a vascular region. Examples of aneurysms in the brain can be seen in Figure 1.1. Unruptured aneurysms can grow and eventually rupture, which is called a subarachnoid hemorrhage (SAH). While unruptured intracerebral aneurysms that are not growing have around a 0.2% chance of rupture, growing aneurysms are 12 times more likely to rupture (2.4% chance).[120]

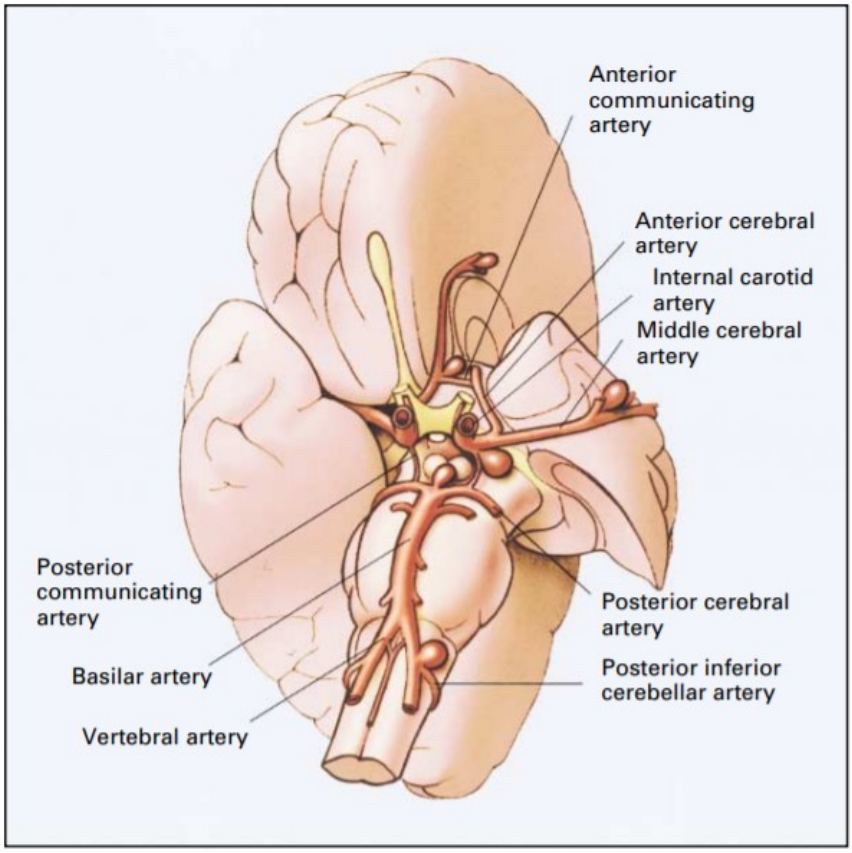

Figure 1.1: Common sites of intracranial aneurysms on the circle of Willis at the base of the brain, from Schievink et al.[98]

SAH can be fatal, and approximately 45% of people who experience a SAH die.[51,60,101,120] Aneurysms can be asymptomatic until rupture, which is problematic due to the high mortality rate upon ruptured aneurysms. The asymptomatic nature of aneurysms makes detection early on in aneurysm development a difficult task, which can lead to a sudden SAH with no forewarning. This also means that getting an accurate number for those with aneurysms is difficult.[107]

Age, sex and genetics (or family history) are other risk factors commonly associated with aneurysm development.[11,22,95,98,107,121] Genetically, one can have autosomal dominant polycystic kidney disease, Ehlers-Danlos type IV, or fibromuscular dysplasia, which have also been associated with the development of cerebral aneurysms, but do not guarantee the existence of aneurysms[19,22,98] It is difficult, however, to correlate

these risk factors to aneurysms, for often times these conditions go undiagnosed, as do aneurysms.[98]

There are also some other factors that are said to play a role in aneurysm development. Cigarette smoking has been the most prominent behavioral factor that has been widely accepted to be related to an increased risk of aneurysm development and even increases risk as much as three to ten times more than non-smokers.[22,96,98] Also, arterial hypertension, or high blood pressure, is a factor that has been associated with the development of aneurysms.[11,96,98] Hypertension can be a behavioral factor, but genetically one can be more likely to have hypertension as well.[15,46,48]

There are a handful of surgical methods to reduce the risk of aneurysm rupture, but they all have a considerable risk to perform and may cause additional harm or risk.[19,43,98] These methods include surgery (clipping, vascular bypass grafting, endovascular balloon occlusion, or hypothermic cardiac arrest) and endovascular therapy (coil embolization).[43,51,82,98]

In a literature review of various endovascular treatments, Naggara et al. found that out of 71 studies of treatments resulted in an overall 1.2% chance of death when or after being treated for an aneurysm.[82] There was also an overall unfavorable outcome rate of 4.8%. An unfavorable outcome was defined as a procedural mortality or disability at 1 month. Although their study did not account for how often each treatment was performed, it still shows how prevalent surgical complications are. Aneurysms are both difficult to detect and treat.

1.2 Aneurysm Locations

1.2.1 Arterial Degradation

Little is known about the direct cause(s) of the formation of aneurysms. However, since aneurysms are abnormalities in the vascular region, it is important to understand how arteries function, how/why an artery may host an aneurysm and how aneurysms can develop and rupture. Human arteries consist of three main layers: Adventitia, media and intima. These three layers consist primarily of collagen fibers, smooth muscle cells (SMCs) and endothelial cells (ECs) respectively. These layers are shown in Figure 1.2.

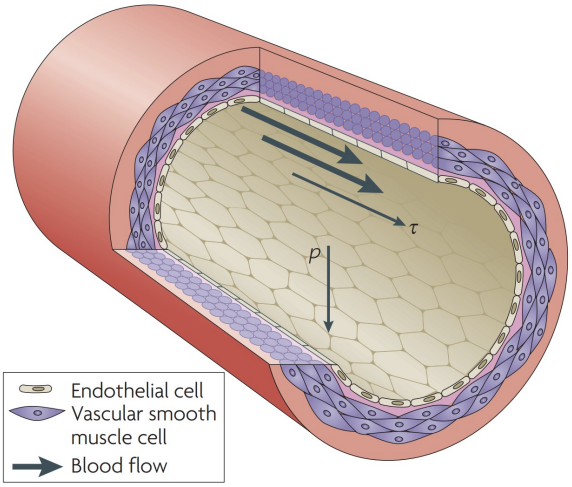

Figure 1.2: Shows the different layers of the artery along with the pressure (p) and shear stress (τ) that act on the ECs. Image from Hahn et al[44]

The muscular tone of the artery is defined primarily by SMCs, and also is the means of which arterial blood pressure is maintained throughout the vasculature.[78,116] The intima is lined by a monolayer of ECs known as the endothelium. It also provides a fairly smooth surface for blood to flow along the blood vessel wall.

A common histopathological finding in aneurysms is the thinning of the layers in arteries, leading to arterial wall degradation. This may lead to a severe lack in structural integrity of an artery, which can lead to abnormal growths, or balloons,

where this thinning occurs.[19,106]

Some studies have found that around the apex (or branch point) of the carotid bifurcation, significant arterial thinning occurred.[21,106] Canham et al. concluded that there is a relationship between the bifurcation angle and the size of the medial gap that appears at bifurcations.[21] This may be correlated to aneurysm development, as the carotid artery has been noted as a location susceptible to aneurysms, and arterial thinning is said to be a known precursor to aneurysm formation.[51,98,121] There was also a notable thinning of the media layer at the entrance of some aneurysms, with a sharp end to the media layer at the aneurysm neck. This thinning and disappearance of the media layer in aneurysms may also be related to how and why aneurysms develop.[106]

The internal elastic lamina has also been said to undergo degradation at a site of aneurysm formation.[79,95,106] The internal elastic lamina, like the media layer, has been reported to end abruptly at the entrance of aneurysms.[106] However, Stehbens et al. reported a loss in internal elastic lamina integrity independent from media degradation, which means the internal elastic lamina may also play an important role in aneurysm development. Others have also reported the importance of elastic lamina in the structural integrity of arteries.[32,95] Circumferentially around arteries and within the elastic lamina region are sheets of concentric cylinders of elastin. Elastin is responsible for most of the stretching and retracting behavior of arteries, as well as in the lungs and skin.[33,80] When an artery degenerates, which is known to happen with age, there can be stiffening of the arterial wall. This could be caused by the elastin, though able to stretch and allow arteries to dilate, wearing over time due to cyclic fatigue.[33] This may cause weakening in arteries, which may make them more susceptible to arterial structural degradation or aneurysms.[6]

Intracranial blood vessels do not have an external elastic lamina.[32,98] The main

structural component of the elastic lamina is elastin, which plays a large role in terms of load bearing of pressure in arteries.[32,33] It is not well known, however, how the lack of an external elastic lamina effects the structural integrity of the blood vessel, or how it may affect aneurysm development. Also, Anwar et al. discussed how circumferential stress may induce aneurysms due to an excessive hoop stress weakening the vessel wall, which is more catastrophic for thinner vessels such as in the brain. The fact that there is no external elastic lamina and thus less elastin and arterial structure in intracranial arteries means that thye may have less structural elasticity than other parts of the body.[95] The structural integrity of an artery may be compromised in aneurysm-susceptible region.

1.2.2 Aneurysms in the Circle of Willis

Some regions where aneurysms in the brain may occur are the basilar artery, carotid bifurcation, internal carotid artery (ICA), posterior communicating artery and the middle cerebral artery trifurcation.[26,63,69,79,98] One study, where a review of 19 different studies were analyzed for pediatric patients who had cerebral aneurysms, found an overall death rate of 28%.[51] They found that the most common location for an aneurysm to occur was the ICA terminus, which occurred in 26% of the pediatric patients studied. The likelihood of developing an aneurysm is much more likely with age.[11,22,95,98,107,121] However, the location in which people develop aneurysms as adults is different than children.[51] Aneurysms are not only a risk for adults, but also for children.

Liu et al. found that out of the cerebral arteries studied, the ICA was where 39.8% of aneurysms were located.[75] Also, out of 280 aneurysms analyzed in the internal carotid artery, 267 (95%) were sidewall aneurysms rather than bifurcation aneurysms.[75] Since there were 353 sidewall aneurysms analyzed in this study, 75% of aneurysms were in the ICA (267 aneurysms). Considering the anatomy of an artery at and near

a bifurcation as well as the aforementioned studies, it makes sense that aneurysms would occur there. However, Liu's finding leads to the idea that something more than strictly the arterial layer structure is at play here. Based on Liu's findings there may be some other influence as to why aneurysms occur at certain locations along the sidewall of certain arteries, such as the internal carotid artery, as opposed to occurrences on an apex of a bifurcation.

These common aneurysm sites in the brain are within the region known as the circle of Willis (COW), shown in Figure 1.3. The circle of Willis is said to develop aneurysms more than other regions of the body due to the plethora of bends, bifurcations and the turbulent-like nature of blood flow that develops in this region. This region also strays from the calculated optimal angle for work minimization according to the optimality principle.[53,107] It is hypothesized that a possible reason for this stray from the work minimum optimality is that there are other factors that play a role in how an artery is shaped other than exclusively fluid dynamics, such as biological developments, that must occur.[53] Figure 1.1 shows a cartoon of the COW in the brain with aneurysm-susceptible sites from Shievink et al.[98]

It should be noted that only around 50% of people will have a complete COW.[5,59] An example of an incomplete COW is shown in Figure 1.4. There can also be other variations of blood vessels in the COW. Some other examples of variations are shown in Figure1.5

In Kapoor's study, where brains from 1000 autopsy subjects were analyzed, all aneurysms found were in the anterior portion of the COW. Kapoor et al. also mentioned that the incidence of aneurysms may be related to the hemodynamic stresses caused by the variations in the COW.[59]

It was originally thought that the COW served as a means of compensating for portions that may not be getting enough blood flow.[113] However, the conclusion of

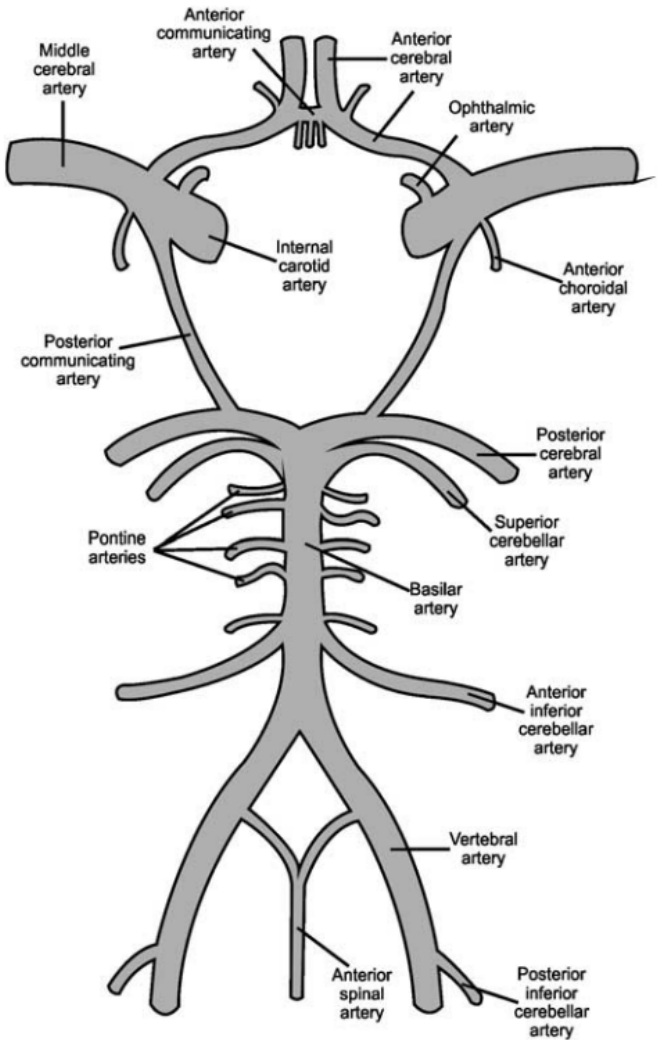

Figure 1.3: Shows the anatomy of the COW, Figure from Vrselja et al.[122]

Vrselja et al. disagrees with this. Vrselja hypothesizes that the communicating arteries are not compensatory for blood flow between the anterior and posterior sides because the communicating arteries are usually too small for effective blood transfer. They conclude that the communicating arteries act as a pressure dissipation system to prevent arterial damage from the asynchronous arrival of pulse waves and blood flow.[122] This agrees with the idea from Kapoor who addresses the potential relationship between increased hemodynamic stresses and aneurysm development. If the purpose of the communicating arteries in the COW is pressure dissipation, there may be consequences of highly pulsatile and higher magnitude flow rates for certain

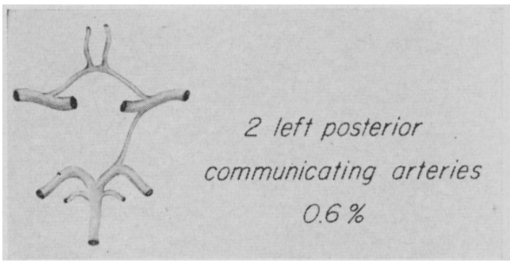

Figure 1.4: Shows an example of a missing posterior communicating artery from Alpers et al.[5]

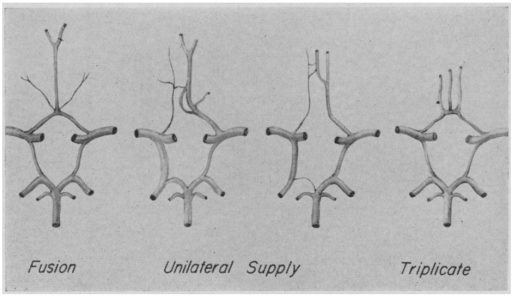

Figure 1.5: Shows some variations of the anterior communicating artery from Alpers et al.[5]

configurations of the COW.

1.3 Hemodynamics

A lot of the aforementioned factors are thought to be be related to the hemodynamics, or fluid dynamics of blood, in specific regions. Aneurysm development must be assessed through not only a purely biological lens, but also from the lens of physics, and more specifically, fluid mechanics. Many studies have emphasized the importance of hemodynamics relating to endothelial cells (ECs) when discussing aneurysm development because ECs are the inner lining of blood vessels that interact with blood flow.[25,30,37,39] ECs are known to change their gene expression based on the blood flow directions and magnitudes they are exposed to which will also affect the other layers of arteries through the release of various enzymes, ions and proteins, known as a signaling cascade.[23]

Endothelial cells function as a barrier between the artery and blood to maintain vascular homeostasis.[89] ECs experience the friction force from the blood flowing through arteries, and that friction force is commonly known as shear stress. ECs will react differently depending on how much shear stress is applied to them, meaning ECs are mechanosensitive.[25,30,37,39] Mechanotransduction is when many intracellular pathways are triggered by the mechanoreceptors on ECs. For example, ECs are known mediators of inflammation, a commonly studied phenotype when studying arterial disease development, like aneurysms or atherosclerosis.[23,25,30]

The two different relevant types of fluid flow that will studied are laminar flow, which is uniform and unidirectional flow, and turbulent flow, which is multi-directional and non-uniform. The inertial and viscous forces are the two factors that play a role in whether the flow is laminar (uniform) or turbulent (non-uniform). When the ratio of inertial forces to viscous forces is very high, the flow will be unstable and multi-directional (non-uniform). This concept is represented by the Reynolds number and is shown in Figure 1.6. It should be noted that the turbulent profile shown in Figure 1.6

is the average profile, and there will be transient deviations from this profile at any given instant in time.

$$Re = \frac{\rho * V * D}{\mu} \tag{1.1}$$

The fluid density is ρ, V is the fluid velocity, D is the diameter of the lumen of the blood vessel and μ is the fluid viscosity. For rigid straight pipe flow, when the Reynolds number is below 2100, the flow is considered laminar. With a Reynolds number over approximately 4000, the flow will be turbulent. When the Reynolds Number is between 2100 and 4000, the flow is known to be transitional, which means there can be both turbulent and laminar flow present simultaneously. Typically, in the carotid artery, which is the focus of this study, the Reynolds number is around 500,[83] which is well within the laminar regime if it is assumed that blood is a Newtonian fluid and arteries are a rigid pipe. However, neither of these assumptions are valid for blood flow, as blood is non-Newtonian and arteries are not rigid.[74]

Blood flow in the body changes over the cardiac cycle, and many studies have shown the importance of pulsatility with blood flow.[108] Stoner et al. discussed how both steady flow and accelerated flow are necessary in order for ECs to function properly in terms of arterial function, and how flow acceleration may be an important stimulus in terms of blood flow and mechanotransduction.

Since blood flow in the body is by nature pulsatile, the Reynolds number is constantly changing throughout the cardiac cycle due to the change in velocity. Also, the arterial diameter changes from person to person (as well as throughout a cardiac cycle), and each section of arteries has a changing diameter, thus also changing the Reynolds number. Therefore, there must be a range of effective Reynolds numbers to consider. The average diameter of internal carotid arteries are typically between 5.11+-0.87

mm and 4.66+-0.78 mm for women and men, respectively.[67]

In terms of blood flow velocity, Hardesty et al. found that out of 11 patients, the average flow rate in the internal carotid artery was 364 mL per minute.[45] However, another study, where four different velocity measuring methods were used, and MRI measured ICA flow rate at 215+-82.82 mL/min.[86] Tuijl et al. recorded ICA flow velocities around the inlet of 25 +-5.2 cm/s mean flow velocity.[118] Tuijl also found that the pulsatility increases from the extracranial portion to the intracranial portion, and then decreases at the more tortuous portion. The pulsatility was calculated by dividing the range of velocities by the average velocity. This may be a useful metric, but may also skew the pulsatility value if the magnitude is very large. Nonetheless, this decrease was discussed to be caused by the tortuous nature of the flow in irregular geometries, dampening the pulsatile effect on the flow.

Because of the pulsatile nature of blood flow discussed, there is a wide range of Reynolds numbers that characterize carotid artery flow. Based on the aforementioned numbers for flow rate and velocity, a typical Reynolds number would be around 200-450. Kerber found from their in vitro silicone models a maximum Reynolds number of about 200 for their models of the carotid artery,[64] which is considerably lower. It should also be noted that the viscosity of blood does not change as much as velocity or diameter, but it is not constant, as blood is a non-Newtonian fluid.

Pulsatile flow, while necessary for proper EC function, can also have a peculiar effect. When flow decelerates, flow is known to become more unstable, such as at the end of systole of the cardiac cycle.[1] Straatman et al. noted that both the frequency and amplitude of pulsatile flow can each separately affect flow stability.[109]

Because of the anatomy of blood vessels specifically in the brain, which include many various bends, bifurcations, and perturbations within arteries, using a straight pipe assumption for the Reynolds number equation is inaccurate.[4,74,79,102,105] Flow may

appear to be turbulent within arteries even though the conventional Reynolds Number would predict laminar flow.[94,105] Pulsatile flow has been shown to have a similar effect, where turbulent-like flow occurs at lower Reynolds numbers than would occur at steady flow.[94,105,129] Also, torsion has been found to have a destabilizing effect on flow.[131]

Roach et al, with glass models, studied the importance of hemodynamics in bifurcations within the circle of Willis, where vessel bifurcations, flow instabilities and aneurysms are known to occur.[94] One of the aneurysm models is shown in Figure 1.7. They found that flow pulsatility and a higher bifurcation angle both independently decreased the critical Reynolds number where they began to see flow instabilities in their models. This means the flow appeared to be turbulent at a lower Reynolds number than the classically defined turbulence regime. They also found that these two aspects, bifurcation angle and velocity fluctuations, combined for an even greater reduction in the critical Reynolds number. These results are shown in Figure 1.8. They also found that with their aneurysm models, flow instabilities occurred much sooner both in and around the aneurysm, at a Reynolds number of 500, which is a common Reynolds number used in simulating flow in the carotid artery.[83,94] The flow instabilities can also be seen in Figure 1.7, where the flow is not uniform. Roach et al. also found that, even at low Reynolds numbers of 500, there was significant flow separation at bifurcations, meaning there were vortices within their models.[130]

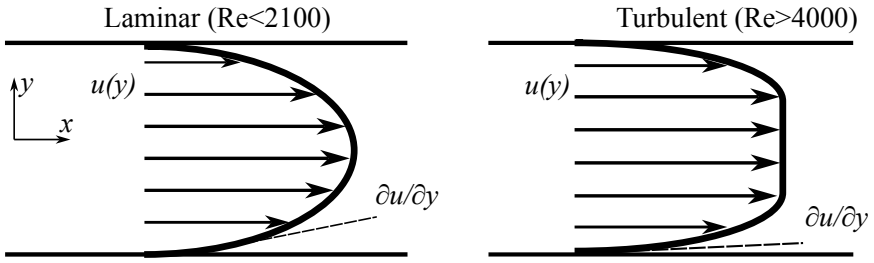

Figure 1.6: Shows the difference between laminar and turbulent flow in a rigid pipe. Laminar flow is more parabolic with a lower velocity gradient near the wall, while turbulent flow has a higher velocity gradient near the wall.

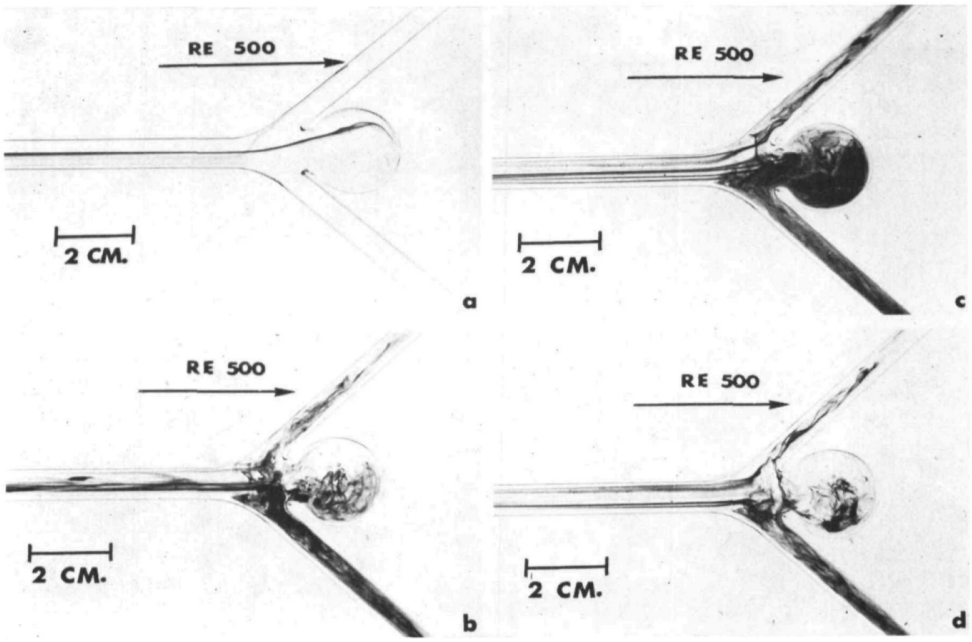

Figure 1.7: Aneurysm glass model from Roach et al.[94]

A similar study by Stehbens et al. showed how the geometry of a fluid domain can influence the Reynolds number where flow instabilities occur. The idea that geometry influences the Reynolds number where turbulence occurs has been studied for at least a century,[41] showing that this idea is by no means a new development, but rather a fundamental component of fluid dynamics applied to a biological perspective.

One feature of typical turbulent flow is the high gradient of velocity near the walls, which is called wall shear stress (WSS). A large difference between the velocity of a fluid and a wall creates what is known as a boundary layer, or shear layer. It has been shown that within the brain, blood flow can be highly unstable.[94,129] As aforementioned, a characteristic of flow instabilities is a higher WSS or WSS gradient. These have also been suggested to promote aneurysm formation.[4,23]

Based on the aforementioned studies, it is known that geometry plays a role in the fluid dynamics of blood vessels. It is also known that even steady flow can have flow separation on the wall of irregular geometries.[24,35,73,112] Flow separation causes

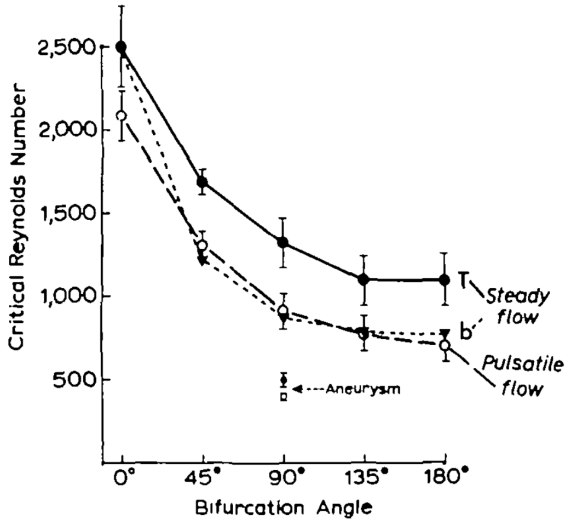

Figure 1.8: From Roach et al.,[94] Shows the effect of a bifurcation angle in glass artery models on the critical Reynolds number, where flow instabilities are visible in the glass models. The critical Reynolds number is synergistically lowered with bifurcation angle and pulsatility.

vortices to develop at the wall of a vessel, which will induce local pressure gradients along the vessel wall causing vibrations.[14,20,42,49,57,126,134] Vibrations within arteries may lead to arterial damage.[29,66] Vibrations in the vessel wall may occur due to fluid flow through the irregular geometries of blood vessels. Pulsating flow, along with the bending and splitting geometry of arteries in the brain, are much more susceptible to these vibrations due to the critical Reynolds number being substantially lower than that of a straight pipe.[94] Not only this, but external forces such as power tools or even snoring may cause vibrations to the endothelium.[7,28,50,62,125]

Blood vessels experience two main forces due to blood flow; shear stress from the flow of blood, and vibrations of the vessel wall from pressure fluctuations. Pressure fluctuations caused by flow separation in regions of unsteady flow have been shown to cause poststenotic dilation caused by deformed elastin.[17] Also, Curry et al. showed that prolonged vibration exposure can induce blood vessel deformation, which can compromise arterial function.[29] Also, vibration has been shown to induce vasoconstriction,[103] which decreases blood flow through the vasculature.[117]

Because of the anatomy of the brain and cerebral blood flow conditions, where there is a plethora of bends and bifurcations of arteries causing more unstable flow, there are natural vibrations that will occur due to local pressure fluctuations. This will play a role in endothelial cell function because ECs not only react to friction force, but also the compressive/expansive force, which is sometimes referred to as strain (or cyclic strain).[9]

There are two main methods to test how strain induced via acceleration will affect cellular phenotype changes; vibration acceleration and centrifugal force via centrifuge.[2,10,40,114,123] The similarity between these two methods is that there is a defined induced acceleration, either centripetal/centrifugal or linearly oscillating, each of which has been used as an independent variable to test ECs for differential gene expression. Since ECs are mechanosensitive, it is important to consider the forces cells would experience under these two conditions.

A centrifuge has been used in a study by Yang et al. who exposed rats to a centrifugal force and fed some rats a high-fat diet. The effects of acceleration and the high-fat diet were both found to decrease the nitric oxide level as well as decrease eNOS expression.[133] They found that there was a slight decrease, but not statistically significant, in blood vessel relaxation when exposed to a centrifugal acceleration of 10 g, which is about 98.1 m/s^2. However, the rats that were fed a high-fat diet and were centrifuged had a synergistic decrease in vessel relaxation in the thoracic aorta that was statistically significant. Also, they found that there was, again, a slight but not statistically significant decrease in eNOS expression between the control and either the high-fat diet or centrifuged rats. The rats that were fed a high-fat diet and exposed to centrifugal forces had a statistically significant decrease in eNOS expression. This is shown in Figure 1.9.

They also showed that with rats exposed to only the centrifuge, there was a significant

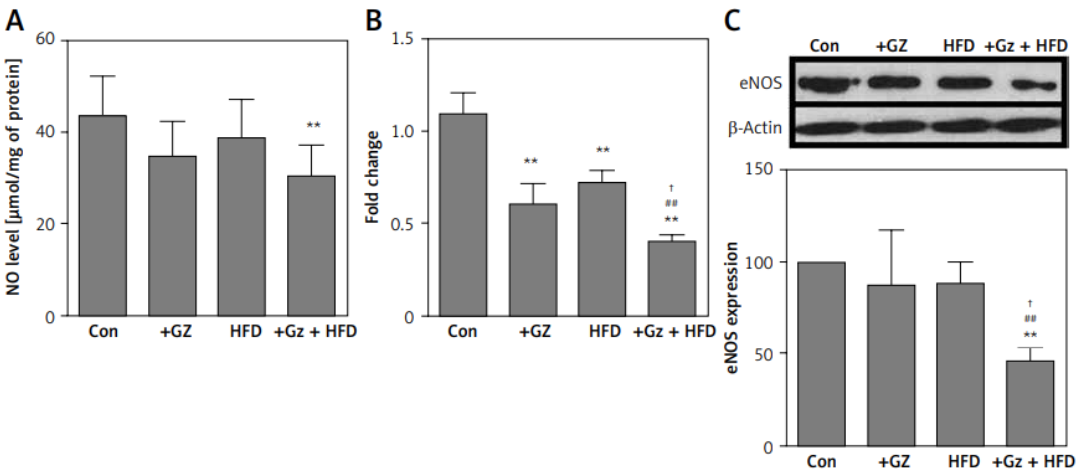

Figure 1.9: Results from Yang et al.[133] **A** shows the NO content in the aorta. **B** shows the mRNA expression of eNOS in the aorta. **C** shows the protein expression of eNOS in the aorta detected using Western blotting. +GZ represents the centrifuged specimens, HFD represents the high-fat diet specimens, and +Gz + HFD represents the specimens that were both centrifuged and fed a high-fat diet.

increase in IL-6 and ICAM-1, which are inflammatory markers. It may be that the very brief exposure to the centripetal force (30 seconds per session, 3 sessions per week for 8 weeks) at a time-limited the effect on the rats. Nonetheless, centrifuging rats in this study has been shown to induce significant dysfunctional changes to the rat aorta.

Furthermore, Wehland et al. compared the effect of altered gravity and induced vibrations.[124] The two conditions were tested in a centrifuge at 1.8 g and up and down vibrations with a max acceleration of 1.8 g. There were some similarities in the results, such as a downregulation of VEGFA and CDKN1A, which are known to be stimulated by stress. In this case, stress is in the perpendicular direction (or normal vector), which is pressure. However, some proteins, such as pan-actin or Ezrin, were upregulated by vibration and unchanged by the centrifuge. This shows that the oscillatory acceleration motion has a different effect on ECs than constant acceleration. Vibration must, therefore, also be investigated for its physiological relevance and effect on ECs.

The endothelium, lining all blood vessels, including those of the brain, has shown discontinuity and degradation from induced vibrations.[29] In a study where 40 rats had their tails vibrated four hours a day for nine days, there was significant deformation on the endothelium and the vessel lumen. This abnormality was not only within the EC monolayer but also SMCs, which expressed more of a migratory phenotype. There was also thinning of the blood vessel wall. They found that early arterial injury involves vasoconstriction and deforming the arterial endothelium.

Uryash et al. vibrated a whole rat horizontally and found that under periodic whole body vibration with a peak acceleration of 2.9 m/s^2, the rats' mean blood pressure decreased, but the ratio between the peak amplitude and first valley magnitude was increased.[117] They also found that under induced vibrations of 100 Hz, there was a significant increase in eNOS level from the control. This differs from Yang et al's findings, where a centripetal force induced a slight decrease in eNOS. This could be due to the constant and oscillatory vibrations that each of the studies used by Yang and Uryash respectively.

White et al. found that the activation of ERK1/2 was linearly increased in HUVECs when the frequency of vibrations was held constant at 30 Hz, and the accelerations of 1 g and 2 g were compared.[125] Krajnak found that rat tails vibrated with a constant acceleration of 49 m/s^2 with ranging frequencies of around 30-250 Hz and yielded a constricting effect on the smooth muscle cells in arteries.[66] This emphasizes the idea that pressure fluctuations causing vibrations also play a role in the mechanosensitive activation of ECs in addition to WSS.

However, it has not been defined how specific amplitudes or frequencies relate to EC dysfunction. There have been studies that show different oscillating pressure/vibration conditions inducing various changes to ECs, such as activation of ERK1/2 and eNOS,[8,9,52,65] but there is not, to the author's knowledge, any specific combination for where dys-

function will begin to occur based off of just amplitude and frequency of induced vibrations. One way to confine both amplitude and frequency into one variable would be to use acceleration as the defining parameter. Acceleration of oscillating waves is commonly defined as follows:

$$Acceleration = Amplitude * (2 * \pi * f)^2 \tag{1.2}$$

where f is the frequency in Hz.

A centrifuge will induce acceleration continuously. Vibrations, on the other hand, induce a periodic acceleration, usually defined by the maximum acceleration, in a oscillatory manner. Vibration acceleration is more relevant to ECs, as they are constantly moving and accelerating at varying rates as opposed to continually experiencing a large constant force for extended periods of time.

Wang et al. shows that there is a linear relationship between acceleration and cell displacement, shear, and strain in an osteoblast computational analysis.[123] Although this was a somewhat idealized model (isotropic solid), it shows how both normal stress and strain, which are induced on ECs by pressure and pressure fluctuations, may be linearly related to the maximum acceleration of vibrations.

Goenka et al., however, showed that even under the same acceleration, there was a significant difference between experiments for bone cells. They had two experimental conditions, each with max accelerations of 49 m/s^2. One set of mice was exposed to 125 Hz and the other to 250 Hz, and the corresponding amplitudes of vibrations according to Equation 1.2 were around 80 and 20 microns for 125 and 250 Hz respectively. They found that there was a statistically significant difference between the control and the two vibration frequencies for nitrotyrosine,[40] which is a known marker for cell damage and inflammation.[81] Also, the higher frequency caused a

slightly higher nitrotyrosine level, although this was not statistically significant. This shows that acceleration may very well play a role in arterial damage, but there are likely other factors than just vibration acceleration.

This can be at least partially explained by one of the findings of Bacabac et al. They found that the jerk, or the rate of change of acceleration over time, was linearly correlated to the amount of NO and PGE_2 produced by bone cells rather than just amplitude and frequency of vibrations.[10] It is well known that ECs are mechanosensitive and therefore react to strain, and it would make sense that EC gene expression correlates more with the change in pressure, which can be directly related to the change in acceleration from a physics perspective because force is proportional to pressure, as are their respective derivatives over time. Goenka et al.'s results would align with this idea, how the greater the jerk, the more of a mechanosensitive effect will be induced on the cells, causing an increase in cell damage and/or inflammation. Thus, the time derivative of acceleration may be a good parameter along with acceleration to guide this study's experimental setup. It is also important to note that the periodic acceleration due to vibrations is also correlated with the displacement, stress, and strain in a linear manner.[10]

It is more realistic to assume a more periodic acceleration of pressure and pressure gradients because pressure by nature acts perpendicular (or normal) to the local cell surface and is constantly changing under physiological blood flow. This means that it is more reasonable, when discussing the effect of pressure fluctuations due to turbulent-like flow, to implement vibrations rather than a constant centrifugal force.

1.4 Endothelial Cell Mechanotransduction

Inflammation is said to play a large role in arterial dysfunction, which can originate from disturbed blood flow conditions that cause an inflammatory phenotype expressed

by ECs.[23,25,39,85] Healthy ECs will be anti-coagulative and anti-thrombotic.[89] Many have studied the effect of shear stress on ECs.[30,36,37,55,108,128] EC dysfunction can also occur when vibrations are induced on ECs.[72,123,125] This can change the delicate characteristics of ECs, such as cell-to-cell junction adhesion, cell proliferation and migration, cell survival, cell orientation and cell signaling.[30,34,39,76,119]

These traits are shown by Dai et al, who demonstrated a difference in gene expression based on different blood flow waveforms in the brain.[30] In this study, two different waveforms are analyzed; athero-protective and athero-prone. These regions were defined as locations in the carotid artery that were 'resistant' and 'susceptible' to atherosclerotic lesion development. In athero-prone regions, it was hypothesized that atherosclerosis is more likely to develop. In that study, they found that the region that experienced athero-prone flow had an upregulation of inflammatory genes than the athero-protective region, such as IL-8, CLDN11, PTX3, MCP-1 and PGF, which are considered to be inflammatory markers.[30,58,85]

ECs response to the mechanical environment instigates much of the function of an artery, which can be severely consequential when ECs are not functioning properly.[54] For example, when ECs express an inflammatory phenotype, this will consequentially affect smooth muscle cells, which maintain the vascular tone as well as maintain blood pressure throughout the vasculature.[3,13,27,61,87,93] Nitric Oxide (NO) also has a key impact on the functionality of arteries as a vasodilator and has been studied in relation to aneurysm development.[18,56,91,99,115,132] Endothelial cells emit NO in the form of endothelial NO synthase (eNOS),[31,38,88] which is also sometimes referred to as Endothelium-derived hyperpolarizing factor (EDHF). Regulating endothelial permeability is another function of eNOS.[90] EC function is vital for proper arterial function.

1.5 Hemodynamic Testing Methods

1.5.1 Flow Chambers

There are many fluidic devices to test endothelial cell genetic expression based on flow exposure. Two common devices used for this application are the Parallel Plate Flow Chamber (PPFC)[77] and the Cone and Plate Viscometer (CPV).[30,36,100] A PPFC is based on Hele-Shaw flow principles for parallel-plate flow, which is flow between two flat parallel plates where the width is so large compared to the height that the flow is uniform away from the walls.[47] In the context of fluidic devices focused on EC flow exposure, a PPFC is typically used to induce laminar flow onto ECs, which will experience respective shear stress from the flow.[70,77] This device is much simpler to design and manufacture, and calculating the shear stress that the cells will experience based on flow rate is well-defined. An example of a PPFC used in this context is Song et al, who found significant elongation of ECs exposed to higher WSS values when compared to cells exposed to low WSS values.[104] A limitation of PPFCs is the difficulty of inducing pulsatile flow that accurately mimics the physiological shear stress waveforms that ECs experience. A PPFC can induce unsteady waveforms when driven by a peristaltic pump, but peristaltic pumps are typically not as robust in terms of inducing highly precise and pulsatile waveforms as a CPV.[70] A CPV is driven directly by a motor, which can yield highly transient WSS waveforms. For this reason, the CPV seemed like a more reasonable device for this application. An example of a CPV is shown in Figure 1.10.

Sdougas et al. was one of the first to define many measurable parameters of a CPV, such as the shear stress based on cone rotational speed and the flow characterization parameter, $\widetilde{R}$.[100] The flow characterization number is similar to the Reynolds number, which defines whether the flow will be laminar or turbulent. Equation 1.3

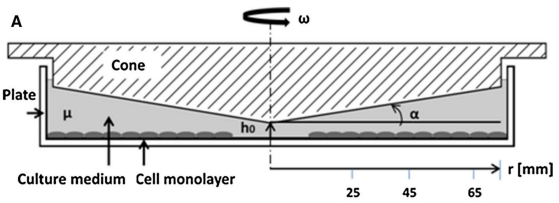

Figure 1.10: A 2D Sketch of a CPV geometry from Franzoni et al.[36]

is the equation derived by Sdougos for the shear stress on the bottom plate, and Equation 2.20 is derived for $\widetilde{R}$.

Sdougos found that when the parameter $\widetilde{R}$ was less than 0.5, the flow would be tangential and laminar under the cone. When the flow is between 0.5 and 4, there would be significant radial secondary flows in the system. Above an $\widetilde{R}$ value of 4, the flow transitions to turbulence.

It should be known that Equation 1.3 is very limited, as there should physically be a gap height between the apex of the cone and the bottom plate, or else damage to the cone, plate and/or cells seeded on the plate may occur. Therefore, Equation 1.3 has been further modified to incorporate a fluid gap between the apex of the cone and the bottom plate for a more practical application in Equation 1.4.[110]

Another incentive to using a CPV is that there is an assumed constant shear rate due to the shallow cone angle.[100] This enables the use of the small angle identity for the shear stress derivation, which allows a direct proportion between the angular velocity of the cone and the shear stress of the bottom layer of cells. For this device, a motor with a controlled angular velocity can yield a predicted shear stress value that ECs cultured on the bottom plate will experience. However, the model for shear stress derived by Sdougos et al. is only valid when $\widetilde{R}$ is less than 0.5, where the flow is purely tangential and laminar. When $\widetilde{R}$ becomes greater than 0.5, there will be significant secondary flow, which will affect both the magnitude and direction of WSS that the cells will experience.

There are a few assumptions that have been made in deriving the above expressions. For one, it is assumed that the fluid is incompressible, and the fluid is non-Newtonian. This means that the volume of the fluid and the viscosity will be a constant value for any calculations and simulations. Also, a no-slip condition is assumed at the boundaries. This means that there will be an assumed fluid velocity of zero at the bottom (stationary) walls. At the cone, the fluid will be moving at the same velocity as the cone. It is also assumed that there is no change in thermal energy throughout the system. Although this does not exactly mimic the environment of the carotid artery in vivo, it greatly simplifies the model while still yielding a direct analysis of the effect of WSS on ECs.

Bataineh et al. analyzed the effects of secondary flow on CPVs and how they relate to $\widetilde{R}$, as well as the effect of the edges of the CPV on the flow field. They found that there are significant effects of the edge boundaries on the flow field, but those effects decrease further from the wall. Also, they observed that a smaller gap height between the cone apex and the bottom plane will yield a more consistent WSS value throughout the fluid domain under the cone.[12]

$$\omega = \frac{\tau * \alpha}{\mu} \tag{1.3}$$

$$\omega = \frac{\tau * (h_0 + r * \alpha)}{\mu * r} \tag{1.4}$$

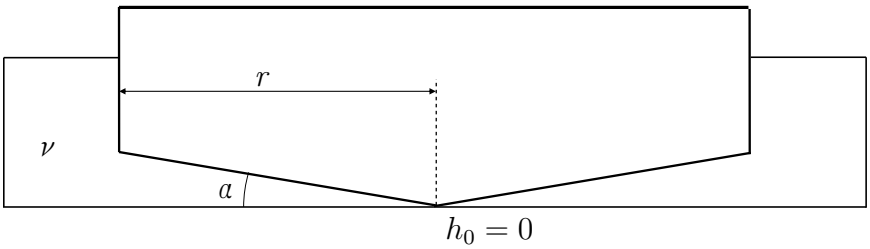

Figure 1.11: CPV geometry with no gap height ($h_0 = 0$), corresponds to Equation 1.3.

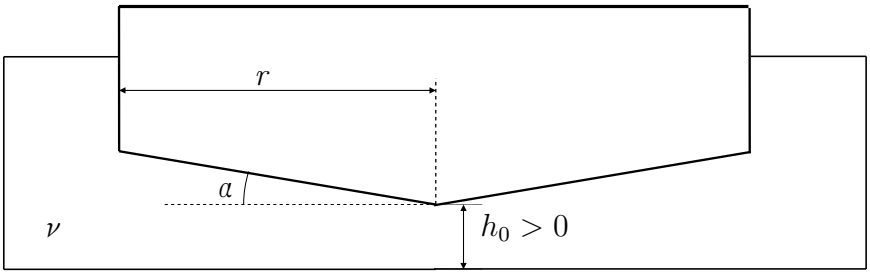

Figure 1.12: CPV geometry with a gap height ($h_0 > 0$), corresponds to Equation 1.4.

Equation 1.3 is applicable for a CPV where the cone tip is touching the base where the cells are hosted. This setup is shown in Figure 1.11. This is an idealized model, for there are few physical applications where the cone tip is touching the base with no frictional effect or adverse effect on the cells. Therefore, the second equation, Equation 1.4 was derived given that a fluid height will exist which is shown in Figure 1.12. The second equation, like the first, demonstrates the relationship between ω to τ. The other variables are held as constants for most experiments for this application.

The PPFC, as aforementioned, is a device that is simpler to design and fabricate but does not typically yield as transient of a waveform to ECs as a CPV because it is usually driven by a syringe pump or a peristaltic pump. The main trade off between a PPFC and CPV is that a PPFC is much easier to design, fabricate and assembly while a CPV is capable of more complex unsteady waveforms. Since one of the main goals of this work is to have the capability of producing complex waveforms, the CPV will be analyzed and designed. Also, vibrating the device is necessary to best mimic the environment of the ECs, which will play role in the analysis and design process. For additional examples of PPFCs, Nidadavolu et al. provides a review of various designs of PPFCs and their application.[84]

1.5.2 Computational Fluid Dynamics (CFD)

To better understand the temporal and spatial effects of a CPV, Computational Fluid Dynamics (CFD) is used. CFD allows the user to simulate a flow field by approximating a solution to the equations of motion. It is advantageous to visualize and quantify how flow develops and changes spatially and temporally. Data points can also be taken at any location among the fluid body to track any parameter over time, such as velocity, pressure, and/or shear stress. These data are much more difficult to obtain, as they require calibrated devices, such as MRI devices.

Something to note with CFD simulations, however, is that they must be set up properly, and adequate attention must be put into the setup and execution of each simulation. It may seem simple or trivial to run a simulation, but if care is not taken to set up a simulation properly, the results are not as meaningful. There are many studies that have used CFD to simulate a CPV device.[12,36,92]

There are some gaps in the literature for how these simulations are set up and executed. Few articles have given details on their solver method (SIMPLE, PISO, etc.), or residuals and why they chose them. These are critical aspects of CFD that seem to be overlooked by most current research in the field. The reason for the lack of detail is unknown.

One study, which will be replicated for a proof of concept for this work's simulations, provided information about how they set up their simulation, and how they got their results.[36] Their first step was using the results from a previous study by Dai et al., which was previously discussed. They then described some of the meshing and solver details, but not enough detail to replicate their work.

In this study by Franzoni et al, they tested whether their CFD results math with a physical CPV, and compared the results for both athero-protective and athero-prone waveforms. They used two different equations throughout the study; both of which correlate the rotational speed of the cone to the WSS the ECs experience. One equation, labeled in their study as Equation 1 (Equation 1.3 in this work), does not account for the cone height above the cells. Equation 2 (Equation 1.4 in this work) is the equation that does account for cell height. Both of those equations are only valid when there is no secondary flow present, where the flow is purely tangential as previously discussed.

Franzoni used Equation 1.3 to calculate the rotational speed needed to apply the WSS from Dai et al. to their ECs. They also used this as their CFD rotational speed

input. This input is also what they used for their physical CPV.

For their analytical methodology, they started with the rotational speed input that was used in their simulation, calculated from the WSS waveform from Dai et al. using Equation 1.3. Then, for their analytical WSS result, calculated the WSS with Equation 1.4, using the rotational speed values from the input from their simulation. This led to a very close match between their computational and numerical model.

They also included in their results their physical CPV device EC orientations. This gives their results some validity in the sense that the atheroprotective waveform yielded more aligned cells, and the atheroprone waveform yielded EC that were not as aligned. Also, for the atheroprotective waveform, the ECs were more aligned over the course of the 48 hour experiment.

However, there seems to be a flaw in their methodology when comparing their CFD results to their analytical solutions. For both the CFD and analytical solution, they started with the WSS from Dai et al., and calculated the rotational speed of the cone using Equation 1.3. This is not correct, for there is certainly a fluid height, as they clearly stated in their methodology. They should have used Equation 1.4 for this step.

Also, after they obtained their rotational speed for the cone, which is the same for their CFD and analytical model, they used two different equations to find the WSS. They used Equation 1.3 for their rotational speed input for their CFD simulation, which would overestimate the actual value of WSS that the cells would experience, for the fluid height is neglected.

Then, for their analytical solution, after using Equation 1.4 to calculate the rotational speed, they used Equation 1.4 to recalculate the WSS. They should have compared their CFD simulation to the WSS waveform from Dai et al, as that is the data they were trying to compare. Although their results seem like they match very well, their

methodology is seemingly flawed and these limitations should be taken into account. However, their main results in terms of verifying the transient capabilities of a CPV, as well as the cell morphology of ECs is still valid. Overall, Franzoni et al. did have a methodology and results that were well described and explained, which is necessary and helpful when performing experiments and running simulations to verify the use of these methods. It should be noted that the only reason these issues were noticed is because Franzoni did a good enough job describing the methodology so that it could be analyzed and reproduced, which is quite beneficial.

Ramadan et al. used CFD to simulate a cone and plate viscometer and had a better description of their meshing analysis and simulation setup.[92] First of all, they did well in describing the 3D model and exactly how it was made, how the meshing was defined, and how the setup was performed. They also gave detailed information on what solution methods were used for their simulation. They gave a well-detailed description of the decision-making for the simulations, which is helpful when trying to replicate one's work and also improve the field. They also showed, for their CPV, a mesh independence study, which is necessary to show any validity to a CFD model. They also compared their CFD results to other's CFD results and mathematical models, further validating their methodology.

However, they did not compare their results with a physical device. While they did validate their methods in a couple of ways, the results may not completely represent reality due to various assumptions made, both computationally and mathematically. While they did use physiologically relevant values for WSS applied to ECs using a CPV, they did not use physiologically relevant waveforms, only general magnitudes and oscillatory trends. Nonetheless, their results are helpful in terms of understanding how shear rate and rotational cone speed are related, and they did provide some sufficient detail about their setup.

Another common gap in the scientific literature is the studies that only analyzed steady flow for a CPV.[16,127] This is by no means a valid assumption for arterial blood flow, for there are surely temporal changes in flow throughout the cardiac cycle. This is a necessary component to analyze the genetic expression of ECs under physiologically relevant waveforms, and should therefore be relevant to any CFD simulation mimicking a physiologically relevant cardiac cycle.

Sucosky et al. were among the first to implement a numerical model where the gap height is accounted for.[110] Sdougos et al. detailed how a CPV is useful for applications where the shear stress is constant while having both laminar uniform flow as well as secondary flow toward the outside of the cone. However, Sucosky et al. manipulated the dimensions so that only laminar flow is induced in the device, eliminating secondary flow. CPVs are versatile for transient applications as well as inducing purely uniform flow, as well as predictable secondary flow.

One of the limitations of Sucosky's work with respect to our aims is that they used a sinusoidal flow pattern, which is much more physiologically accurate than a constant flow pattern, but does not finely mimic the flow of a typical cardiac waveform in terms of acceleration. Also, they did not measure or verify the WSS on the cell surface, only estimated based on the cone velocity measurement.

A major gap in the literature that this work aims to address is the effect of both physiological WSS and vibrations that are simultaneously induced onto ECs in vivo. Only understanding one of these two, shear or vibrations, can lead to dangerous conclusions as they both will have their own effects on ECs, and it has not yet been shown what the effect of inducing both onto ECs would be.

Chapter 2

METHODS

2.1 Wall Shear Stress Waveforms

The goal of this work is to design a device that can induce a physiologically relevant shear stress waveform and vibration condition to ECs that mimics an aneurysm-susceptible site, and compare that to an aneurysm-protective site. This will give insight to how fluid flow may play a role in the early stages of aneurysm development. This involves mimicking both the shear stress that the cells experience, as well as vibrations that the cells experience in vivo, which may occur from rapid acceleration, turbulence or pressure fluctuations. The first step to do this is to gather the two distinct WSS waveforms. This is done with previous work of our lab where patient specific aneurysm models of the ICA were modeled and simulated. Also, the aneurysm for each model was computationally removed, and the aneurysm site was smoothed over as seen in Figure 2.1a. The results from those CFD simulations have not yet been published.

The two distinct waveforms were taken from the two regions highlighted in Figure 2.1a. The orange highlighted region is where the aneurysm was computationally

removed, and the blue highlighted region is where steadier laminar flow is known to occur, which will serve as a control. Then, the average WSS values of those regions were taken as the WSS waveforms for their respective regions. These waveforms are shown in Figure 2.1b.

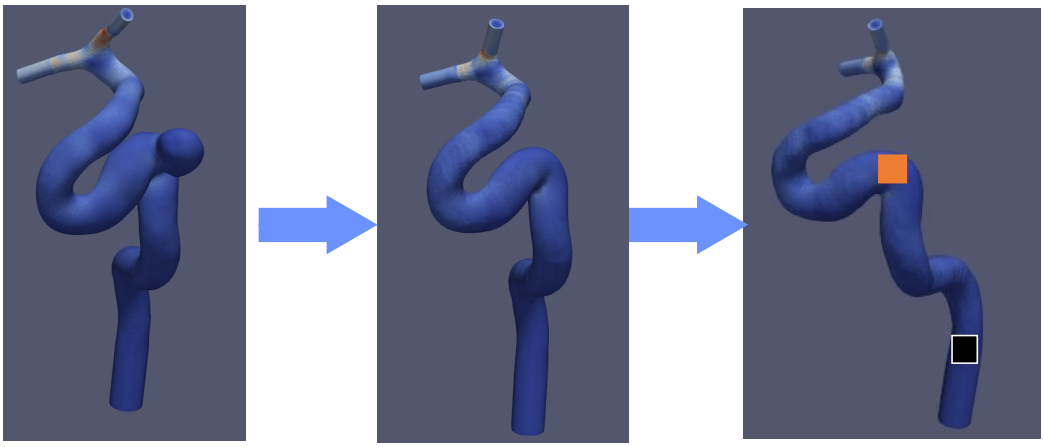

(a) An aneurysm from patient-specific data was computationally removed and smoothed over. Then two regions of distinct flow conditions where the WSS waveforms will be analyzed. The orange square is the aneurysm-susceptible site, and the black square is the aneurysm-protective (upstream) site.

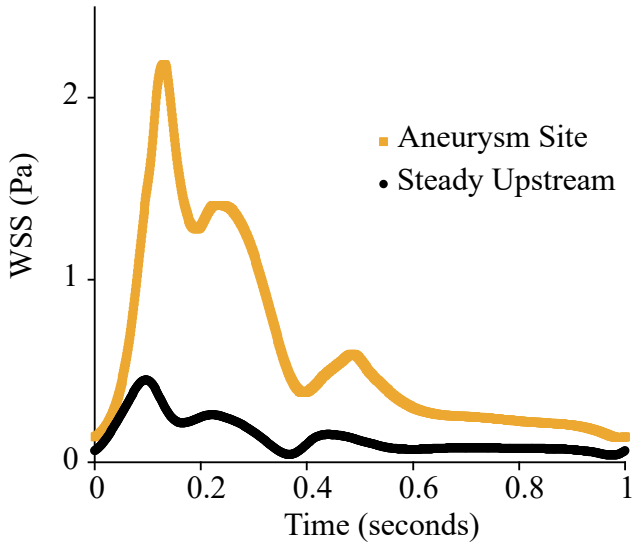

(b) Spatially averaged transient WSS waveforms for the steadier upstream and aneurysm locations.

Figure 2.1: WSS waveforms of the steady upstream site and site where an aneurysm was computationally removed.

2.2 Cone and Plate Viscometer Analysis

2.2.1 CPV Numerical Analysis

The first device that was analyzed was the Cone and Plate Viscometer (CPV) due to its ability to induce highly transient WSS waveforms that best mimic blood flow in the carotid artery.

The input to the CPV CFD simulations will be the transient rotational speed of the cone which will induce a predictable WSS onto the cells. In order to verify the derived equation for the shear stress τ that endothelial cells will experience based on the rotational velocity of the cone, we will start with the viscous stress tensor. Cylindrical coordinates should be used due to the geometry of the CPV. The viscous stress tensor in cylindrical coordinates is defined as follows.

$$\sigma = \begin{pmatrix} \tau_{rr} & \tau_{r\theta} & \tau_{rz} \\ \tau_{\theta r} & \tau_{\theta\theta} & \tau_{\theta z} \\ \tau_{zr} & \tau_{z\theta} & \tau_{zz} \end{pmatrix} \tag{2.1}$$

If we expand each component of the viscous stress tensor we get

$$\sigma = 2\mu \begin{pmatrix} \frac{\partial u_r}{\partial r} & \frac{1}{2}\left(\frac{1}{r}\frac{\partial u_r}{\partial \theta} + \frac{\partial u_\theta}{\partial r} - \frac{u_\theta}{r}\right) & \frac{1}{2}\left(\frac{\partial u_r}{\partial z} + \frac{\partial u_z}{\partial r}\right) \\ \frac{1}{2}\left(\frac{1}{r}\frac{\partial u_r}{\partial \theta} + \frac{\partial u_\theta}{\partial r} - \frac{u_\theta}{r}\right) & \frac{1}{r}\frac{\partial u_\theta}{\partial \theta} + \frac{u_r}{r} & \frac{1}{2}\left(\frac{1}{r}\frac{\partial u_z}{\partial \theta} + \frac{\partial u_\theta}{\partial z}\right) \\ \frac{1}{2}\left(\frac{\partial u_r}{\partial z} + \frac{\partial u_z}{\partial r}\right) & \frac{1}{2}\left(\frac{1}{r}\frac{\partial u_z}{\partial \theta} + \frac{\partial u_\theta}{\partial z}\right) & r\frac{\partial u_z}{\partial z} \end{pmatrix} \tag{2.2}$$

Since $u_r = u_z = 0$, those terms cancel out.

$$\sigma = 2\mu \begin{pmatrix} 0 & 0 & 0 \\ 0 & 0 & \frac{1}{2}\left(\frac{\partial u_\theta}{\partial z}\right) \\ 0 & \frac{1}{2}\left(\frac{\partial u_\theta}{\partial z}\right) & 0 \end{pmatrix} \tag{2.3}$$

Then we are left with

$$\sigma = \mu \frac{\partial u_\theta}{\partial z} \tag{2.4}$$

Or commonly seen in Cartesian coordinates:

$$\sigma = \mu \frac{\partial u}{\partial y} \tag{2.5}$$

Since the shear stress is constant, it is known that:

$$\frac{\partial^2 u_\theta}{\partial z^2} = 0 \tag{2.6}$$

When integrating the above equation, we get

$$\frac{\partial u_\theta}{\partial z} = C_1 \tag{2.7}$$

Then, integrating again, we have

$$u(z) = C_1 z + C_2 \tag{2.8}$$

Solving for the constants, the relevant boundary conditions are applied. First, a no-slip condition is assumed, which means the velocity at the wall $u_0 = 0$. Then, the velocity at the cone the input, u_{cone}. This can also be seen in Figure 2.2 for 2D flow.

$$u_{cone} = \omega r \tag{2.9}$$

$$\omega = \frac{v_{cone}}{r} \tag{2.10}$$

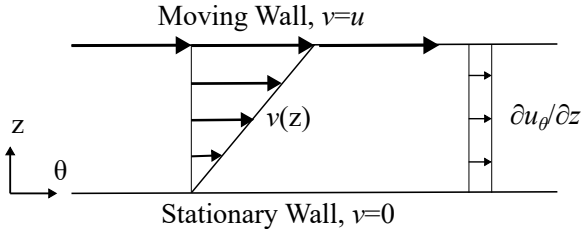

Figure 2.2: Shows Couette flow with cylindrical coordinates for CPV flow.

u_{cone} can be put in terms of ω, which provides the two boundary conditions: $u(0) = 0$ and $u(h) = u_{in} = \omega r$. Then, these boundary conditions are put into the original equation to solve for $u(z)$.

The first condition is $u(0) = 0$. This yields $0 = 0 + C_2$, $C_2 = 0$.

Then, using the second condition $u(h) = u_{in} = \frac{\omega}{r}$ it is known that $u_{in} = C_1 h$, $C_1 = \frac{u_{in}}{h}$. Finally, plugging in the values for C_1 and C_2 yields the velocity equation.

$$\vec{u}(z) = \frac{u_{in}}{h} z \tag{2.11}$$

Now that the velocity is known, the equation for shear stress is derived using the equation $\tau = \mu \frac{\partial u_\theta}{\partial z}$

$$\frac{\partial u_\theta}{\partial z} = C_1 \tag{2.12}$$

$$\tau = \mu \frac{u_{in}}{h} \tag{2.13}$$

$$\tau = \mu \frac{\omega r}{h} \tag{2.14}$$

It can also be assumed that $h = r \tan \alpha$.

$$\tau = \mu \frac{\omega r}{r \tan \alpha} \tag{2.15}$$

which simplifies to

$$\tau = \mu \frac{\omega}{\tan \alpha} \tag{2.16}$$

Because α is 0.5°, the small angle identity is used, where if $\alpha << 5$, we can assume that $tan\alpha = \alpha$. With these simplifications, we get the standard equation for a CPV with no fluid gap height.

$$\tau = \frac{\mu \omega}{\alpha} \tag{2.17}$$

A major limitation that makes this equation more or less unusable in practice is that there must be some gap height to make this device applicable in reality. Thus, we must also derive an equation for a CPV device with a fluid height between the cells and the tip of the cone. Since our assumptions in terms of fluid mechanics are the same, we can use the same methodology as before, using the stress tensor and canceling all multi-directional components of flow, leaving off at Equation 2.8. Hence, we will start from $\tau = \mu \frac{\partial u_\theta}{\partial z}$ and $\frac{\partial^2 u_\theta}{\partial z^2} = 0$.

It is known then, by integrating with respect to z that $\frac{\partial u_\theta}{\partial z} = C_1$. Integrating again yields $u(z) = C_1 y + C_2$. Like before, using the known initial conditions, a no-slip condition at the walls is assumed. Since $u(0) = 0$, we know $u(0) = C_1 * 0 + C_2 = C_2$. Thus yielding $C_2 = 0$.

It is also known that $z = h_0 + r * \tan \alpha$ where h_0 is the gap height between the cone and plate. We have u_θ in terms of height z, but the velocity in terms of the cone radius r is the desired equation. Thus, since $z = h_0 + r * \tan \alpha$, it can be written as

$u(r) = C_1(h_0 + r\tan\alpha) + C_2$. Since $C_2 = 0$, $u(r) = C_1(h_0 + r\tan\alpha)$. Since $u = \omega r$, $\omega r = C_1(h_0 + r\tan\alpha)$. Again using the small angle identity, $\omega r = C_1(h_0 + r\alpha)$. This yields the second constant $C_1 = \frac{\omega r}{h_0 + r\alpha}$. Since $\frac{\partial u_\theta}{\partial z} = C_1$ and $\tau = \mu\frac{\partial u_\theta}{\partial z}$, it is known that $\tau = \mu C_1$. Therefore, our final equation for a CPV with a defined gap height is the same as Equation 1.4 as follows.

$$\tau = \mu\frac{\omega r}{h_0 + r\alpha} \tag{2.18}$$

It should be noted that only tangential low should occur in this system. If there is significant radial flow, Equation 2.18 is not valid as it assumes purely tangential flow. A cartoon of this is shown in Figure 2.3.

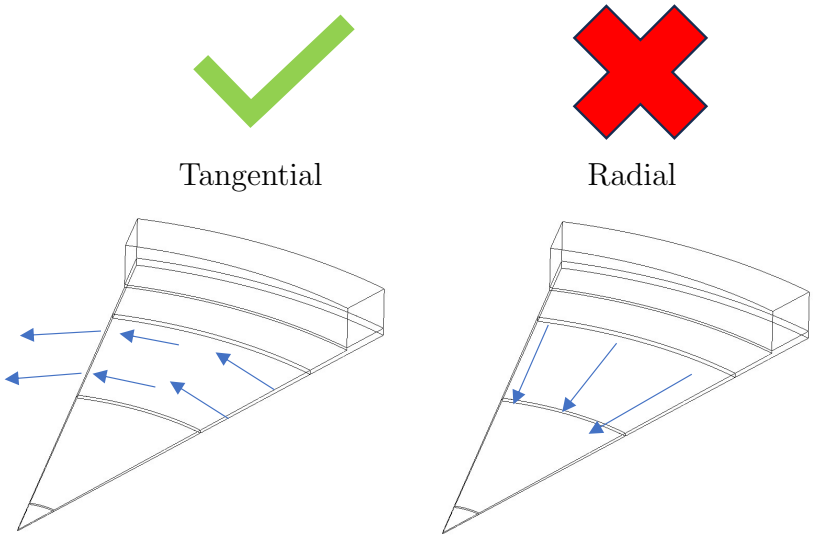

Figure 2.3: Shows the desired flow direction; tangential flow (left). Significant radial flow (right) compared to tangential flow would invalidate the derived equations for the CPV, notably Equation 2.18.

Based on the aforementioned gaps in the scientific literature, the present study will include a thorough methodology of the 3D model, mesh setup and analysis, case setup, and the post-processing needed for a complete CFD study.

2.2.2 CFD Geometry Setup

The first step in any CFD simulation is to define the fluid domain. For ease of changing the geometry for various simulations if needed, the geometry was made using the DesignModeler feature in ANSYS. First, the sketch plane was defined as the XZ plane in DesignModeler so that the Z-axis is the vertical axis and the X-axis is the horizontal axis. This way data can be taken along the X-axis for centerline data which would also serve as the radial coordinate. Then, a cross-sectional area of the desired fluid domain was sketched according to Figure 2.4a. Then, the sketch was revolved about the Z-axis. A revolve initially of 15 degrees on each side was used, for a total of 30 degrees. The symmetry revolve choice was made so that the center-line of the cone was along the X-axis, or radial axis for ease of postprocessing. The dimensions of the CPV were based on Franzoni et al's parameters[36] initially, except the cone is slightly smaller (radially) to reduce computation time.

The flow in the CPV should be axisymmetric, meaning the flow field should be the same tangentially around the domain at any point along the same radial and vertical coordinates. Before using sliced geometries, however, this concept must be verified computationally.

To make meshing more efficient, a slice will be made through the fluid domain offset from the XY plane by 0.75 mm off the Z-axis, shown in Figure 2.5a. This mostly separates the fluid under the cone and on the side of the cone. Also, a circular cut will be made in the middle shown in Figure 2.5b.

The radial portion of the domain where the cells will be seeded is between 25 and 40 mm on the bottom of the Petri dish. Therefore, an annular extruded slice will be made to define the cell area shown in Figure 2.6a. This will also be done for the whole disc geometry to maintain a consistent geometry and domain when verifying the axisymmetric slice simulations. This step is also helpful in the meshing stage, as

will be described in Section 2.2.3. All of the five bodies are preset to solid bodies, so they should all be changed to fluid bodies in DesignModeler.

Starting from the inner portion of the fluid, the names of the five fluid bodies are Inner, Inner2, Cells, Outer, and Upper. These are shown in Figure 2.7. Named selections should also be made to define the bottom, cone, left, right, top, and outer walls, where left and right named selections would only be made for the sliced geometry. Maintaining these naming conventions across CPV simulations is important when exporting data from multiple simulations. The list below shows how to define these zones geometrically in DesignModeler.

- Inner: Extrude circle on XY plane with a diameter of 10 mm.
- Inner2: The region between 'Inner' and 'Cells'.
- Cells: Extrude annulus on XY plane defined by two circles of diameters 50 and 80 mm.
- Outer: The region under 'Upper' and most outward radially.
- Upper: Create a slice through a plane defined as an offset from the XY plane by 0.75 mm.

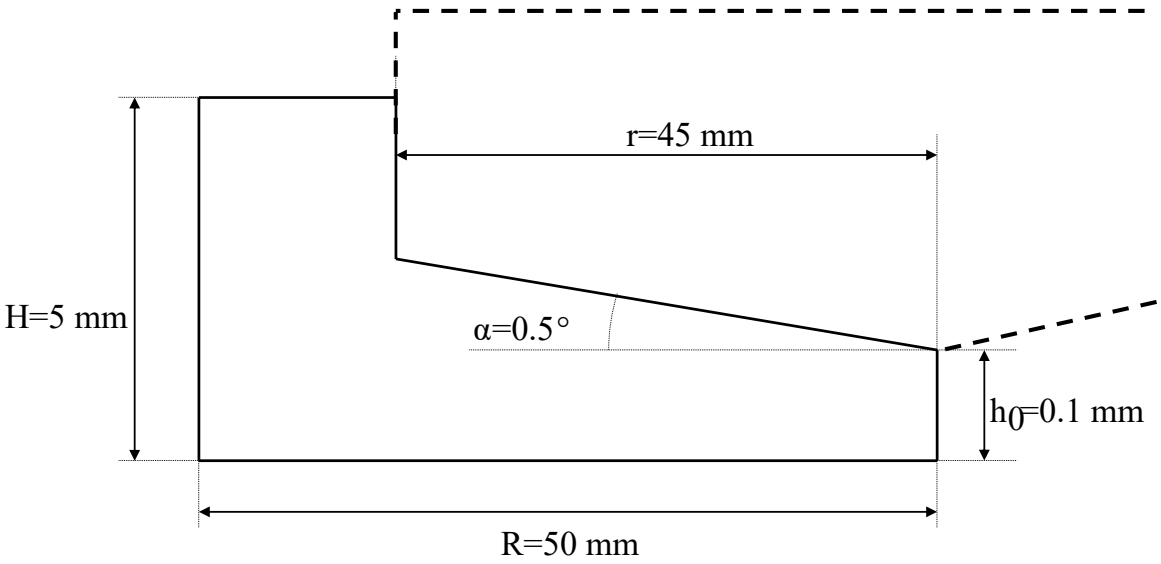

(a) Not-to-Scale 2D sketch

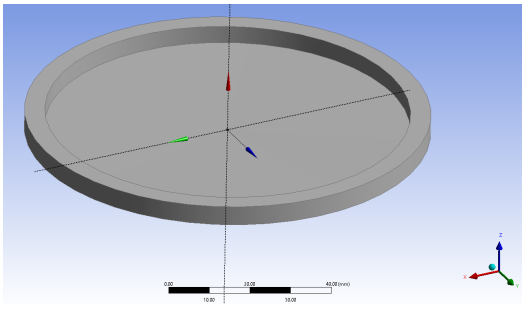

(b) Fluid Domain Disc

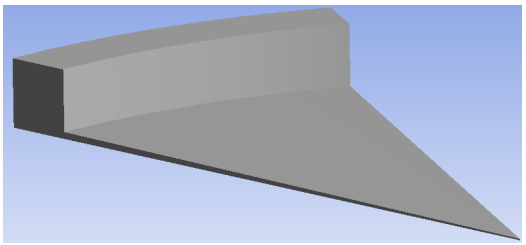

(c) 30° Slice

Figure 2.4: Geometry of 2D sketch and 3D revolve for simulation geometries.

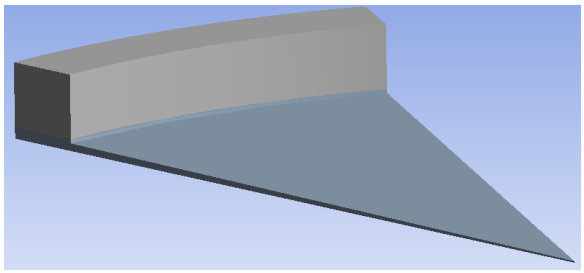

(a) Slice to separate the lower and upper fluid portions for meshing.

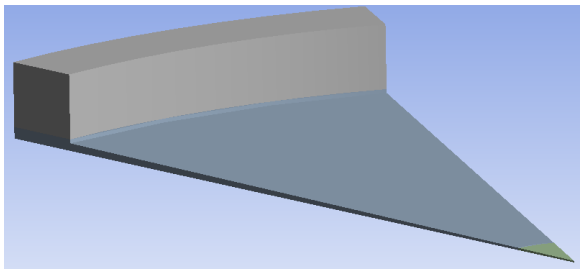

(b) Circular Slice for inner fluid portion. 'Inner' fluid portion is the tip of the slice in green.

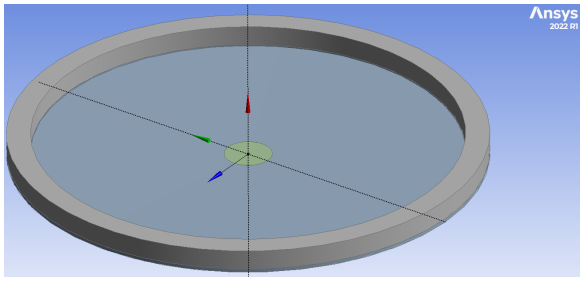

(c) Full disc geometry.

Figure 2.5: Shows DesignModeler steps for geometry definitions for the first two slices.

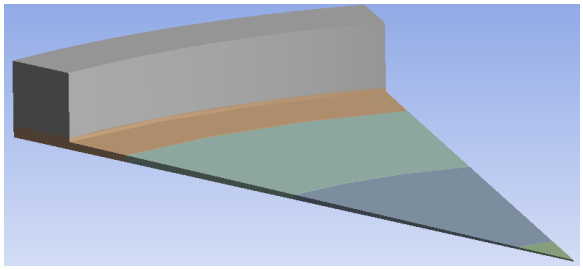

(a) Slice to isolate relevant cell area for the 30° slice geometry between 25 and 40mm radially.

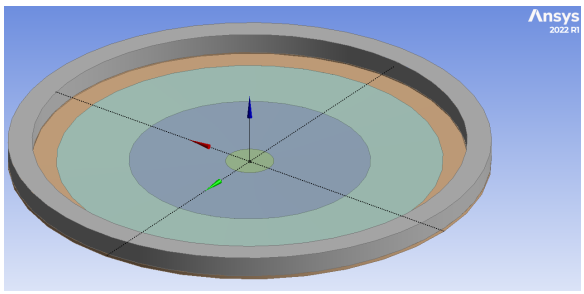

(b) Slice to isolate relevant cell area for full disc geometry between 25 and 40mm radially.

Figure 2.6: Slices for the cell area for the 30° slice and disc geometries.

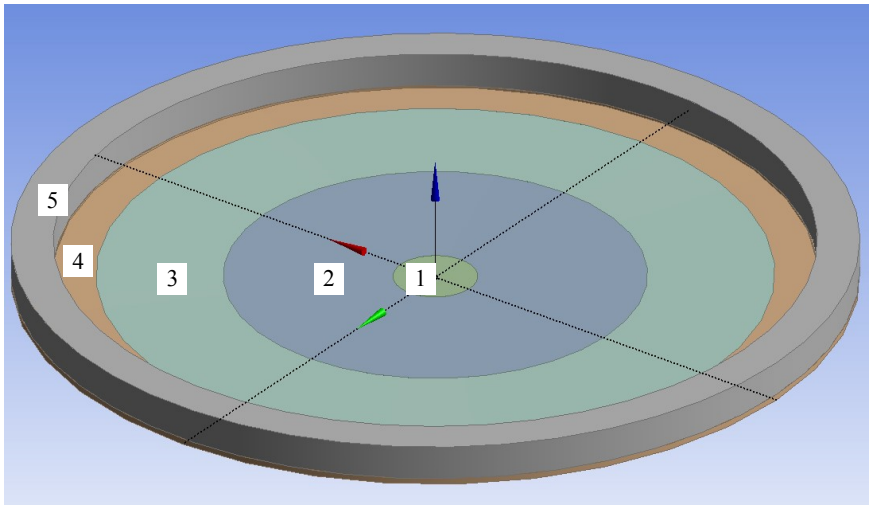

Figure 2.7: CPV fluid domain portions sliced for ease of meshing and post-processing. In numerical order, zones are named "Inner", "Inner2", "Cells", "Outer", and "Upper".

2.2.3 Meshing

The next step for a CFD simulation is the meshing process. This section of the CPV analysis details the meshing process for the different geometries so that others can replicate this work easily when working on a CPV similar to the geometries studied. In order to verify that the mesh is sufficient, a few criteria should be met. First, the element quality as well as orthogonal quality of the mesh should typically be greater than 0.2 as a general rule of thumb. Also, a Richardson extrapolation was performed to verify that the mesh used will sufficiently converge. The methodology of the Richardson extrapolation for mesh independence is described in more detail in Section 2.3.2 and is effectively the same application from the CPV to PPFC, so it will not be discussed in detail here. These will be taken into account as well as comparing the WSS values to the numerical model. This meshing analysis will be performed for a stationary bottom plate (no dynamic mesh). Later simulations will involve a dynamic mesh to simulate vibrations on the bottom plate.

There are two main goals of meshing for CFD simulations: having fine enough elements to best approximate the nature of the fluid flow field, and reducing the number of elements in order to minimize computational time. As the number of elements increases the results typically approach the exact solutions, but the computing time increases as well. In order to maximize accuracy and minimize time, an optimal mesh must be determined and assessed.

First, the full disc was meshed. The main mesh was defined as an element size of 0.5mm. A face meshing was applied to the inner face of the 'Inner2' and 'Cells'

bodies. The internal number of divisions was set to four. This means there will be four elements equal in height throughout the affected portions of the fluid domain. This is advantageous to ensure a consistent vertically sized mesh under the cone region. A cross-section of this is shown in Figure 2.8.

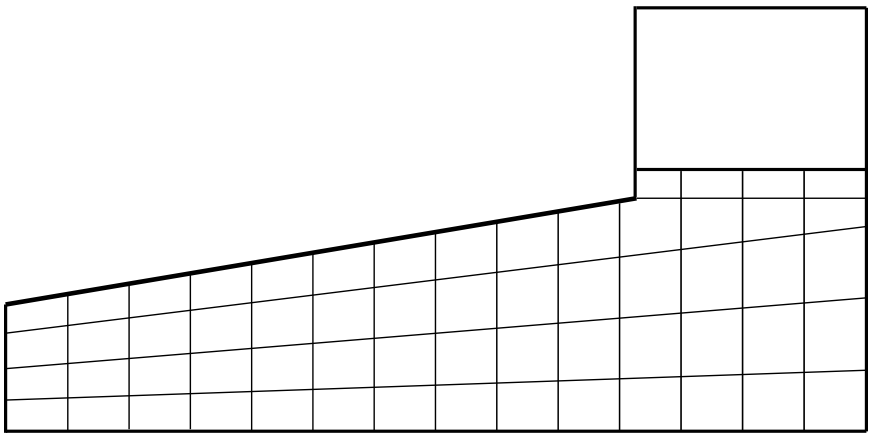

Figure 2.8: Shows a mesh under the cone with four divisions. There are four vertically stacked elements of equal height at any radial point under the cone.

A multiZone method was applied to the 'Cells' body and the 'sweep size behavior' was set to 'sweep edges'. The sweep edge was set as the outer top edge of the circular 'Cells' body. To define this, hiding all other bodies except for the 'Cells' region was necessary to prevent selecting an edge that looked like it was the correct edge but was actually the inner edge of the 'Outer' body. The MultiZone method forces more of a radially organized mesh, as opposed to a more cubic mesh that may have aspect ratio issues due to the circular geometry.

Another MultiZone method was applied to the 'Inner2' body. The sweep size behavior was again set to sweep edges, and this time both of the top side edges around the Inner2 body were selected. Body sizings were added to 'Inner2' and 'Cells' bodies with a 0.15 mm element size.

A third MultiZone method was added to the 'Outer' body. The sweep size behavior was again a sweep edge. A body sizing was also added to the Outer body with an element size of 0.15 mm. The reason this body was not compatible with a face mesh was most likely due to the inconsistent radial shape of the body closer to the edge of the cone. Therefore, a body sizing was implemented instead. The sizing was chosen to ensure the same number of layers under the cone (in this case 4) as the rest of the fluid domain.

Then, named selections were defined for all visible walls (all walls except for contact regions). All named selections should be the same across all simulations for consistency and ease of post-processing.

Then, the meshing for the 30 degree slice was performed. The meshing method was slightly different than the full disc because there were no left or right boundaries, so the face meshings were replaced by edge sizings at the relevant edges. They effectively accomplish the same thing for this application; to define a number of divisions heightwise throughout the domain.

The main mesh size was set to 0.25 mm. A method for 'Inner2' was set to Multizone with a sweep element size of 0.04 mm. An edge sizing on 11 edges was added; four on the corners of each 'Inner2' and 'Cells' bodies, two on the inner edges of 'Outer', and one on the center of the domain on 'Inner'. The number of divisions was set to four to match the full disc simulations. A body sizing on 'Inner2' was set to 0.15 mm element size. Another Mulitzone method was induced on 'Cells' and 'Outer', with a sweep element size of 0.25 mm. A face sizing on 'InnerBottom' had a 0.05 mm

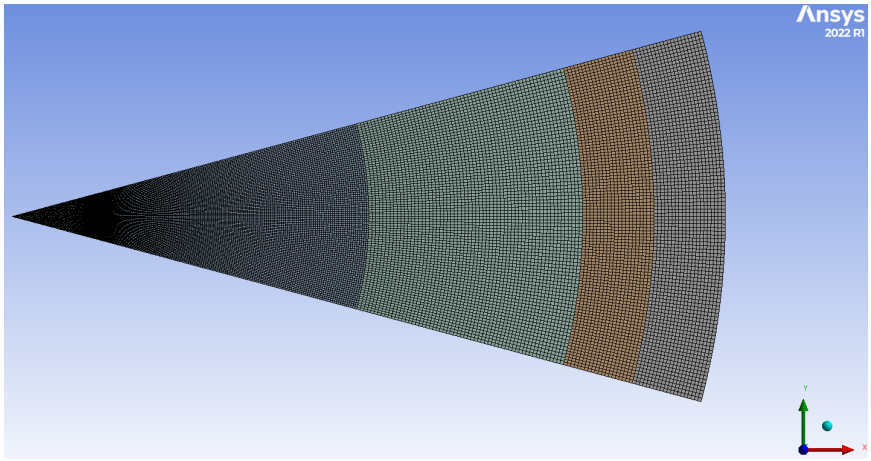

(a) Top view of 30° slice mesh

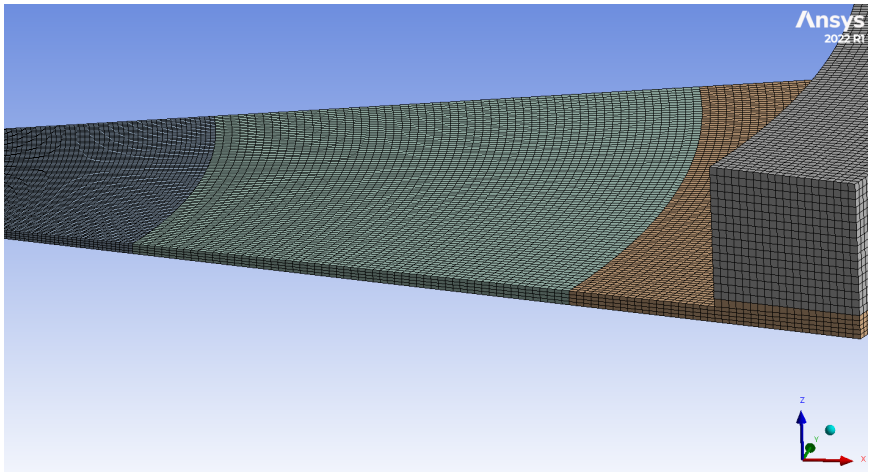

(b) Right view of 30° slice mesh

Figure 2.9: Images of 30° slice mesh.

element size. Lastly, named selections were defined for each outer wall; each bottom, cone, left, right, outer, and top was defined as a named selection for ease of use in Fluent. Figure 2.9 shows some examples of what the mesh looks like.

Lastly, the 1 degree slice is meshed. The main mesh is selected to be 0.4mm. Then, a MulitZone method is applied to the 'Inner2' body with a sweep element size of 0.3 mm. An edge sizing to the same 11 edges described in the 30 degree slice meshing is applied with four divisions. A body sizing on the 'Inner2' body was set to 0.1 mm.

This is smaller than the 30 degree slice for this sizing because the element quality should be kept above 0.2 for this region. A multiZone method was applied to the 'Cells' and 'Outer' bodies with a sweep element size of 0.25 mm. A body sizing of 0.05 was applied to the 'Inner' body.

Because of the 1° angle, the innermost cells are very sharp, and the element quality is very poor (around 0.03). However, the only region with lower than the acceptable 0.2 element quality is within the innermost 0.4 mm of the domain. This means that the other regions of the domain, and most importantly the cell region, are sufficient and the simulation should still be conducted and be considered valid. If the results do not match with the other disc and slice simulations, it may be an issue with the mesh. However, as will be discussed, this does not happen and all of these simulations yielded nearly identical results.

The named selections for the 1 degree slice are the same as the 30 degree slice. When the number of elements for each case is compared, it becomes obvious that there is a large advantage to using a smaller portion of the fluid domain (see Table 2.1). This is also not a perfect ratio because the 1 degree slice was refined to ensure sufficient quality throughout almost all of the domain.

Table 2.1: Number of mesh elements for each case.

Case	Elements (Thousands)
Full Disc	1,600
30° Slice	127
1° Slice	5.5

2.2.4 Fluent Setup

In Fluent, gravity was set to -9.81 m/s^2 in the z-direction. The pressure-based solver should be selected. The viscous (laminar model) is used for all simulations. The fluid material simulated is EGM-2. A new fluid with a density of 1015 kg/m^3 and viscosity of 0.007 kg/(m s) was defined as 'dex10' representing EGM-2 with 10% dextran added to increase the viscosity. All cell zone conditions should be set to fluid, not solid, and all cell zones are to be the 'dex10' fluid material. All contact regions are then set to matching, which ensures whatever one of the contact regions experiences, the matched contact region will yield the same results. It ensures a continuous fluid domain through contact regions.

For the methods of the solver, the SIMPLE scheme is implemented for steady simulations while PISO is used for transient cases. Under the 'Spatial Discretization' section, the node based, second order, and second order upwind methods are used for solving the gradients, pressure, and momentum respectively. All residuals were set to 1e-10 to ensure convergence for continuity as well as x, y, and z velocities. Residuals are a means of quantifying the error of the solver, and a simulation is typically run until the residual, or error, is below a certain threshold. The standard initialization method is selected.

Each boundary condition is defined to best represent what will be occurring to ECs in vitro. The geometry of the CPV fluid domain consists of the fluid that is between

the cone and the Petri dish. There will be fluid beneath the cone as well as on the side of the cone, simulating the fluid in the gap between the side of the cone and the Petri dish as seen in Figure 2.4a. All boundary conditions for the cone slice will be summarized in Table 2.2 and Figure 2.10. The only difference between the slice and the full disc is that the full disc will not have the left or right boundaries.

Table 2.2: Boundary Conditions of CPV Fluid Domain Slice. For the entire disc simulations, the left and right boundaries do not exist.

Face	Boundary Condition
Left/Right	Periodic
Bottom	Stationary Wall
Top	Outlet Vent
Cone	Rotating Wall
Outer Wall	Stationary Wall

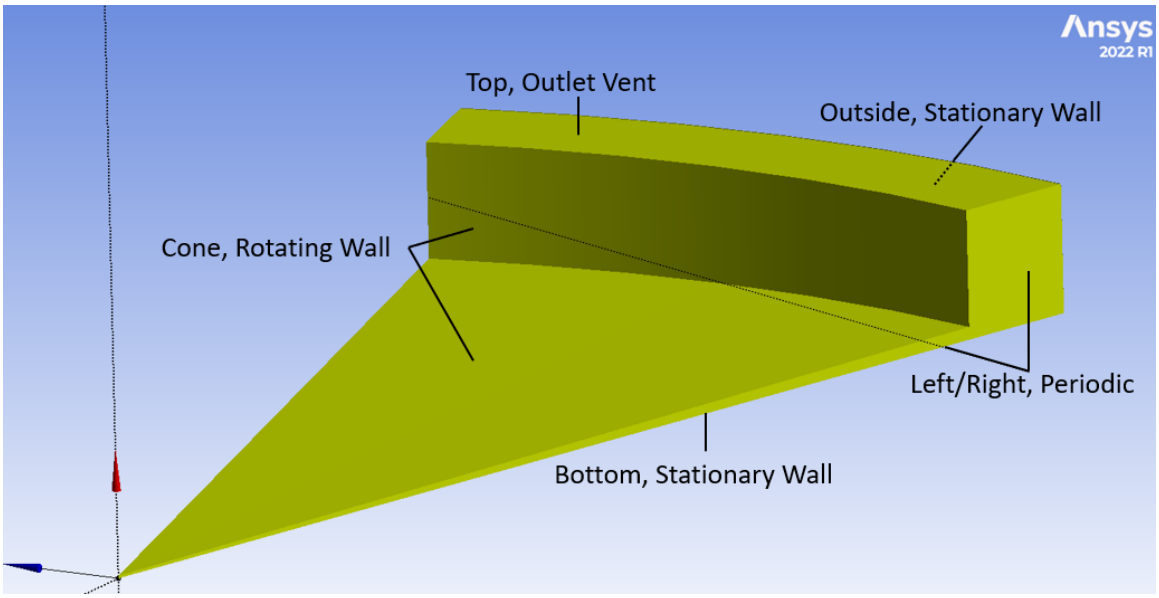

Figure 2.10: Boundary Conditions for CPV Simulations

The outermost wall will be a stationary wall, as that is simulating the inner wall of the Petri dish. The bottom will be a stationary wall when there are no induced

vibrations, as the cells/Petri dish will not be moving or rotating. For preliminary verification of the setup, this will be the case. When the cells are vibrating for later simulations, the wall will be treated as a stationary wall, but a dynamic mesh will be implemented to simulate the upward and downward motion of the Petri dish/cells.

The uppermost flat and horizontal portion of the geometry is the fluid domain exposed to the environment. Because there will be a change in volume of the fluid domain under the cone for later simulations, an outlet vent condition is imposed on the portion of fluid exposed to the environment. This is distinct from a symmetry boundary, which would mean fluid would not be able to enter or exit that boundary, which is not the case. While a symmetry boundary may yield an accurate WSS profile for the bottom boundary, it would not make physical sense to impose such a boundary in a location where fluid may displace in and out of, as a symmetry boundary implies no fluid will enter or exit. Also, for future simulations where the bottom boundary will have imposed vibrations, continuity is not conserved when the volume is changing and a symmetry boundary condition is used. Therefore a vent condition must used for this application.

The 'cone' is the top of the angled portion of the fluid as well as the inner side wall. This will be the rotating cone acting on the fluid, assuming a no-slip condition. A no-slip condition allows us to assume $V(cone) = V(TopFluid)$. All cone surfaces will have the same rotational speed at any given point.

In order to simulate just a slice of the fluid domain, a periodic boundary condition is used. A periodic boundary condition simulates a repeating pattern in the fluid

geometry. These boundary conditions can either be translational or rotational and in this case, a rotational boundary condition will be used. All of the left and right walls should be assigned as interfaces to define the periodic boundary conditions. This is necessary for assigning these boundary conditions in ANSYS. Then, adding a new mesh interface and selecting "manual create" will enable the defining of periodic boundaries. Each corresponding left boundary should be paired with its respective right boundary (InnerLeft and InnerRight, CellsLeft and CellsRight, etc.). Then 'Periodic Boundary Condition' is selected, as well as rotational rather than translational. Auto compute is selected to auto-compute the offset angle of the two boundaries but can be overwritten if needed.

2.2.5 Axisymmetric Test

As discussed, showing that the simulations are axisymmetric will enable the utilization of periodic boundary conditions, allowing us to simulate only a slice of the full fluid domain, greatly reducing the computational time. There will be three cases compared for this analysis: the full disc domain, a 30 degree slice, and a 1 degree slice to show numerical equality between multiple different domain segments. The driving rotational speed for all of the steady simulations will be constant at 4 rad/s. This rotational speed yields a maximum of around 2.5 Pa for the bottom plate, which is a little more than the 2.2 Pa that will be the target WSS for cell experiments. If the goal is to only achieve a maximum of 2.2 Pa, about 3.5 rad/s should be applied to the cone.

The full disc simulation was not converging well in terms of the residuals, so the WSS at two distinct points was measured. Typically, it is advisable to let the simulation run for around 1000 iterations to give the simulation enough iterations to lead to a converged solution. As seen in Figure 2.12, the WSS values seem to have converged, which indicates the simulation has most likely converged even though the residuals are higher than desirable. Therefore the WSS at a handful of distinct points is monitored for assurance of convergence. After 1000 iterations, the simulation was stopped.

For the full disc simulation, the residuals for continuity, x, y and z velocities were relatively constant around 0.3, 1.7e-5, 1.7e-5 and 2.2e-5 respectively. These are not very good residuals in terms of convergence, but the WSS values did converge over many iterations. Also, both of the slice simulations did converge to 1e-10 (which is more than sufficient) after about 1200 and 640 iterations for the 30 and 1 degree slices respectively. A vector field of the WSS at the bottom plate is shown for the full disc in Figure 2.11.

The WSS values at two distinct points, 35 and 20 mm in the x and y direction for the slices and full disc are shown in Table 2.4. Also a WSS contour can be seen in Figure 2.13. Figure 2.12 shows that there is no significant difference between the WSS profiles along the x and y axes, which further verifies axisymmetry.

It was found that the full disc, 30 degree slice and 1 degree slice yielded the same

Table 2.3: WSS comparison for full disc and theoretical WSS value from Equation 1.4. A grid independence study is still needed to verify the mesh.

Radial Position(mm)	Theoretical WSS (Pa)	Full Disc(Pa)
20 x	2.03	2.03
20 y	2.03	2.03
35 x	2.41	2.41
35 y	2.41	2.41

Table 2.4: WSS comparison between the full disc, 30 and 1 degree slice

Radial Position(mm)	Full Disc(Pa)	30° Slice	1° slice
20 x	2.03	2.03	2.03
20 y	2.03	-	-
35 x	2.41	2.41	2.41
35 y	2.41	-	-

results in terms of a WSS profile, and all matched the theoretically derived WSS value well. This was compared using steady simulations with a driving cone rotational speed of 4 rad/sec. The fluid was EGM-2 with 10% dextran to increase the viscosity. EGM-2 with 10% dextran has a density of 1015 kg/m^3 and a dynamic viscosity of 0.007 Pa s. The viscosity was increased so that the Reynolds number for the CPV would be well below 0.5, where secondary flows become significant. Secondary flows are not desirable for this application. Figure 2.13 shows a contour plot of the WSS for the 30 degree slice. The vector fields for the 30 and 1 degree slices are shown in Figure 2.14.

The WSS values were tracked at 35 and 20 mm along the X-axis (and Y-axis for the full disc) to compare the WSS profile consistency in terms of the radial coordinate of the domain. The X-axis is a midline through the slice geometries representing the radial coordinate. It should be noted that the slice geometries will not have measurements in the y-axis, as they are only small angles centered about the x-axis.

Since the WSS values are the same for the corresponding radial coordinates, it can be assumed that the simulations are axisymmetric. This shows that the use of only a small slice of the fluid domain is valid, and will tremendously help in reducing computational time for further simulations. Thus, the 1 degree slice will be used for further analysis.

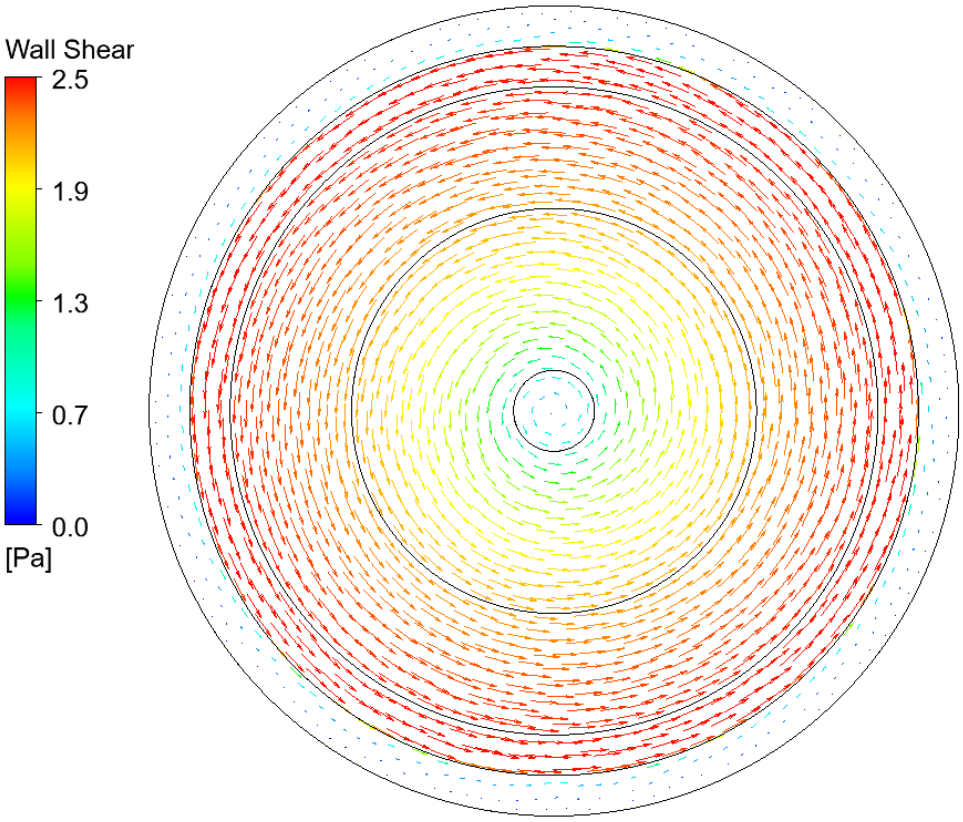

Figure 2.11: Shows a WSS vector field for the full disc simulation with an expected maximum WSS of about 2.5 Pa.

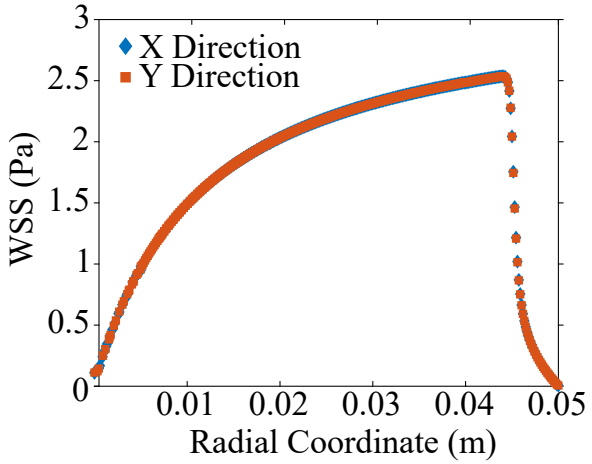

Figure 2.12: Comparison of WSS magnitude vs radial coordinate for the full disc simulation after 1000 iterations. This shows that the WSS magnitudes are the same along the X and Y radial coordinates verifying the axisymmetric assumption.

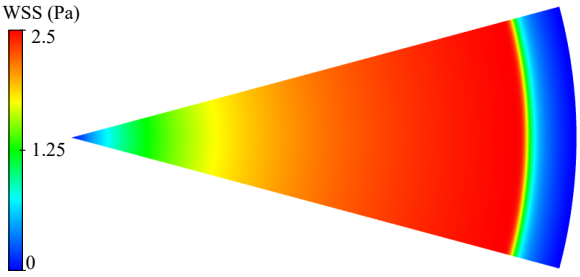

Figure 2.13: WSS contour of the steady case for the 30degree slice. This compares well to the max theoretical WSS value (at 45mm) of 2.549 Pa (0.6% error).

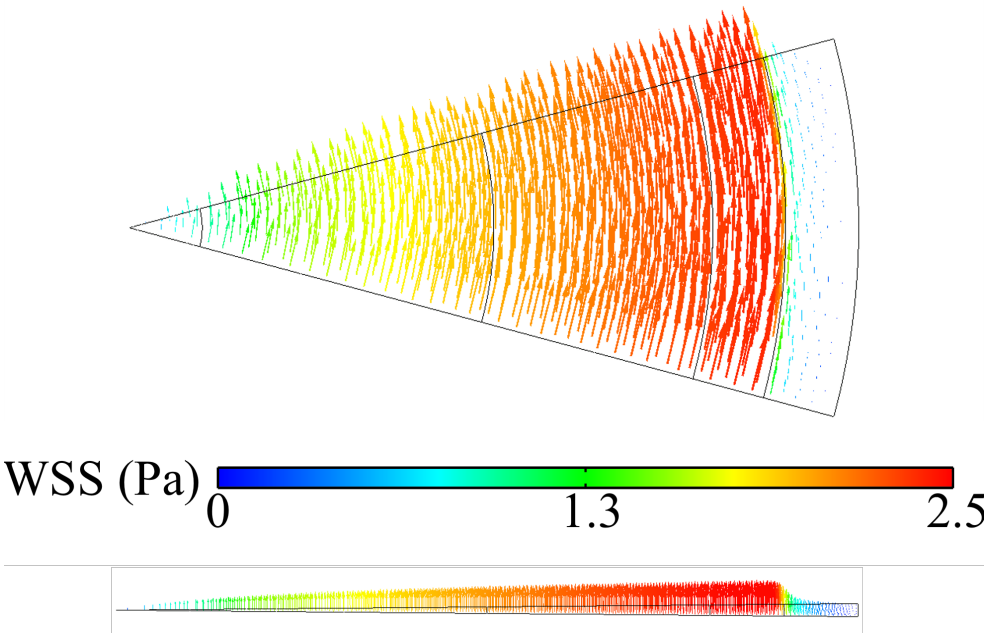

Figure 2.14: WSS vector field of the bottom plate for the 30 and 1 degree slices on the top and bottom respectively.

2.2.6 Steady Vs Transient Results

Next, we will check the validity of a transient case compared to the steady case. Since the cone slice of 1 degree takes the least time to simulate, that will be the geometry used in further simulations for the CPV.

When performing transient simulations, the time step must be small enough to fully capture what is happening each time step. In order to do this, fluid should not travel more than one mesh element throughout any one time step. This concept is quantified by the Courant number, defined as follows.

$$C = \frac{v\Delta t}{\Delta x} \tag{2.19}$$

The Courant number is effectively a ratio between the velocity and a combination of the respective time and displacement, where C, when less than 1, is a constant that ensures a fluid particle will not travel more than one element in any one time step. For the best results of a transient simulation, it is recommended to maintain the Courant number less than 0.7. This is to ensure that a theoretical 'particle' would not travel more than one cell over any one time step. For example, a Courant number greater than 1 means that a particle would 'skip' a cell within one time step. Since a simulation will converge substantially better when a particle travels less than one cell per time step, a Courant number of 0.7 is desirable. With the given parameters of $\Delta x = 0.2$ mm, $v = wr = 4$ rad/s $*0.04 = 0.16$ m/s and a Courant number of 0.7, Δt =8.75e-4 seconds, which will be rounded down to 5e-4 seconds to make time steps

in multiples that go into 1 second for ease of post-processing.

Because this will be a transient simulation, the PISO solver will be used. Also, for the transient formulation, the second order implicit is selected. As seen in Table 2.5 there is no significant difference between the steady and transient simulations with a constant 4 rad/s rotational cone speed once converged. At 20 and 35 mm in the radial direction of the bottom boundary, there was no notable difference between cases.

Table 2.5: Wall Shear Stress Comparison for Transient Vs Steady for a 1 degree slice.

X (mm)	Steady WSS (Pa)	Transient WSS (Pa)
20	2.03	2.03
35	2.41	2.41

Something to keep in mind is that these simulations are performed prior to a proper mesh analysis, so although the results seem correct compared to the theoretical equation and to each other, there still must be an analysis done to show independence between the mesh and the simulated result. These simulations are only performed to show how they compare to each other and whether the various angle slices yield the same results. The accuracy of the simulations will most likely be a function of the number of divisions between the cone and plate because the wall shear stress can be more accurately calculated with more cell layers.

As explained previously, the 2D rotational velocity profile with respect to the vertical direction is Couette flow because the cone is uniformly rotating and the bottom boundary is stationary. This means that no matter how many vertical divisions there

are in the fluid domain, the resulting WSS value should be the same due to the same velocity gradient. This idea is similar to linearly interpolating a straight line; It will always be the same slope no matter where in the line you are measuring. This makes a mesh analysis much more difficult for a steady simulation because all of the meshes, so long as the element quality, aspect ratio and orthogonal quality are sufficient, should yield the same WSS values. Thus, the transient cases will be the basis for our mesh independence test.

2.2.7 Mesh Independence Test

In order to verify that the mesh is sufficiently providing accurate results, a mesh independence test will be performed. A Richardson extrapolation was done, and the method of how this is carried out can be seen in Section 2.3.2.

To ensure the velocity profile is as expected, a different mesh setup was used, this time with a domain consisting of 10 divisions rather than four. This was to increase the number of data points in the vertical (or z) direction. The velocity profile, as discussed previously should represent Couette flow, where the velocity profile is linearly decreasing from the cone to the bottom boundary, where the velocity should be zero (see Figure 2.2).

The mesh should be finer to ensure the flow field is representing what will be occurring physically. The mesh was adjusted to maintain an element quality of at least 0.2 with 10 divisions rather than 4. This resulted in a mesh with about 50k elements for a 1 degree slice. As a check, the WSS at 35mm was 2.41 Pa, the same as the other cases.

The normalized velocity profile can be seen in Figure 2.15. Since the R^2 value is 1, there is a clear linear correlation between the velocity and vertical coordinate. Therefore it is indeed Couette flow, which is expected.

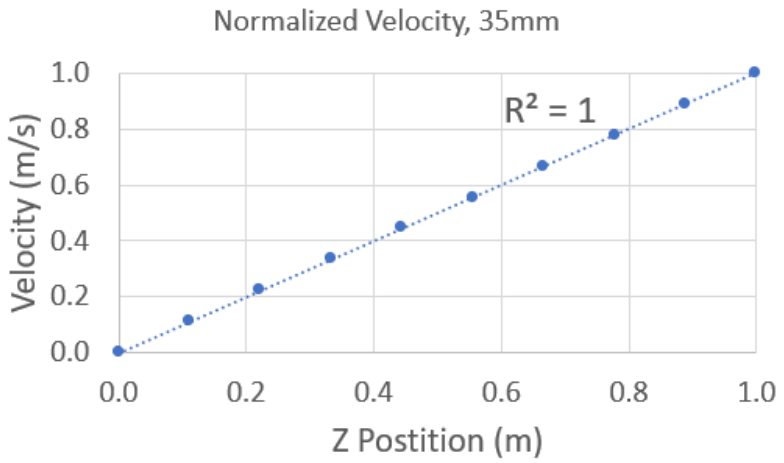

Figure 2.15: Normalized tangential velocity with respect along the Z-axis. An R^2 value of 1 shows a perfect linear trend in the data, showing the flow of the CPV with respect to the vertical dimension is Couette flow.

It is again important to note the importance of using a vent condition at the top boundary rather than a symmetry boundary. A symmetry boundary condition would assume that no flow can travel through the symmetry boundary, but fluid should be able to do so in the top portion of the CPV due to the centrifugal force. In preliminary simulations where the bottom boundary was not vibrating, there was no difference in the resulting WSS profile along the bottom of the device, but there was a difference in the flow fields on the side of the cone. This is especially important when the $\widetilde{R}$ is greater than 0.5 or when the cone is moving up and down relative to the plate, as will be discussed in Section 2.2.10. It is crucial to keep in mind what is physically occurring in the device and how specific boundaries should be defined.

2.2.8 Replicate Literature

As another test to determine whether the setup for the CPV geometry is valid for transient cases as well, the results from Franzoni et al. were duplicated.[36] Both types of waveforms, atheroprone and atheroprotective, were analyzed and replicated. The 25 and 45mm cone radius 'CFD Model' solid line from Figure 5(a) (Figure 2.16 in this work) from Franzoni et al. was traced as a starting point to calculate the required rotational speed input for the cone using Equation 2 (or Equation 1.4 in this work) from Franzoni et al. See Equation 1.4 for the WSS equation of a CPV that accounts for the gap height.

Tracing the plots was done with the online tool WebPlotDigitizer. This yielded the transient waveforms for WSS, for both the atheroprone and atheroprotective cases. Then, a transient rotational speed file was formatted as a readable input for ANSYS. The first couple of rows show the syntax ANSYS needs to properly read the input file. The syntax for the input file are shown as follows:

ProtPprRoteq2 2 42 1
time Roteq2
0 4.1
0.014 4.87
00.026 5.75
...

In the file, "ProtPprRoteq2" is the name of the rotational speed data that Fluent inputs as a text file. This is the named expression used on the cone boundaries. The '2' after the file name defines how many inputs are to be read by Ansys. In this case,

rotational speed and time. The number 42 is the number of points in the file that were traced. Only three are shown here as an example, but there were a total of 42 data points taken for this waveform. The '1' in the first line shows that this file is to be read cyclically. If only one cycle is desired, it should be a 0 instead of a 1. It does not matter if the time steps are evenly spaced or not, as Fluent interprets the rotational speed input with respect to the inputted corresponding time steps with linear interpolation.

It was found that the methodology in Franzoni et al. was not consistent with their physical setup. They first used Equation 1.3 (not accounting for the cone gap height) to derive the cone velocity based on Dai et al's waveforms for WSS that was based on MRI data. Then, after using Equation 1.3, Franzoni used Equation 1.4 to define their theoretical result for WSS (accounting for the gap height). This is inconsistent because they should have used Equation 1.4 for both steps, for in both steps a defined cone height must exist for the physical and numerical data to be relevant to each other given the fact that their physical apparatus had a gap height present. However, when their methodology is used, the data of this work and Franzoni's matches well to verify this work's CFD setup. As another verification, other simulations are compared to the theoretical WSS values.

As Franzoni et al. discussed in their work, there will be a time delay that will occur because of the high acceleration of the cone at certain points of the cardiac waveform cycle. This accounts for the slight delay for the 45mm curves of this work compared with Franzoni's work. The time delay, as is evident by the equation for the time delay

that Franzoni described, will have a greater effect as the radial coordinate increases.

However, the amplitudes and trace of the curves from this work and Franzoni's simulations are not significantly different. To eliminate any simulation startup errors, the second cycle was recorded for comparison to Franzoni. This is why the resulting plots will start at about 0.8 seconds; the period of roughly 0.8 seconds that was used in Dai et al's. work, the author who obtained the original MRI patient-specific data. There was next to no variation between the magnitudes of the atheroprotective cases between this work and Franzoni's work, with the largest error of less than 2%, as seen in Figure 2.17.

The atheroprotective simulation results also compared well to the numerical model as seen in Figure 2.18. There is little difference between the theoretical and simulation results. Keep in mind that the results from comparing this work's simulations to the theoretical model will have a different magnitude than the comparison to Franzoni's work because of Franzoni's methodology. Figure 2.18 provides a simulation comparing to the theoretical model of Equation 1.4, while Figure 2.17 replicates part of the work of Franzoni. Both atheroprotective simulations match the respective desired WSS, showing the inputs and setup for simulations are thus far valid and correct.

The atheroprone simulation results also compared well to Franzoni's simulations. There were however two locations, where the fluid acceleration is highest, where the WSS waveforms deviate. The reason for this is the time delay that takes effect which is described and addressed by Franzoni. There is a transient delay between the cone rotating and the bottom plate experiencing the respective WSS. If there is a high

acceleration in cone speed, the response may be dampened as seen in Figure 2.19 for the larger radius and in Figure 2.20. Effectively, Franzoni accounted for the time delay to better match the theoretical WSS value. As aforementioned, the oscillating acceleration of the cone will result in a slight dampening of WSS magnitude on the bottom plate. Also, all other sections of the waveform match very well in terms of magnitude in Figure 2.19. Both the replicated work of Franzoni as well as the comparison to the numerical model match well for both the atheroprotective and atheroprone waveforms.

Since this work will not be focusing on flow with as high acceleration, this will not be an issue for this study. This work is focused on providing a waveform that will be more represented by the atheroprotective waveform in the sense that the WSS is fully positive with relatively high magnitude as opposed to low oscillating WSS with high acceleration. Nonetheless, both the atheroprotective and atheroprone cases match fairly well with their respective theoretical WSS values for these simulations, especially for the waveform that is more relevant to this study, the atheroprotective case.

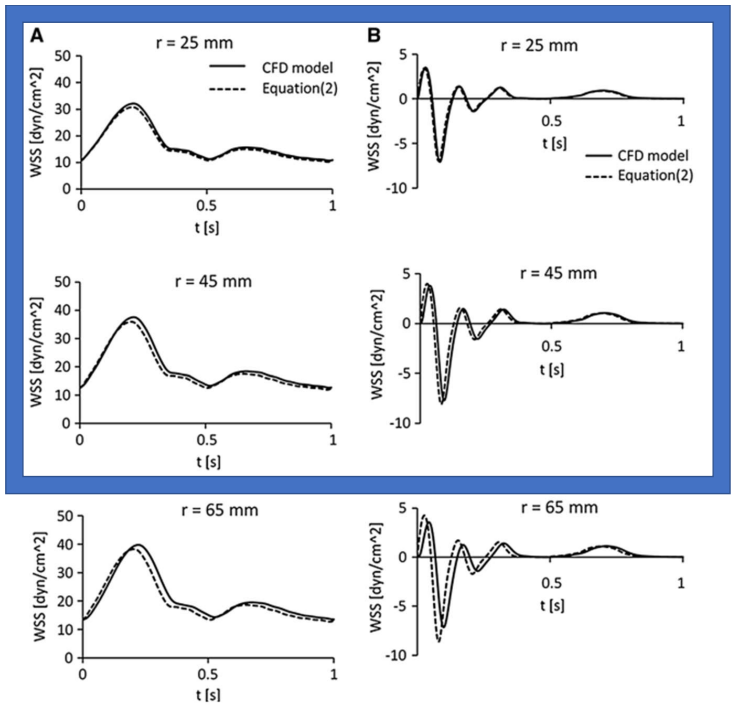

Fig. 5 **a** Atheroprotective WSS waveforms (Dai et al. 2004). The continuous line represents the WSS value on the plate surface calculated with CFD simulation while the *dashed line* represents WSS calculated with Sucosky et al. (2008) formulation (2). The curves were calculated for $\mu = 0.00354$ Pa s, $h_0 = 0.1$ mm, $\alpha = 0.5°$ and $r = 25$, 45 and 65 mm, respectively. **b** Atheroprone WSS waveforms (Dai et al. 2004). The continuous line represents WSS value on the plate surface calculated with CFD simulation while the *dashed line* represents WSS calculated with Sucosky et al. (2008) formulation (2). The curves were calculated for $\mu = 0.00354$ Pa s, $h_0 = 0.1$ mm, $\alpha = 0.5°$ and $r = 25$, 45 and 65 mm, respectively

Figure 2.16: WSS profiles from Franzoni et al. The 25 and 45 mm curves were used for further analysis

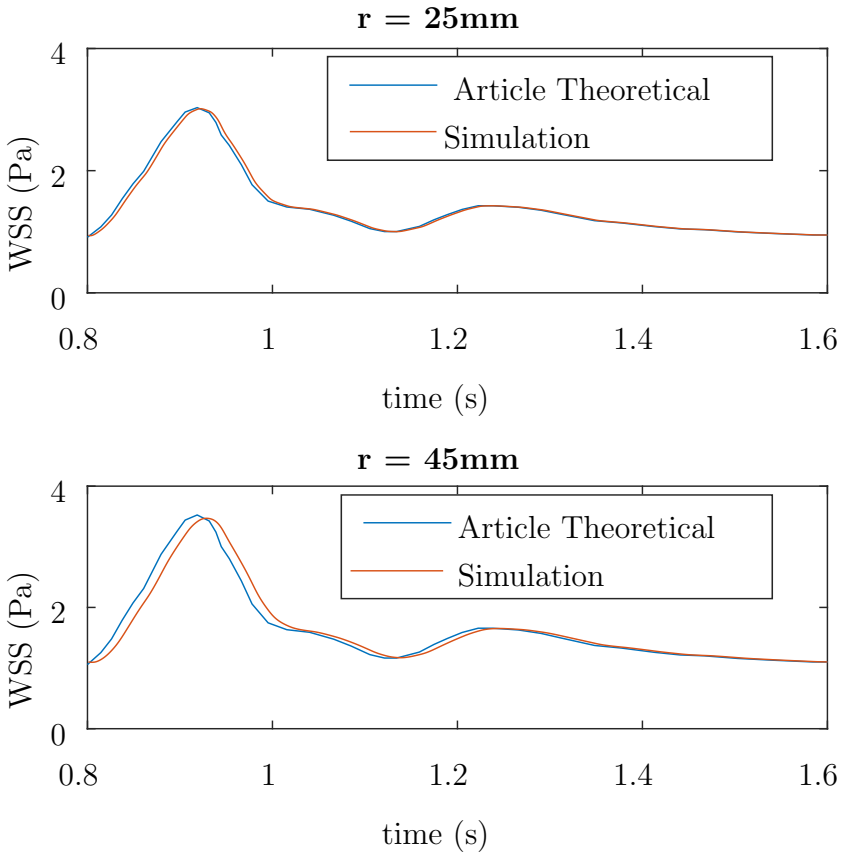

Figure 2.17: Shows WSS comparison to Franzoni et al. at 25 and 45mm along the bottom plane for the atheroprotective simulation.

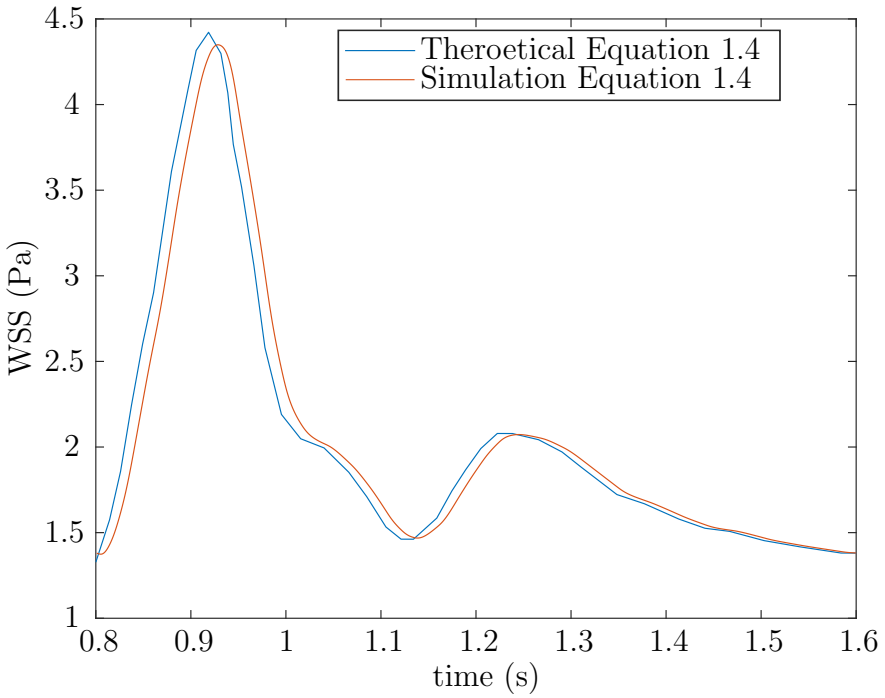

Figure 2.18: Comparison of the theoretical Equation 1.4 and simulations at r=45mm.

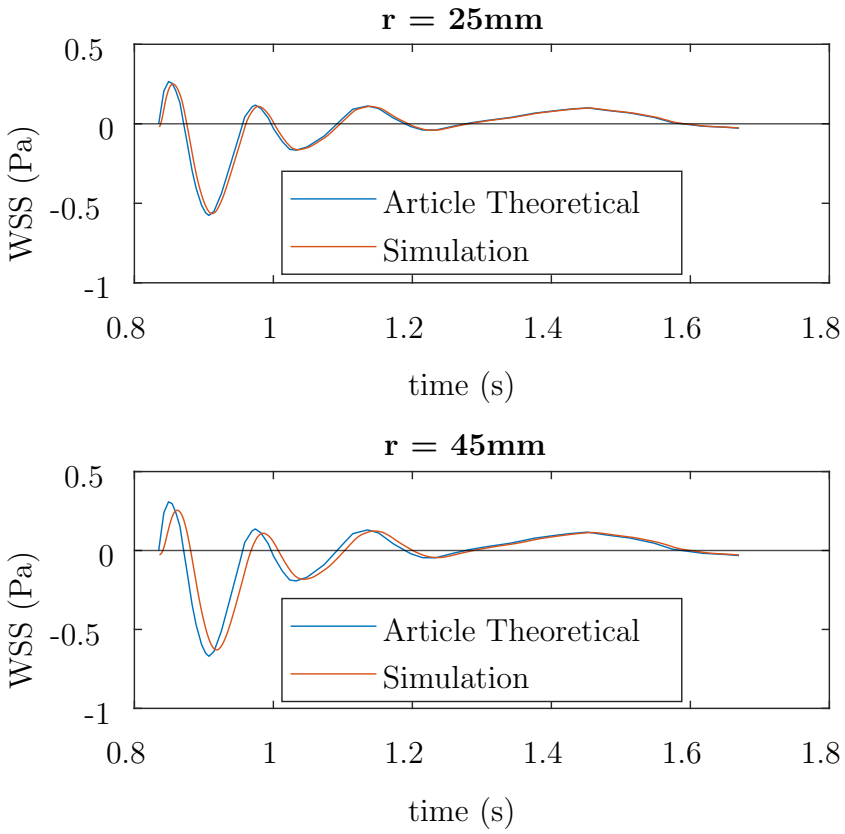

Figure 2.19: Comparison of atheroprone simulations at 25 and 45mm.

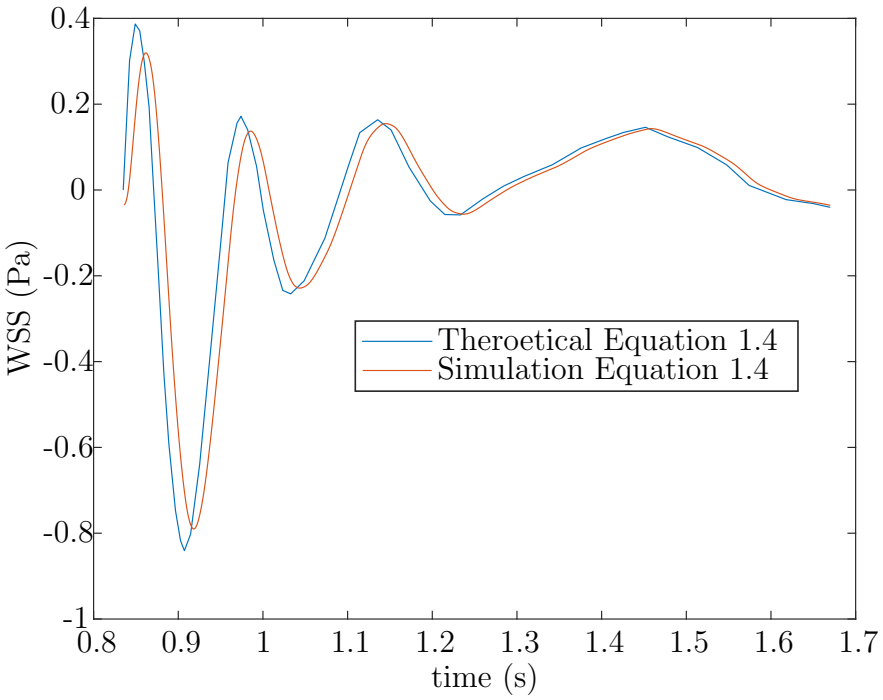

Figure 2.20: Comparison of the theoritical Equation 1.4 and simulations at r=45mm for an atheroprone simulation.

2.2.9 Dimensional Analysis

Now that it has been shown that the CPV simulated agrees with the general defining equations for the WSS of this device for both steady and unsteady cases, the CPV parameters will be optimized for this application. The parameters that should be optimized are based on Equation 2.20 derived in Sdougos et al, and Equation 1.4 inspired by Sdougos et al. but including a set gap height. Based on the findings of Sdougos et al, $\widetilde{R}$ for a CPV without significant secondary flows should be under 0.5.

It is also important to keep in mind that a design requirement of this device is to implement oscillating vibrations of a displacement of 100 μm (or 50 μm amplitude sinusoidal motion). With this in mind, the gap height should be greater than 50 μm to avoid hard contact with the cone tip, which may cause damage to the device or ECs seeded on the plate as well as deviate from the desired vibration motion as opposed to a hard stop. Also, a larger gap height would result in a larger time delay between the cone and plate, potentially dampening the WSS magnitude desired. Thus, a gap height of 100 μm is chosen as a gap height.

Another physical restraint is the cone radius. The largest reasonable round petri dish that is used is 100 mm in diameter, or 50 mm in radius. This means the radius of the cone must be less than 50 mm. Therefore the radius of the cone will be at most 45 mm to avoid any wall effects. It is also desirable that the cone radius is as large as possible so that there is as constant of a WSS profile over the radius as possible. This idea is shown in Figure 2.21, where the slope of WSS approaches 0 as the radius approaches infinity. With these considerations in mind, a radius of 45 mm is chosen

for the cone.

One feature of the CPV analyzed was the effect of secondary flows, or radial flows, in the system. According to Sdougos et al. the effects of secondary flows become significant when $\widetilde{R}$ is around 0.5.[100] However, the derivation of Sdougos et al. did not account for the gap height between the cone apex and the plate. This will certainly have an effect on $\widetilde{R}$, much like it did with the WSS derivation.

A CPV was simulated where $\widetilde{R}$ of the fluid was less than 0.5 at 0.04 mm, where the edge of the cells will be. This, however, caused issues in the flow field and distorted the tangential component of WSS. It has been conventionally assumed by a plethora of authors that as long as $\widetilde{R}$ is less than 0.5, the flow is purely tangential and uniform. This is not a valid assumption, as Sdougos et al. state that there will be secondary flows, and it is just a matter of whether or not they will significantly affect the flow field. Also, Sdougos et al's analysis was performed under the assumption that there is no gap between the cone tip and the bottom plate. This is not the case in almost all of the cone and plate applications performed in this field. This is not an error of Sdougos' analysis, but rather a misapplication of it.

In almost all CPV applications, there is a cone gap, which alters the numerical model that some have analyzed for the shear stress, but few have used this logic for adjusting $\widetilde{R}$. For example, Sucosky was one of the first to derive the shear stress for a CPV with a set gap height but did not translate this analysis to $\widetilde{R}$.[110] This should be taken into consideration when determining what the desirable Reynolds number should be.

By nature, the cone and plate, as discussed, will have a radial secondary flow compo-

nent. A goal of this work is to minimize that radial component to ensure consistent WSS values, and therefore secondary flow is an important feature of these devices to keep in mind when designing one. The radial mass due to secondary flows will cause the fluid on the outer edge to rise. This causes a vortical motion in the upper and outer regions as seen in Figure 2.22. This is important because physically, a symmetry boundary may yield the same WSS results as a vent condition, but does not properly simulate what the CPV will be actually doing at this boundary. This will be apparent when the fluid volume changes over time due to vibrations.

Figure 2.23 shows an example of when $\widetilde{R}$ is 0.5 and yields an improper WSS profile according to Equation 1.4. It can be seen that on the outer edge of the cone, there is a spike in WSS. This spike appears to be an indicator that secondary flows are significant, but the exact reason for this peculiar profile is unknown. This is not to say that secondary flows are only significant when this spike in WSS is present, but it can help indicate that they most likely are present. Although the magnitude of the WSS seems to be relatively correct as seen in Figure 2.23, the radial component is significant thus the tangential component is lower than desired.

Also, the radial component of WSS is about a third of the magnitude of WSS. This means the flow cannot be assumed as purely tangential at this value for $\widetilde{R}$. It can also be seen that when there is a significant secondary flow effect, the WSS has a peak around 25 mm radius, and then the tangential WSS will begin to decline. It is an issue that the tangential component of flow no longer dominates, and it can no longer be assumed that the tangential WSS follows Equation 1.4. The effect of accounting

for the gap height for $\widetilde{R}$ is shown in Figure 2.26 as well as the following derivation.

$$\widetilde{R} = \frac{r^2\alpha^2\omega}{12\nu} \tag{2.20}$$

Then, substituting $r^2\alpha^2$, which is the gap height, for $(h_0 + r\alpha)^2$ to account for $h_0$we get

$$\widetilde{R} = \frac{(h_0 + r\alpha)^2\omega}{12\nu} \tag{2.21}$$

According to this model, $\widetilde{R}$ at 40 mm, where it was previously 0.5, is now 0.75 when accounting for the gap height. However, even when $\widetilde{R}$ is 0.5 using Equation 2.21, there are still significant secondary (radial) flow effects, as shown in Figure 2.24. This means that for a CPV with a fixed initial gap height, $\widetilde{R}$ of 0.5 according to this model cannot be the cutoff for where secondary flows seem to begin to become significant using either Equation 2.20 or 2.21.

Therefore $\widetilde{R}$ of less than 0.2 will be the acceptable criteria for this study because that seems to be a Reynolds number where secondary flow does not adversely affect the flow field according to the simulations. The result of this is shown in Figure 2.25. This work is not focused on determining the cutoff Re where secondary flows start to become significant but only utilizes a setting where secondary flows are insignificant. The main purpose for analyzing $\widetilde{R}$ is to ensure that the CPV geometry and fluid parameters will not yield excessive secondary flows.

Equation 2.21 shows that as the rotational speed decreases, $\widetilde{R}$ will decrease proportionally. Also, when the rotational speed, and thus $\widetilde{R}$, decreases, the tangential WSS is closer to the WSS magnitude as well as the numerical solution, and the radial WSS is reduced.

Because $\widetilde{R}$ of 0.2 is chosen as the acceptable minimum rather than 0.5 based on Equation 2.21, the rotational speed of the system was decreased. This effectively means that this fluid, EGM-2, is not suitable for this application given its density and viscosity. One solution to this issue is to add dextran to EGM-2, which increases the viscosity of the fluid. When looking at Equation 1.4, as the viscosity increases, the rotational speed, which is the only other non-geometric variable, must decrease proportionally. When the viscosity increases and the rotational speed decreases, $\widetilde{R}$ decreases exponentially based on Equation 2.21. This means increasing the viscosity is beneficial in reducing secondary flows. Thus, dextran will be added to the fluid to increase the viscosity of the fluid from about 0.0007 to 0.007 kg/(m*s).

The only parameter not discussed thus far is the cone angle. The cone angle will, according to Equation 1.4, increase or decrease more or less proportionally to the cone rotational speed. The consequence of increasing the cone angle and rotational speed proportionally is that $\widetilde{R}$ will increase exponentially. This is problematic and thus the cone angle should be as small as possible so that $\widetilde{R}$ is minimized. This means the cone angle will be 0.5 degrees, as it is the smallest reasonable non-negligible angle.

The WSS range yielded from these experiments will be between about 0 to 2.2 Pa. The known input parameters are the maximum WSS (2.2 Pa) and the maximum value for

$\widetilde{R}$ (0.2) assuming a known gap height. The radius of the cone should be large enough so that the cell area is exposed to a relatively constant WSS magnitude and direction. The cells should be located in a specific range that spans about 15mm radially for confluence and imaging purposes. There also should be at least 2 mm between the edge of the cone and the outer radius of the cell area so that the cone-edge effects would not influence the flow field over the cells. The radius of the cone should be small for the sake of ease and cost of assembly, manufacturing, and experimentation.

The cells exposed to flow should experience the same WSS as much as possible for experimental consistency. The range of WSS that is considered relatively constant must be defined to analyze the cutoff for the acceptable WSS range. The red circles in Figure 2.21 show the point where the WSS is 15% of the maximum value, which is considered to be the acceptable cutoff range for WSS magnitude. From this, it can be determined that given the 100 μm gap height, that a cone radius of 45mm would be sufficient when the cells are seeded between 25 and 40 mm. A gap height larger than this would yield too high of a WSS range. Table 2.6 shows the dimensions of the flow camber as well as the relevant fluid properties.

Table 2.6: Parameters of the CPV

Feature	Value
Gap Height (h_0)	100 μm
Cone Radius (r)	45 mm
Cone Angle (α)	0.5°
Fluid Viscosity (μ)	0.007 kg/(m*s)
Fluid Density (ρ	1015 kg/(m^3)

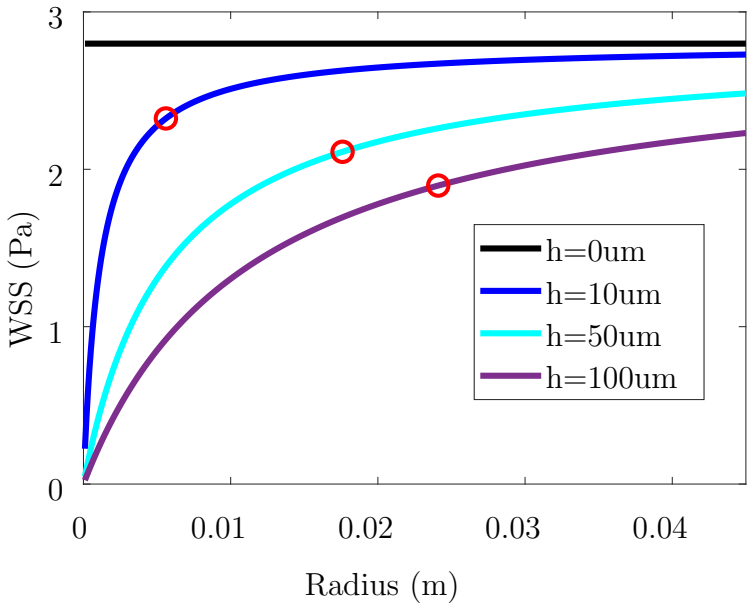

Figure 2.21: Shows the effect of gap height on the WSS profile as a function of radius. The red dot represents where the WSS is within 15% of the maximum WSS value for a 45 mm radius cone.

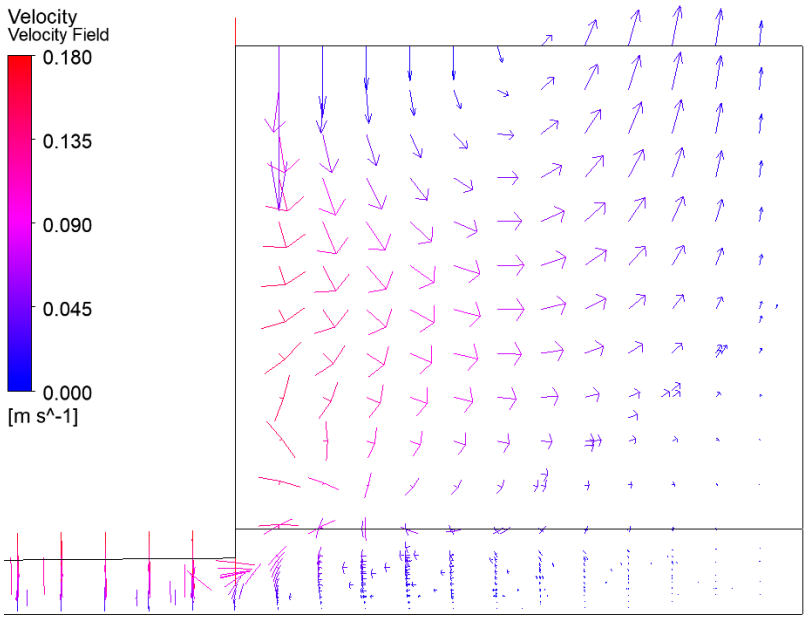

Figure 2.22: Vortex developed from a side view perspective to show the importance of vent boundary condition as opposed to symmetry on top.

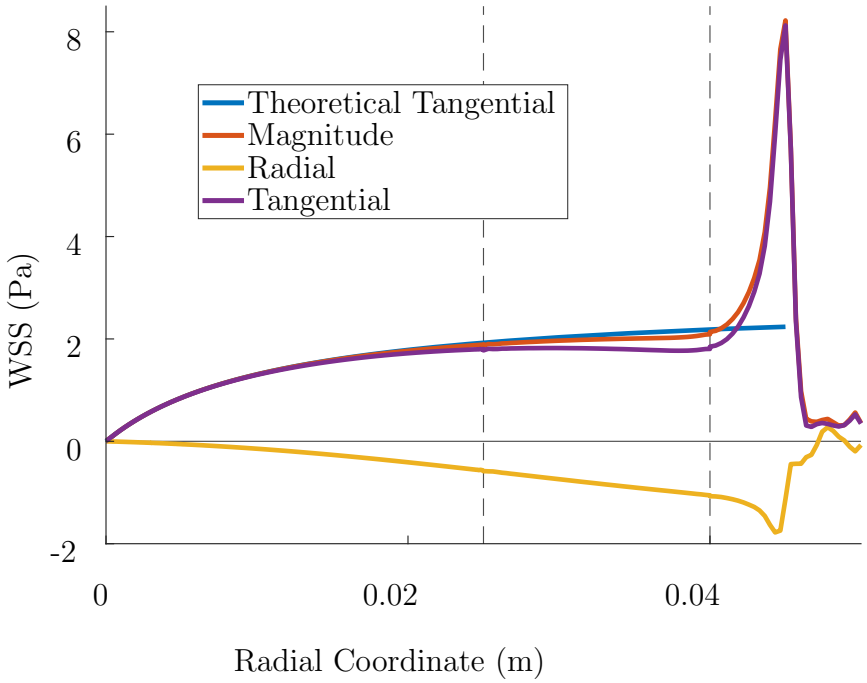

Figure 2.23: Shows component of WSS when $\widetilde{R}$=0.5 at 40 mm. Vertical lines indicate where cells would be seeded. Spike seems to signify that secondary flows are significant.

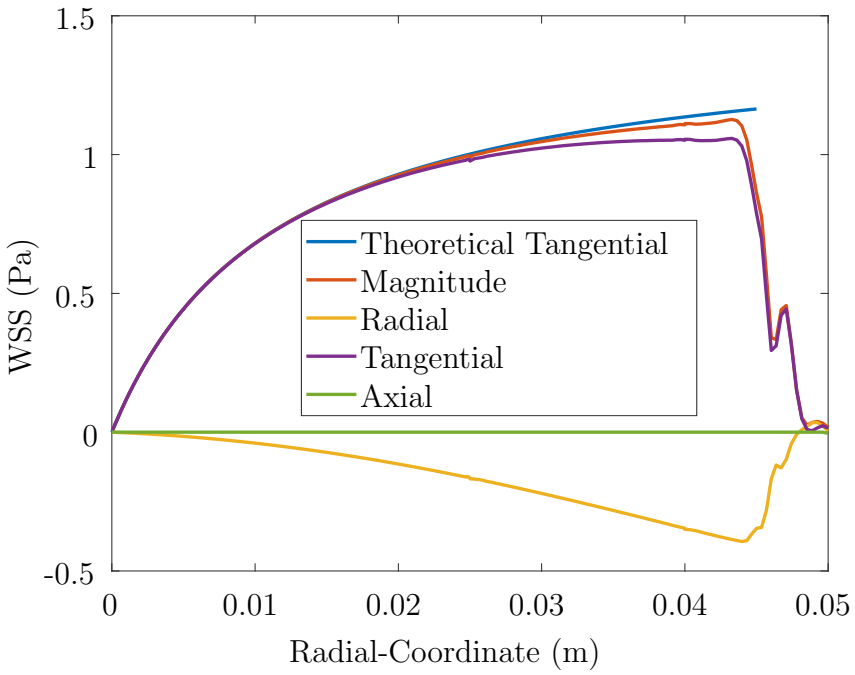

Figure 2.24: Shows the components of WSS when $\widetilde{R} = 0.5$. There is still a significant secondary (radial) flow, demonstrating the acceptable cutoff value for $\widetilde{R}$ is less than 0.5.

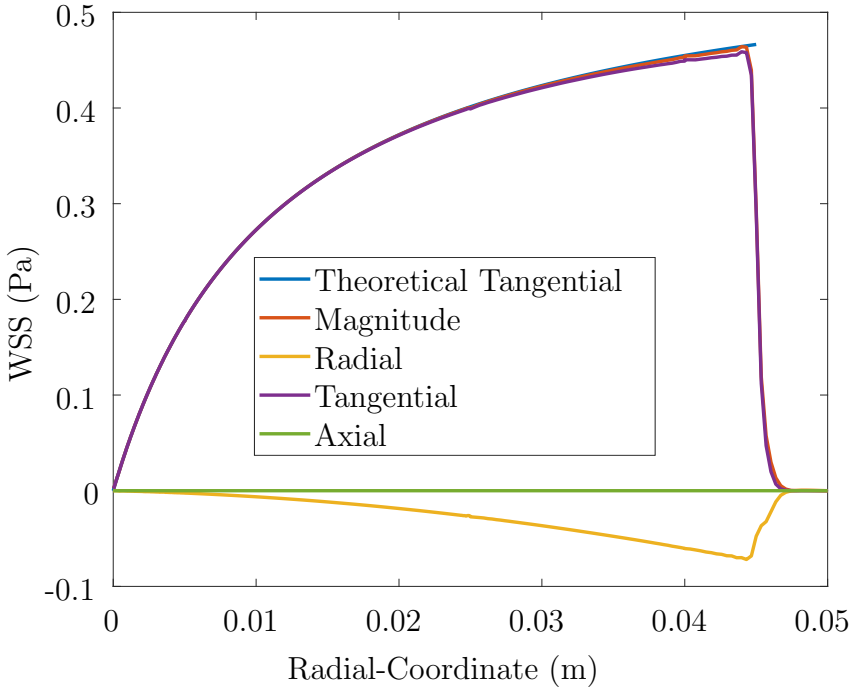

Figure 2.25: Shows the components of WSS when $\widetilde{R} = 0.2$ using the same fluid but decreasing the rotational speed of the cone. Radial WSS is no longer significant and the tangential WSS matches the magnitude of WSS well.

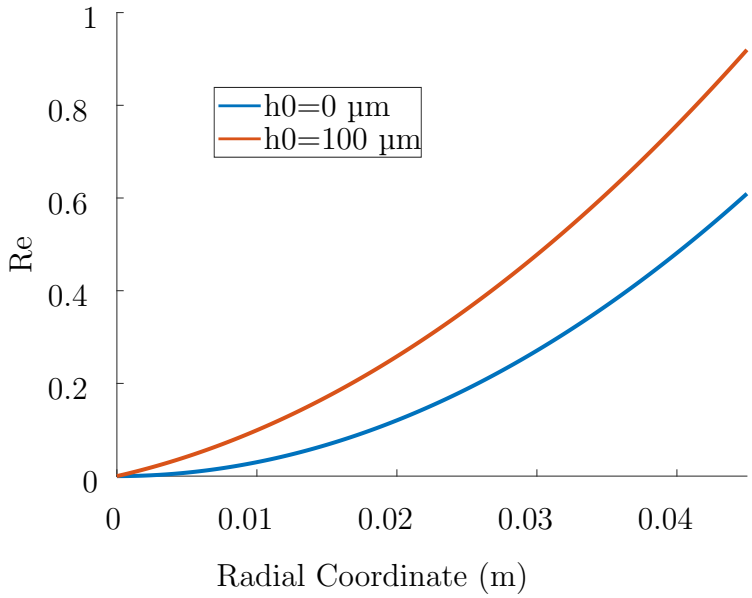

Figure 2.26: Compares $\widetilde{R}$ with and without accounting for the gap height as a function of cone radius.

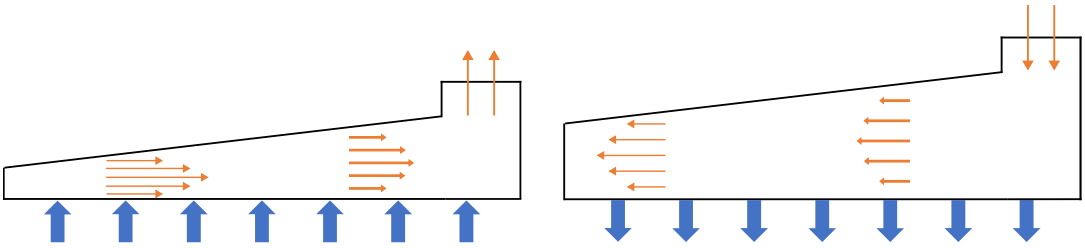

(a) Upward (b) Downward

Figure 2.27: Secondary Flow Concept with the effect of bottom boundary up and down vibration.

2.2.10 Secondary Flow Due to Vibrations

Since the bottom boundary is moving up and down, there will be displacement and replacement of fluid underneath the cone. It was learned from simulations that there will be a significant mass flow under the cone as the petri dish vibrates. This displacement of fluid will travel radially toward the outer wall of the Petri dish as the petri dish moves up, and toward the center as the petri dish goes down. It was found in preliminary simulations that under the current parameters, listed in Table 2.6, radial flow due to the vibrating bottom boundary dominates over the tangential flow from the cone. This is severely problematic, as this will only induce sinusoidal radial flow, which is not at all desirable. The flow field concept from this effect is visualized in Figure 2.27.

Not only is the radial shear the dominating direction of shear stress, but the magnitude is also largely problematic. The magnitude of WSS for this simulation was about 150 Pa and almost entirely in the radial direction. The goal is to obtain a maximum WSS magnitude of about 2.2 Pa with the flow mostly in the tangential direction. This means that the direction and magnitude are not at all close to representative of

the flow in the ICA.

Since this set of parameters is not sufficient for representing the flow in the ICA, a different set of amplitude and frequency will be found where the tangential shear, the desired shear direction, is the most prominent component. Since it has been shown that jerk, the time derivative of acceleration, is a factor that may play a significant role in genetic expression for mechanosensitive cells,[10] the maximum jerk will remain constant across simulation cases and the amplitude and frequency will be set accordingly.

The maximum jerk the cells will experience due to vibrations is defined as the following.

$$j = \omega^3 * a \tag{2.22}$$

Where ω is frequency and a is amplitude.

Since it is challenging to track a specific point on a moving wall for simulations in Fluent, the entire cell area was used to determine the average WSS over the area where the cells would be seeded. Also, the radial velocity at the interface walls located at 25 and 40 mm radially is tracked to analyze the velocity profiles at these areas throughout the simulations. From this, the theoretical WSS will be analyzed and compared so that the ideal parameters for amplitude and frequency can be estimated.

The goal of this section is to derive an equation for the radial velocity caused by vibrations with the intention of determining what vibration parameters are necessary

to induce low enough radial shear stress to induce relevant shear stress magnitudes as well as direction onto ECs. Because preliminary simulations done by our lab show an angle of sudden changes in the WSS direction of about 10 degrees, this will be our acceptable threshold; +- 10 degrees. These results have not yet been published.

In order to derive an equation for the radial velocity based on the changing volume of the fluid domain under the cone, the integral form of continuity will be assessed to determine the average radial velocity with respect to the vibration frequency and amplitude. For this analysis, only the portion of fluid under the cone will be analyzed. This means the two parameters to look at in the continuity equation are the change in fluid volume and the change in cross-sectional area normal to the radial flow.

$$\frac{\partial}{\partial t}\int_{CV}\rho r dV + \int_{CS}\rho(\vec{V}\cdot\vec{n})rdA \ = 0 \tag{2.23}$$

Since the radial flow is to be isolated and analyzed, tangential flow will be neglected for this equation. Thus, $\vec{V} = V_r\hat{r} + V_\theta\hat{\theta} + V_z\hat{z} = V_r\hat{r}$. Then, when the integrals in equation 2.23 are expanded in 3D cylindrical coordinates, we get the following.

$$\frac{\partial}{\partial t}\int_0^{h_0+r\alpha+a\cos(\omega t)}\int_0^r\int_0^{2\pi}\rho r d\theta dr dz + \int_0^{h_0+r\alpha+a\cos(\omega t)}\int_0^{2\pi}\rho V_r r d\theta dz \tag{2.24}$$

Where r is the radial coordinate of the cone, and the change in height due to vibrations is $h_0 + r\alpha + asin(\omega t)$, where a is the amplitude of vibration (half the displacement), ω is the frequency, and t is time.

The two components of equation 2.24 will be separated and analyzed individually for convenience.

When focusing on the control volume side (left) of the equation:

$$\frac{\partial}{\partial t}\int_0^{h_0+r\alpha+a\cos(\omega t)}\int_0^r 2\pi\rho dr dz \tag{2.25}$$

$$\frac{\partial}{\partial t}\int_0^{h_0+r\alpha+a\cos(\omega t)} r^2\rho\pi dz \tag{2.26}$$

$$r^2\rho\pi\frac{\partial}{\partial t}\Big(h_0+r\alpha+a\cos(\omega t)\Big) \tag{2.27}$$

$$-r^2\rho\pi\omega a\sin(\omega t) \tag{2.28}$$

Now the right side, the control surface side, will be solved for.

$$2\int_0^{h_0+r\alpha+a\cos(\omega t)}\rho V_r r\pi dz \tag{2.29}$$

$$2\rho V_r r\pi\Big(h_0+r\alpha+a\cos(\omega t)\Big) \tag{2.30}$$

Then substituting in the simplified equations into continuity yields

$$2\rho V_r r\pi\Big(h_0 + r\alpha + a\cos(\omega t)\Big) - r^2\rho\pi\omega a\sin(\omega t) = 0 \tag{2.31}$$

Cancelling like terms yields

$$2V_r\Big(h_0 + r\alpha + a\cos(\omega t)\Big) = r\omega a\sin(\omega t) \tag{2.32}$$

Then solving for V_r

$$V_r = \frac{-ra\omega\sin(\omega t)}{2\Big(h_0 + r\alpha + a\cos(\omega t)\Big)} \tag{2.33}$$

The transient average velocity based on Equation 2.33 is plotted for the two bounding radii where cells will be seeded as well as a radial coordinate in the middle (33mm) in Figure 2.29. The location of these points on the cone and plate are shown in Figure 2.28. It is seen in Figure 2.29 that the velocity is greater for larger radial coordinates. This agrees with Figure 2.30, which shows an increase in velocity as the radius increases.

There are three radial coordinates that will be focused on for the remainder of this analysis: 0.025, 0.033 and 0.04 m radially. The bounds of the ECs will be 25 to 40mm, and 33mm is the centroid of the area where the cells will be (and therefore where the average WSS will be measured).

Two simulations with different vibration amplitudes are compared. The amplitudes of these cases are 50 and 10 μm (for total bottom plate sinusoidal displacement of 100 and 20 μm). Any spatially dependent plots are based off of the time point where

the radial velocity is highest. This makes it simpler to take a specific time point in the simulations and compare it to the numerical model yielding Equation 2.33.

Figure 2.29 shows two periods of the theoretical radial velocity of the fluid along the fluid domain exposed to 100 Hz vibrations at 50 μm amplitude (100 μm total displacement). In addition, the 20 μm displacement case is compared to the 100 μm displacement case in Figure 2.33. The 100 μm case has a much higher average velocity. This is expected, as the maximum level of jerk is constant across simulations, and will therefore be increasing the frequency in order to decrease the amplitude of vibrations, as seen in and Equation 2.22.

It can also be seen in Figures 2.33 and 2.34 that the velocity at r=40 mm will be greater than the velocity at r=25 mm. As aforementioned, because of the fact that maximum jerk is being held constant across all simulations, and thus the maximum speed of the bottom boundary is greater, there is an increasing maximum average velocity as the amplitude of vibration increases.

Also, the average velocity and WSS on the bottom surface as functions of the radial coordinate are shown in Figure 2.30 and Figure 2.31 respectively. The velocity profile shown in Figure 2.32 shows the theoretical velocity profile at this time step using the parallel plate Poiseuille flow definition for velocity shown in Equation 2.39. A parallel plate assumption is made in order to use a simplified equation that will provide a useful estimate for the amplitude and frequency of vibrations needed to reduce the amount of radial flow. A limitation of this equation being used is of course that these are not parallel plates, but the equation was modified to account for this

changing height along the radius for a more accurate estimate of the radial velocity.

Since the bottom boundary is moving, it is much less trivial to track the WSS at a specific point throughout the simulation in ANSYS, as the bottom plane is changing its vertical position each time step. Therefore, the average velocity over the entire cell surface is tracked over time. The centroid of the area of the cells is about 0.033 m radially. The simulations have a maximum average WSS of 152 and 52 Pa in the cell area for 100 and 20 μm displacement respectively. When compared to the theoretical WSS value from Equation 2.35 at 0.033 m of 152 Pa, there is a a 5.2% error for the 100 μm case. For the 20 μm case there was a 7.5% error at 0.033 m. This may be due to the fact that the CPV geometry is not a parallel plate and that there will be a consequential acceleration of the fluid increasing toward the center of the cone. This may cause the solution to slightly deviate from the theoretical profile.

As seen in Figure 2.37, the theoretical and actual profiles for the cone area match very well. The slight deviation is most likely due to the transient effects of the system, as that will cause a slight delay between the edge and center of the fluid domain. Nonetheless, the results match well and show the numerical model accurately approximates the flow and WSS of the fluid domain.

Now, the critical amplitude where the WSS is dominated by tangential flow is calculated by a maximum allowable radial flow of 10% of the desired tangential flow. Thus the maximum radial flow can be $2.2 * 0.1 = 0.22$ Pa for the defined parameters.

It is known from Figure 2.35 that the maximum WSS value where the cells will be seeded is at 0.025m. Maximum jerk is constant across simulations, so with a given

range of amplitudes, the frequencies are also known. It is necessary to know what the critical amplitude would be at the point in time where velocity is maximized for a worst-case scenario condition of radial flow. Thus, a fourth of the period is used for each frequency, for the maximum of a sine wave is at a fourth of the frequency. With those values, the velocity was calculated with Equation 2.33 as a function of amplitude. Then, the WSS as a function of amplitude was calculated with Equation 2.34, and is also shown in Figure 2.38.

It may be possible to vibrate the entire CPV apparatus to prevent any flow field effects from the vibrations, but this would require a very precise and fine-tuned system that is not adversely affected by vibrations, such as a motor and encoder which are known to have issues with vibrations, making this device not a realistic solution. Since it is not feasible to use this device for this application, a PPFC will be designed for this application instead. A PPFC is not only able to vibrate as a whole device but is also much simpler to design and manufacture. The downside of using a PPFC rather than a CPV is that the PPFC is driven by a peristaltic pump, which induces slightly less robust waveforms than a CPV is capable of inducing. Another benefit of the PPFC is that the size is typically smaller than a CPV system. Nonetheless, the trade-off of ease of design and manufacturing as well as inducing relevant vibrations without adversely affecting the flow field makes the PPFC a more suitable device for this application.

$$\tau = \frac{6\mu V_r}{h_0 + r\alpha + A} \tag{2.34}$$

Again, the radius for Equation 2.34 will be 25 mm (0.025 m), as that is the radial coordinate where the maximum WSS will be where cells would be seeded as seen in Figure 2.31.

The critical amplitude was calculated as the maximum vibration amplitude that would result in less than 0.22 Pa of radial WSS so that the tangential direction of flow velocity would dominate the radial direction. The critical amplitude was found to be 4.4 nanometers as seen in Figure 2.38, resulting in 8.8nm of displacement, where the tangential flow will dominate the fluid flow rather than the radial flow to best mimic the flow in the ICA. This is by no means a realistic amplitude to practically induce, as controlling vibrations on the order of nanometers is extremely challenging, as well as the challenge of accurately calibrating such a fine-tuned system. Also, at that level, the amplitude of vibrations may even be so small that the cells won't experience any effect.

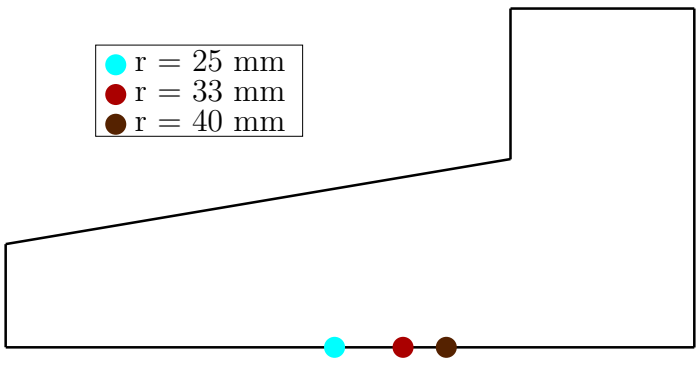

Figure 2.28: CPV Radial coordinates analyzed.

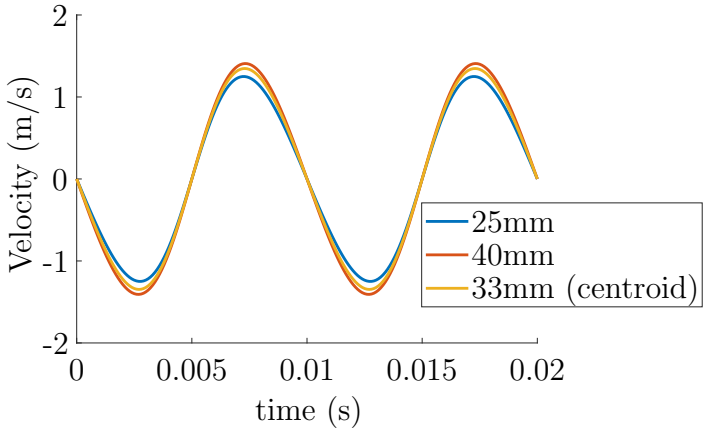

Figure 2.29: Theoretical average velocities over two periods of vibration at 100 Hz and 50 μm amplitude (100 μm displacement) for 25, 33, and 40 mm.

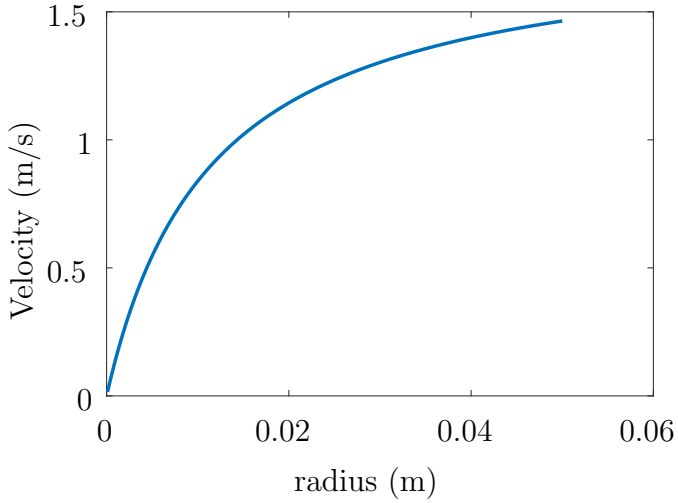

Figure 2.30: Average radial velocity as a function of the cone radius with a vibration amplitude of 100 μm and frequency of 100 Hz.

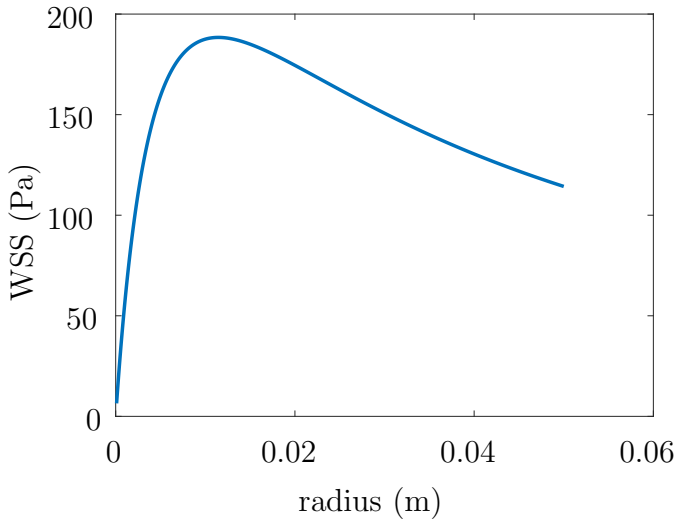

Figure 2.31: WSS as a function of cone radius with a vibration amplitude of 100 μm at maximum radial average velocity.

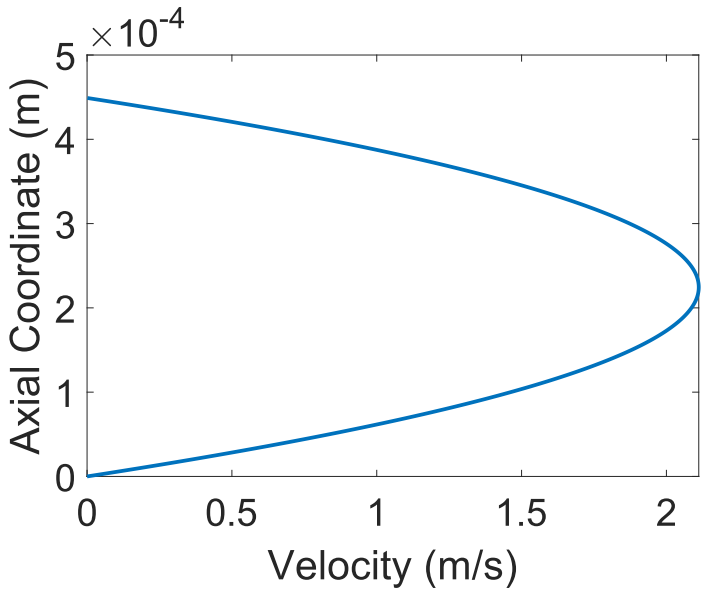

Figure 2.32: Velocity as a function of axial coordinate (height).

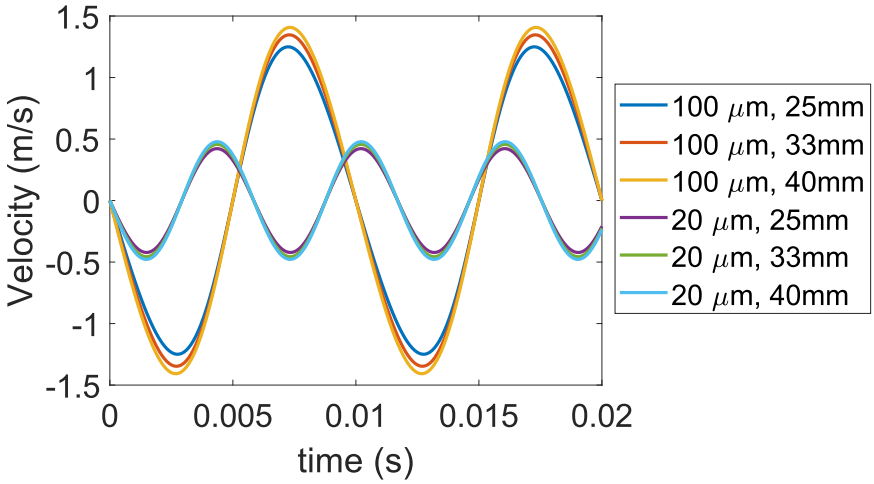

Figure 2.33: Theoretical average velocities over two periods of vibration at 100 Hz and 100 and 20 µm displacement (50 µm and 10 µm amplitude) for 25, 33, and 40 mm.

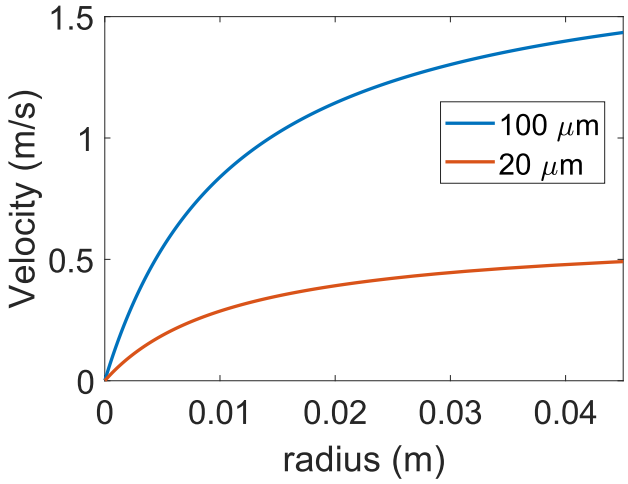

Figure 2.34: Maximum radial velocity as a function of radius for 100 and 20 µm.

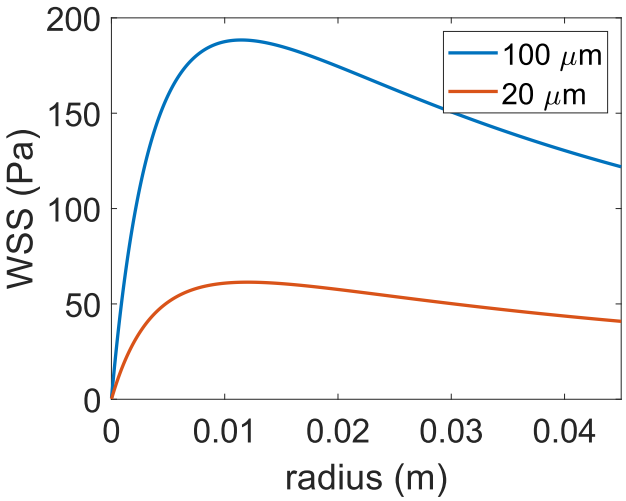

Figure 2.35: Maximum WSS as a function of radius for 100 and 20 μm.

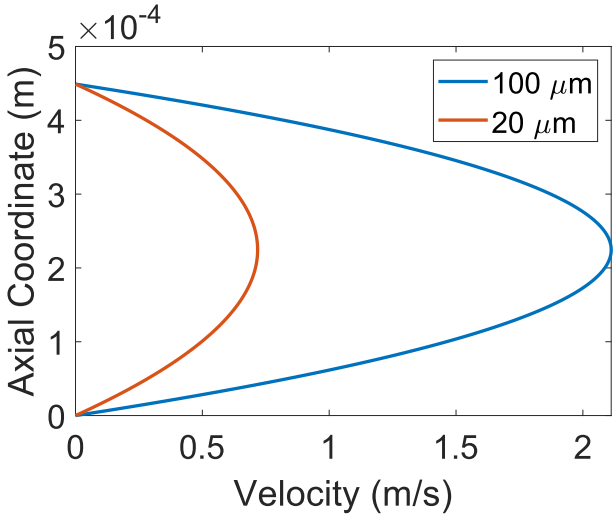

Figure 2.36: Velocity as a function of axial coordinate (height) for 100 and 20 μm.

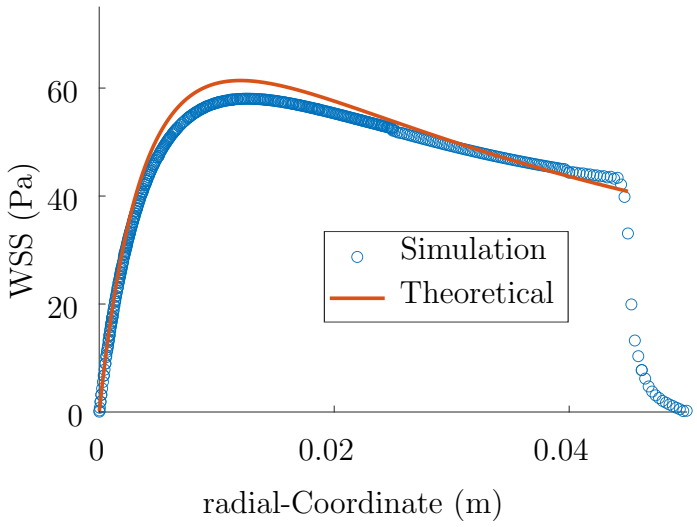

Figure 2.37: Compares theoretical (red line) to simulation (blue circles) WSS as a function of the radial coordinate with 20 $up\mu$m displacement at time t=0.0162 seconds.

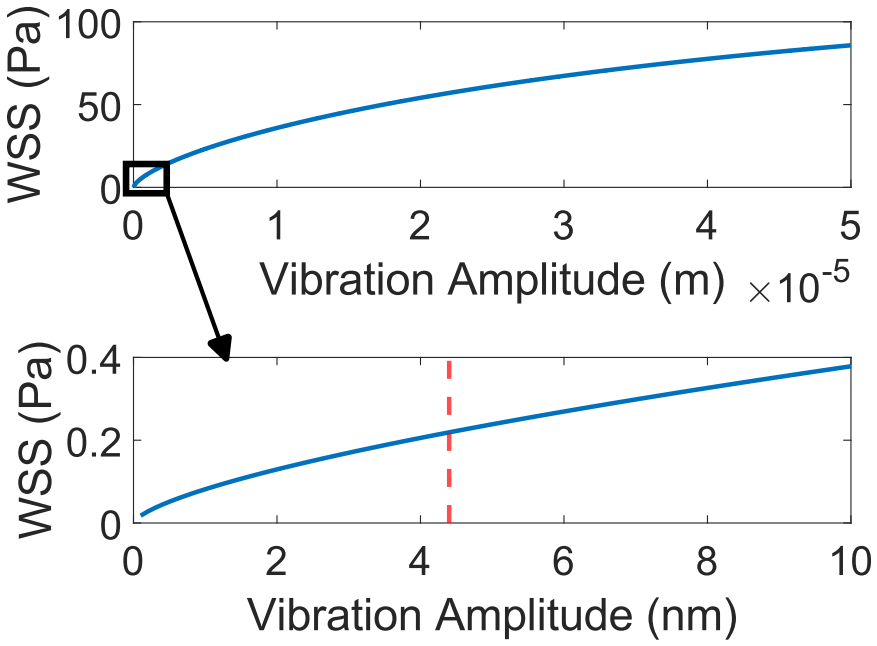

Figure 2.38: Radial WSS as a function of vibration amplitude for the CPV. Amplitude ranges from 0 to 50 µm (top) for a maximum total displacement of 100 µm. A red dotted line in the zoomed in plot (bottom) shows the vibration amplitude for the maximum acceptable radial WSS (bottom).

2.3 PPFC

A PPFC is designed, simulated and fabricated instead of a CPV primarily because of the necessary advantage that vibrations can be induced without any volumetric flow or compromising the fluid flow field, as was found in the CPV. The tradeoff is that a more complex pump system will be required to induce pulsatile waveforms from a peristaltic pump, but that is compromise well worth taking for a functioning setup. The WSS in a CPV that does not vibrate is driven simply by motor speed (assuming the test fluid is Newtonian), while a peristaltic pump will most likely have some error in the flowrate waveform because of the impulsive changes from the rotors driving the flow. This effect of the pump will not be characterized in this research as this study is focused on the device design, proof of concept, and fabrication. The shear stress between two wide parallel plates away from all walls is defined as follows:

$$\tau = \frac{6\mu Q}{wh^2} \tag{2.35}$$

where Q is flowrate, w is chamber width, and h is chamber height. Then the average velocity is calculated with $Q = AV$ where A is the cross-sectional area (m^2) of the PPFC and V is the average velocity (m/s).

The design goals of this device should be clearly defined in order to provide a clear and productive design process. The design requirements are as follows:

1. Can be vibrated without flow field distortion
2. Relevant components can survive the autoclave for sterilization (max temperature of 105°C
3. Bio-compatibility of components that may contact cells or fluid
4. Uniform flow for consistent WSS over the cell area
5. Portion of the cell region visible for PIV
6. Small enough to fit into a 12 inch^3 incubator

Parallel Plate Flow Chambers are a common choice for hemodynamic analyses.[68,70,84,104,123] When the flow is laminar, it can be approximated by Poiseuille flow for parallel plates, which is shown in Figure 2.39 and the velocity is shown in Equation 2.39, and shear stress in 2.35.

The main goal of this device, as was with the CPV, is to expose ECs to a predictable, transient, and physiologically relevant shear stress waveform as well as vibrations. The entire PPFC will be vibrated in order to maintain a constant fluid domain and expose ECs to physiologically relevant vibration amplitude and frequencies that may occur in aneurysm-susceptible locations such as the internal carotid artery.

Many have used these devices for the specific application of exposing ECs to relevant shear stress magnitudes.[68,70,84,104,123] Typically, a PPFC cannot induce as robust waveforms as a cone and plate, leading to most studies implementing steady or slightly transient waveforms.

A practical goal in designing a PPFC is to minimize the entrance length of the flow, where the flow is not fully developed, in order to maximize the effective space of flow while minimizing the size of the device. In many flow chambers the inlet feeds

directly into the main chamber, causing a greater entrance length because the flow must become uniform across the width of the chamber. The entrance length will be minimized by forcing the flow into small ovular pools that span the width of the device and cause fluid to divert across the width of the chamber before flowing across the main chamber area. The general schematic of the device can be seen in Figure 2.41.

The flow will enter in the inlet side which is labeled by an asymmetrical cut in the corners of the device as seen in Figure 2.41. It technically does not matter which side is the inlet or outlet, as the fluid mechanics are equivalent either way, but for the sake of experimental consistency, the inlet is labeled. Then flow will distribute across the ovular pools outward and be forced into the main area of the chamber where the cells are seeded. The Reynolds number for fully developed parallel plate flow away from the walls is defined as follows.

$$Re = \frac{Q\rho}{bh^2} \tag{2.36}$$

Where Q is the flow rate (2.9e-6 m^3/s), ρ is the fluid density (1015 kg/m^3), b is the width of the chamber (0.0635 m) and h is the height of the flow chamber (0.001 m). This leads to a Reynolds number of 7.5, which is in the laminar regime.

The outer 5 mm on each side wall will not be seeded with cells due to the large velocity gradient near the wall. The wall shear stress should be constant along cell areas. The cells will be seeded at least 10 mm from the edge of the inlet and outlet pools so that the cells will experience uniform shear stress and avoid the entrance

length where the flow is not fully developed. The theoretical entrance length is about 0.3mm for the current design parameters assuming the average velocity is constant along the cross-section of the device based on the following equation.

$$L_e = 0.04h * Re \tag{2.37}$$

Where Re is the Reynolds number and h is the chamber height.

This is also assuming the inlet is the same shape as the main channel of the flow chamber, which it is not. The inlet comes in through a circular tube and diverts the flow across the channel to develop the flow. The entrance length will therefore be greater than the theoretical value. Based on the 3D simulations, there is less than a 2% difference between the minimum and maximum values for WSS in the cell area based on Figure 2.44. This means the cells will experience approximately the same WSS independent of location on the glass slide, demonstrating the flow has developed.

In order to machine the PPFC, all of the dimensions are in US customary units because the UMass machine shop uses US customary unit tools. Figure 2.40 and Table 2.7 show the dimensions of the PPFC for the fluid channel. There will be an O-ring seal around the device. Originally the O-ring was also going to serve as the height of the flow chamber, but it was determined that having a rigid wall as the offset would offer a more consistent height throughout the chamber. If the O-ring were to serve as the height of the chamber when compressed a certain percentage, there is a chance that some portions would be more compressed than others, resulting

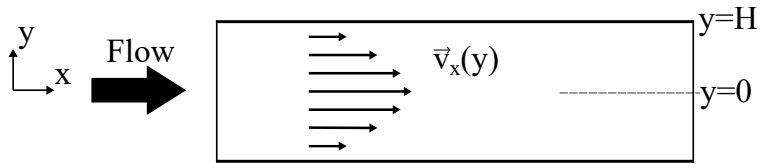

Figure 2.39: Poiseuille flow for 2D parallel plate laminar flow.

in an inconsistent height and thus an inconsistent flow field.

Another goal of this device is to, in one experiment, obtain both the protein and mRNA expression of the cells. Thus, there will be two side-by-side glass slides exposed to the same flow field. This means the chamber will have to be more than 50 mm wide and 75 mm long to fit two side-by-side glass slides that are each about 75x25 mm along with some clearance away from the walls to ensure a uniform WSS across the cells. It is also desirable to have a ridge between the glass slides so they are not touching.

Table 2.7: Dimensions of the PPFC

Feature	Inches	mm
L1	4	101.6
L2	4.5	114.3
L3	0.375	9.53
W	2.35	59.7
R	0.125	3.18
H	0.0394	1

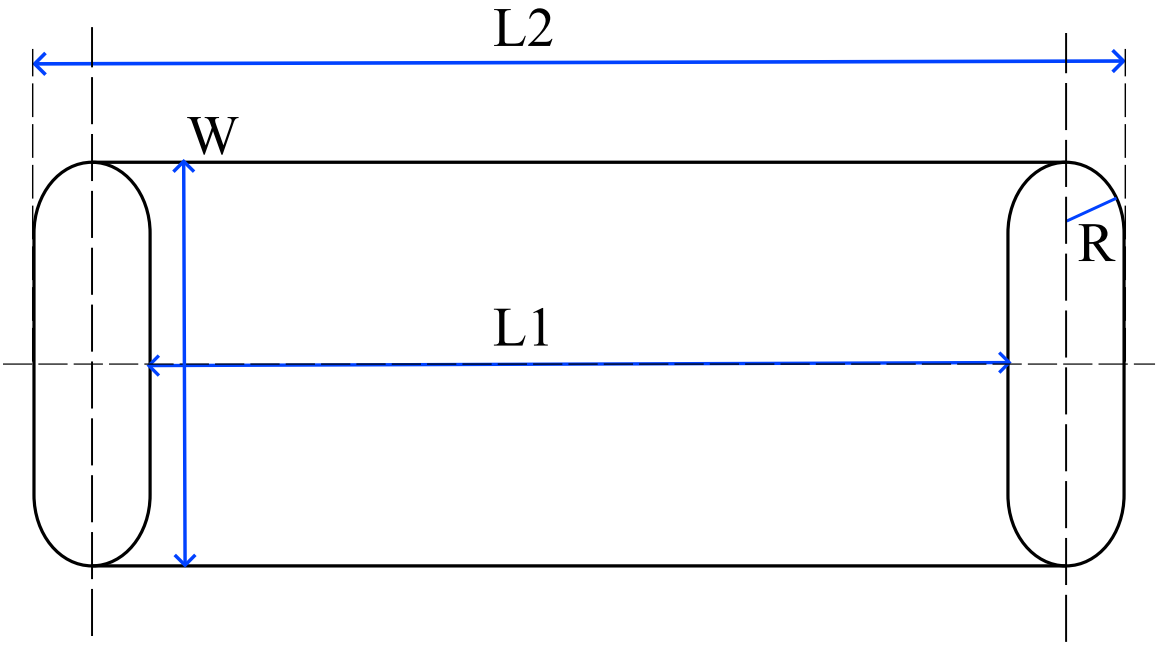

(a) PPFC dimensions.

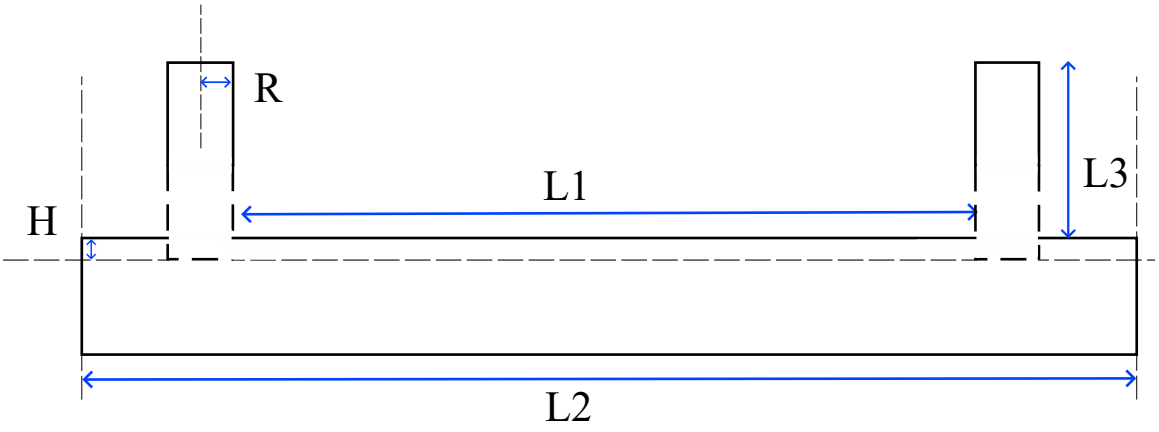

(b) More dims

Figure 2.40: PPFC dimensions top and side view

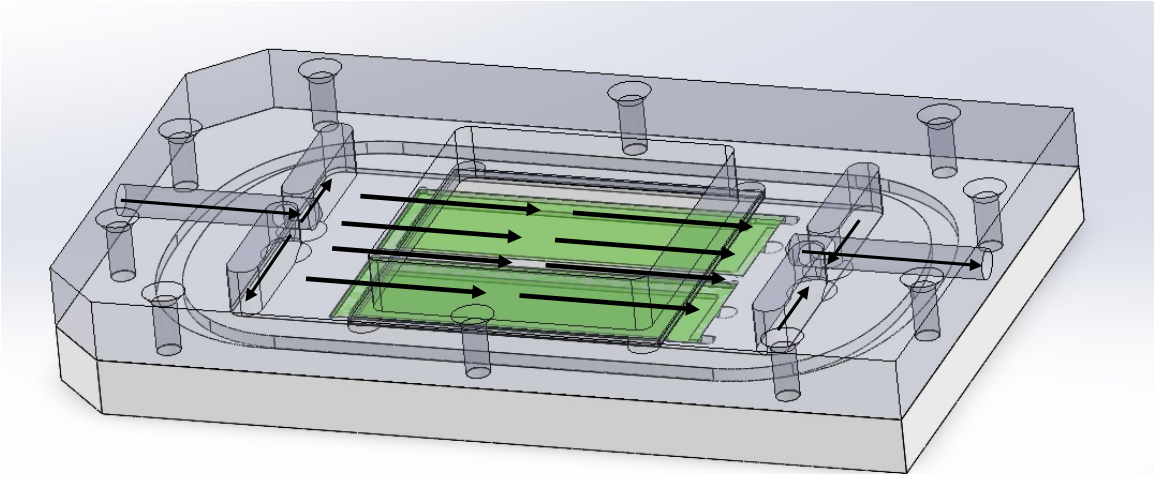

Figure 2.41: PPFC CAD model. Shows how fluid flows through the chamber. Green rectangles represent glass slides with cells. The square cutout is for a glass window for PIV.

2.3.1 2D Simulation Verification

In order to increase computational efficiency, a 2D case will be compared to the 3D case to investigate whether a 2D approximation can be made in order to only simulate the cross-sectional region where the cells will be seeded. First of all, the same number of height-wise mesh elements should be used, meaning the number of layers will be 8 for the 2D and 3D simulations, and the element and orthogonal quality will again be at least 0.2. This will make the 3D and 2D cases approximate in terms of the meshing. In terms of the 2D simulation setup, the inlet will be simulated as coming down from the top of the inlet pool, as will happen in vitro.

Since it is not yet known whether this specific mesh will be considered an asymptotically relevant solution according to a mesh independence test, the numerical results will not be used as a proof of accuracy, but rather a proof of concept to show that the 2D and 3D cases are consistent across the cell area, which is the region of interest. Once the 8-layer mesh is shown to match in terms of the 2D and 3D case results, a mesh analysis will be performed on the 2D case. The different lines where WSS data is being extracted are shown in Figure 2.42.

Since the flow should be laminar Poiseuille flow in the cell area, the inputted mass flow rate can be calculated from the average velocity. The average velocity value that corresponds with a wall shear stress value of 2.2 Pa for the given dimensions of the PPFC will be 0.052 m/s based on Equation 2.35. This leads to an inlet mass flow rate of 0.053 and 0.0034 kg/m^3 for the 2D and 3D cases respectively based on Equation 2.38.

$$\dot{m} = \frac{\tau w h^2 \rho}{6\mu} \tag{2.38}$$

Mass flow is needed because Fluent uses mass flow as an input. It is known that the velocity profile through a straight rigid duct with distance between walls H as a function of height is defined in Equation 2.39.

$$u(z) = u_{max}\left[1 - \left(\frac{2z}{H}\right)^2\right] \tag{2.39}$$

where z is the mid-line of the flow.

There cannot be a significant difference in the WSS profile perpendicular to the flow in the relevant area where the cells will be in order to safely assume a 2D case can be used and is relevant for this application. The perpendicular WSS profiles are compared in Figure 2.43. Also, as seen in Figure 2.45 the WSS across the cell area is nearly constant. Given that the maximum range of WSS magnitudes at relevant sites is less than 5% of the magnitude, the difference is not significant and a 2D approximation can be used based on the steady simulations. A WSS vector field is shown in Figure 2.47 for visualization of the WSS across the bottom of the chamber.

Even though the WSS magnitude is slightly different along the cell area, this would not have an adverse effect on cells, as the magnitude range is rather small as seen in Figure 2.43 (less than 0.1 Pa).

The velocity profile was found to fit well with the theoretical velocity profile, con-

firming Poiseuille flow for two parallel plates. According to the curve in Figure 2.46, the maximum velocity of the flow will be 0.077 m/s. This leads to a 1.8% error with the theoretical maximum velocity for parallel plate Poiseuille flow for the 3D case.

There is a 0.68% difference between maximum velocities for the 2D and 3D cases; 0.0764 (see Figure 2.48) and 0.0769 (see Figure 2.46) m/s respectively. Also, there was a 1.6% difference between the average WSS over the cell area for 2D and 3D cases; 2.113 (see Figure 2.49) and 2.148 (see Figure 2.44) Pa respectively. It can then be assumed that the 2D and 3D cases will yield approximately the same result, so 2D simulations will be used for transient simulations.

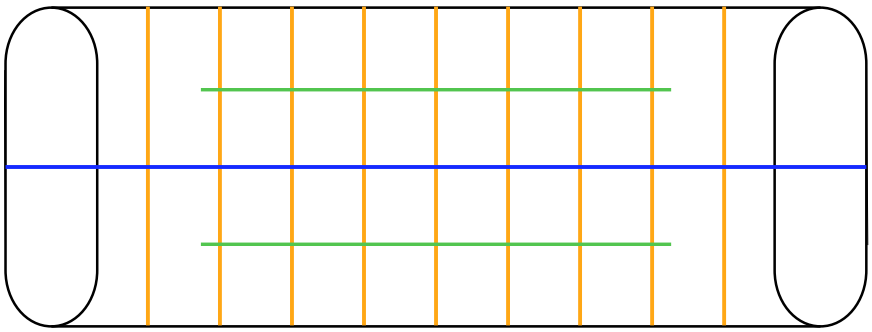

Figure 2.42: WSS data exported for 3D case. The blue line is the mid-line of the flow chamber axially along the flow. The green lines are the mid-lines for the two glass slides that span 75 mm across the flow chamber. The orange lines are perpendicular to the flow to verify the ECs are not too close to the walls at any axial location.

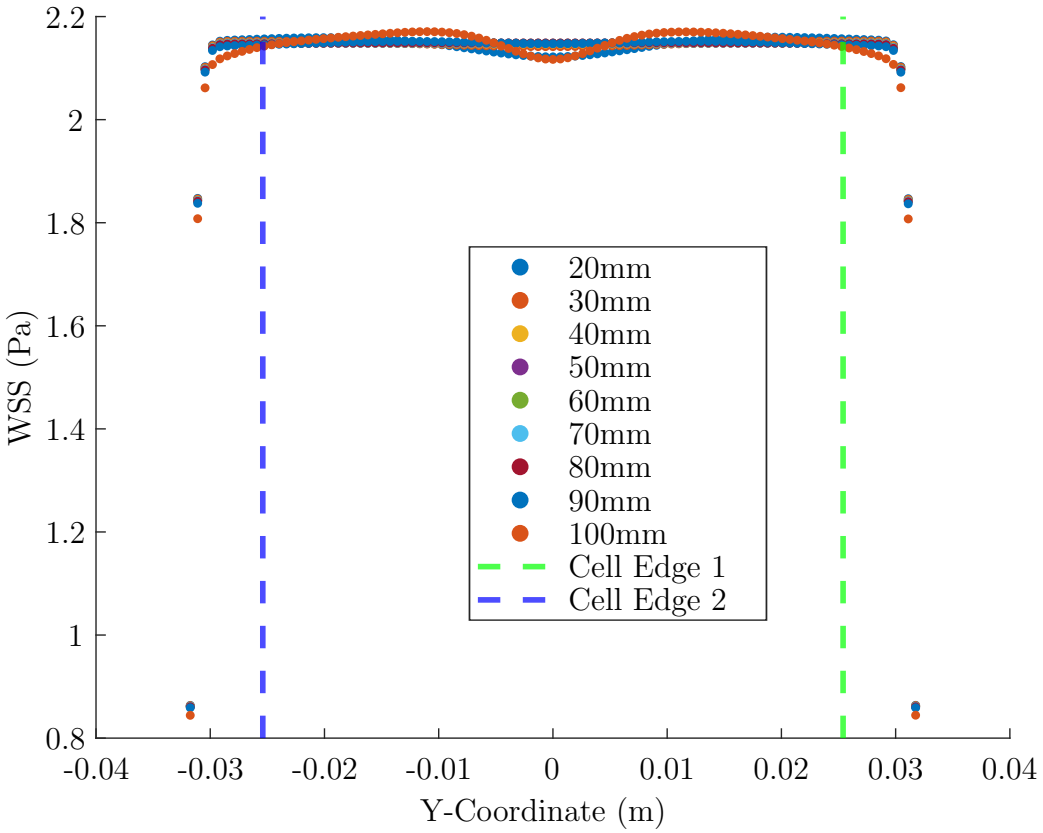

Figure 2.43: WSS data perpindicular to flow every 10mm near where ECs will be.

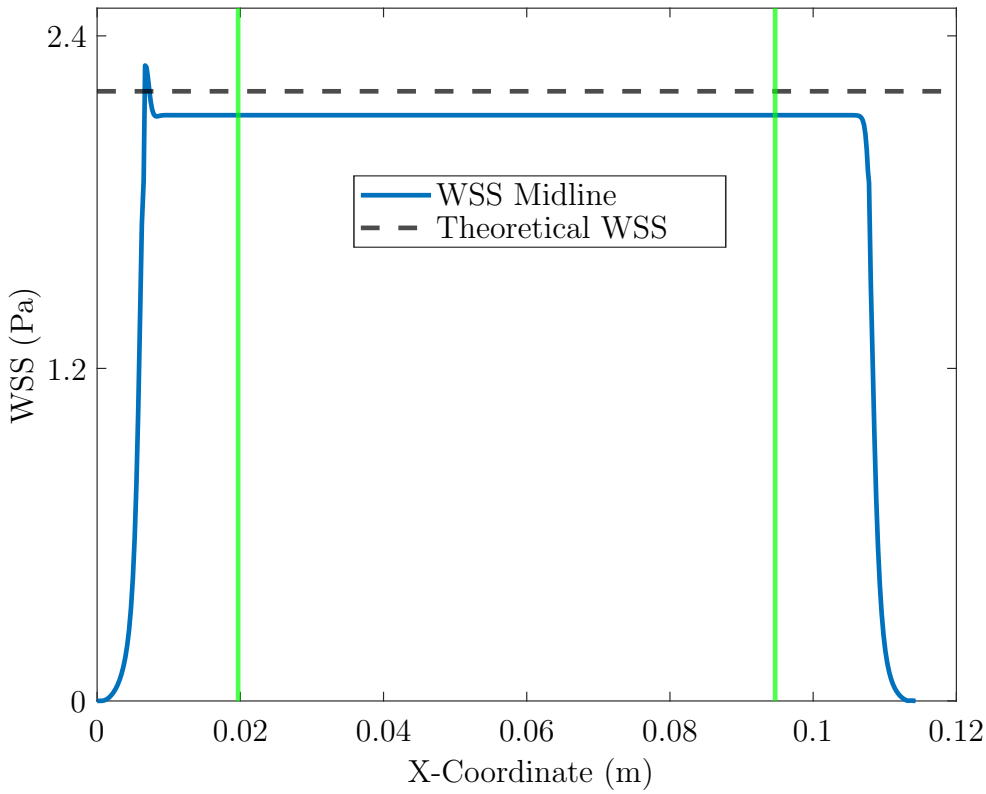

Figure 2.49: WSS along PPFC for the 2D simulation. The dotted line is the theoretical value of 2.2 Pa and the green lines show the bounds within which the ECs will be.

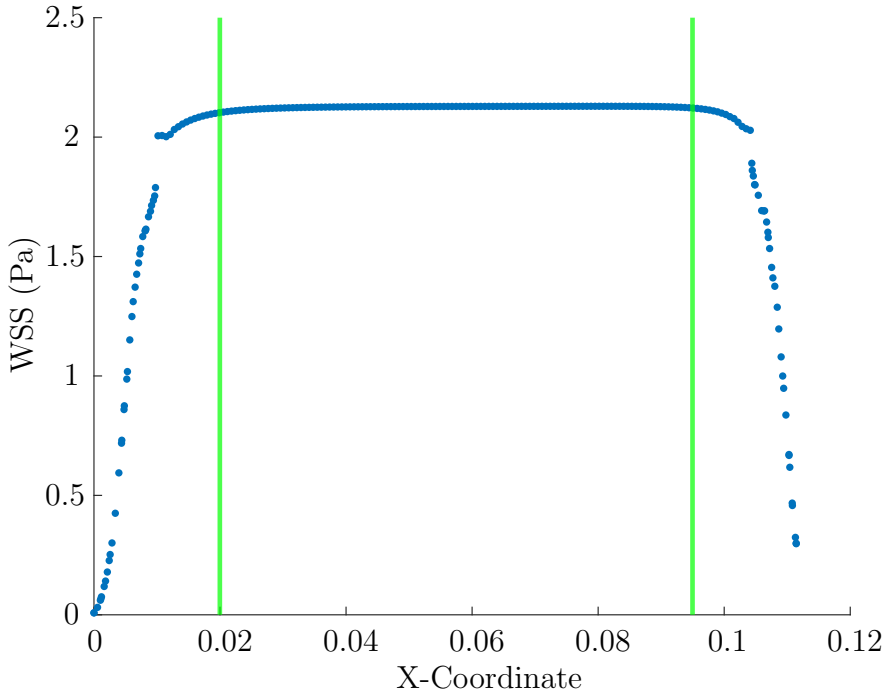

Figure 2.44: WSS along PPFC for 3D simulation. Between the green lines are where cells will be seeded.

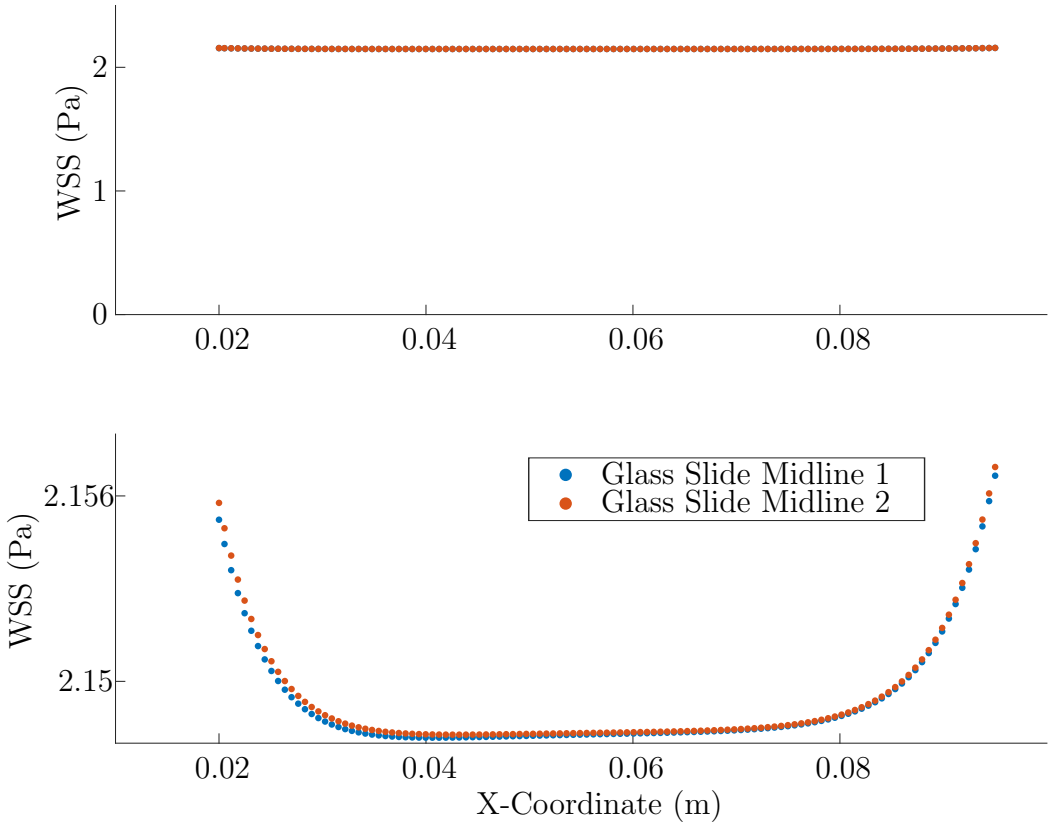

Figure 2.45: WSS along the mid-line of the EC area for 3D simulation. The top and bottom are the same plot, the bottom is zoomed in on the y-axis.

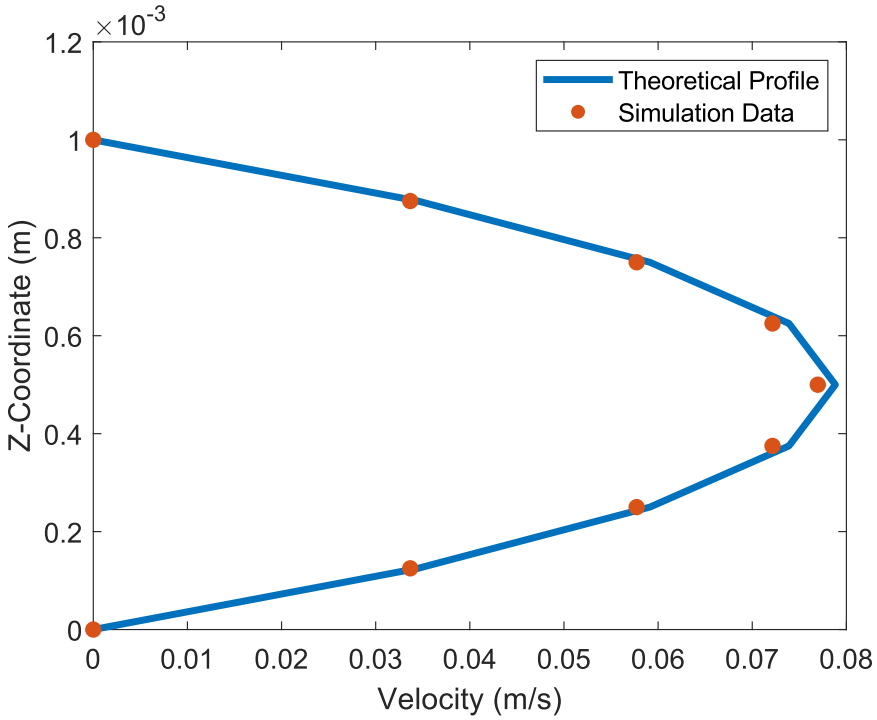

Figure 2.46: Velocity profile in PPFC to verify Poiseuille flow for the 3D simulation.

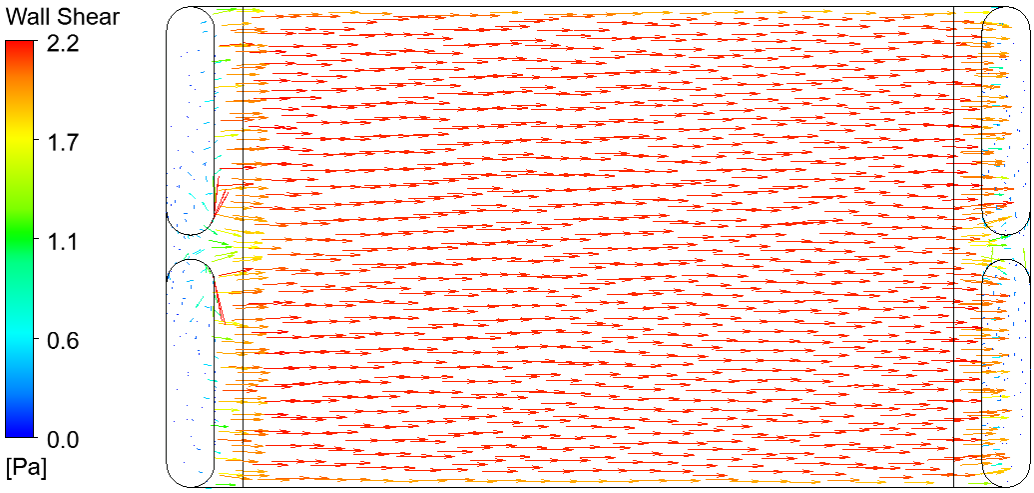

Figure 2.47: Shows a vector field of the WSS on the bottom plate for the 3D simulation. Little to no variation is visible away from the walls, inlet or outlet

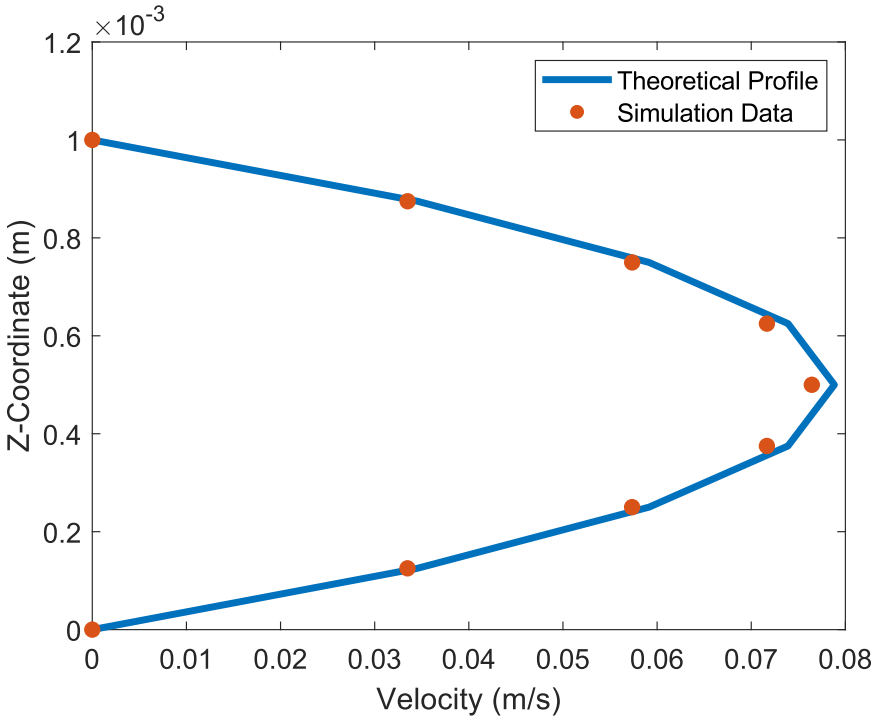

Figure 2.48: Velocity profile for 2d simulation.

2.3.2 Mesh Independence Test

In order to ensure the use of a sufficient mesh, the Richardson Extrapolation method will be used as well as tracking variables over space. In order to see whether the WSS converged based on the mesh, the average WSS over the mid line along the flow will be the compared parameter. Three meshes will be compared at a time to determine when a group of meshes is considered to converge to a solution according to the calculations of a Richardson extrapolation. The Richardson extrapolation has been used in various CFD applications.[71,111]

A grid refinement in a Richardson extrapolation should generally be greater than 1.1 to ensure that any convergence or computational rounding are not effecting the solution. For that reason, a grid refinement of 1.5 is used.

The starting mesh is 7 layers dividing the fluid domain vertically in the main chamber area, and when multiplied by the grid refinement ratio of 1.5 once and twice, that yields 11 and 16 layers (rounding up from 10.5 and 15.75 respectively). This led to a 7 layer mesh being the coarsest acceptable mesh according to the steady simulations because there is less than a 1% error in the Grid Convergence Index (GCI) values compared. However, it would be beneficial to extract data from the mid-line for a max velocity data point, so 8 divisions will be implemented so that a line of nodes is in the mid-line of the flow field because of an even number of layers in the mesh. This will also provide a safety factor for grid convergence, as the mesh is finer than necessary. Solving for the ratio of convergence is shown in Figure 2.50.

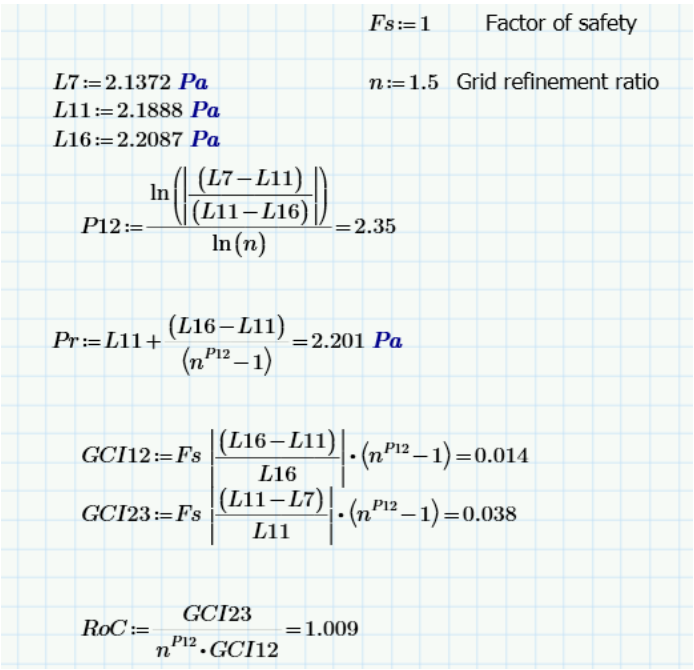

Figure 2.50: Richardson extrapolation calculations for mesh independence. A ratio of convergence (ROC) close to 1 shows the solution is asymptotic.

2.3.3 Transient Mass Flow

The relevant mass flow waveforms for both the upstream flow and aneurysm-susceptible flow were calculated from the WSS values from previous work in our lab that have not yet been published. Then, those mass flow waveforms are formatted and inputted to ANSYS as a transient mass flow inlet condition. This is the same process as the rotational speed waveforms for the CPV input boundary condition, except for the PPFC it will be a mass flow inlet condition. The waveforms for these two conditions can be seen in Figure 2.51.

As seen in Figure 2.52, there is little to no variation between cycles, and the maximum WSS is 2.145 Pa which is a 2.5% error with the theoretical max value of 2.2 Pa. This demonstrates that for the aneurysm-susceptible WSS transient case, the results are

consistent and predictable. There was also no effect of frame motion on the resulting WSS waveform to simulate vibrations of 100 μm and 100 Hz.

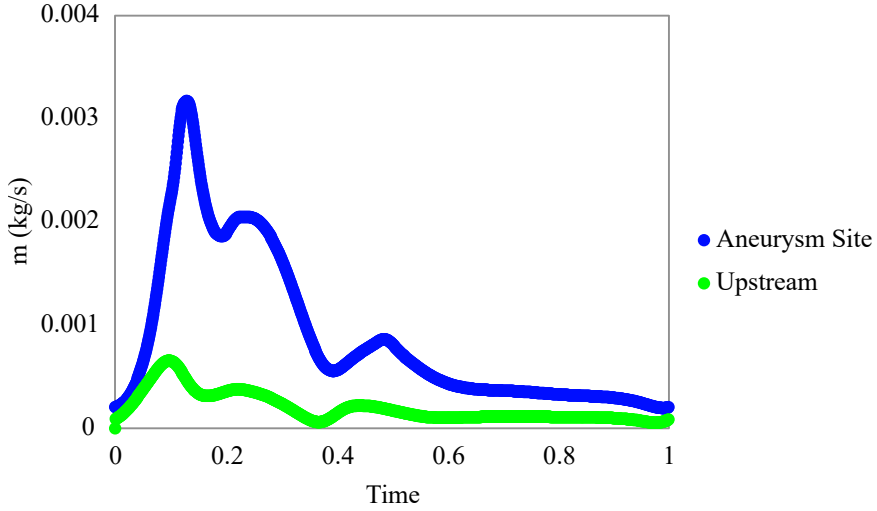

Figure 2.51: Mass flow profiles for the two test conditions; Aneurysm-susceptible (blue) and aneurysm-protective (upstream, green).

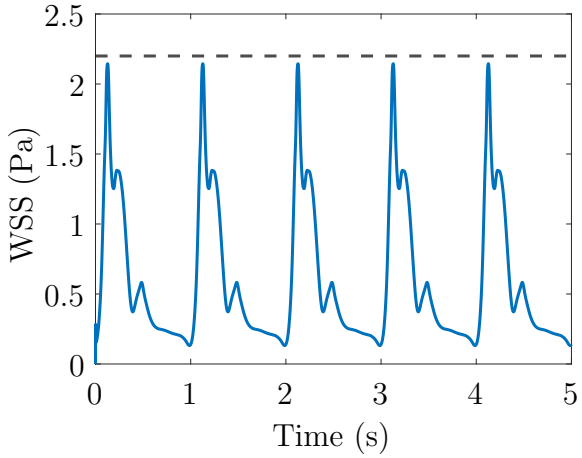

Figure 2.52: WSS on cells over five cycles of aneursym-susceptible flow. The dotted line indicates 2.2 Pa, the theoretical maximum for this waveform.

Chapter 3

RESULTS

3.1 PPFC Design and Fabrication

This chapter will focus on the physical flow chamber that was made and some of the design process that was involved as well as PIV to verify a portion of the flow field.

One of the requirements of the design is that cells seeded on glass slides are mountable to the flow chamber. Upon examination, it was realized that the glass slides were not exactly 75x25x1 mm as advertised but were 3"x1"x1.1 mm. This is a very slight difference but it will have an adverse effect in this case, as the glass slides won't fit into the groove that was precisely cut for the size of these slides. Thus more exact dimensions of the glass slides must be used. The glass slides must fit into the grooves without too much extra space to avoid perturbing the flow with a gap. A small nylon countersunk screw is placed such that the circular head of the screw just barely covers a small portion of the glass slide to secure it in place. It is not anticipated that this

will have an adverse effect on the flow field or the cells, as it does not significantly protrude into the flow field and is only about 0.17 inches in diameter.

The inlets were placed on the lengthwise sides of the chamber as opposed to the width-wise sides. Although putting the inlet and outlet on the lengthwise sides does add more length than putting them on the width-wise sides, the fluid flow is more unidirectional when they are on the lengthwise sides as opposed to the width-wise sides, which is desirable for optimal performance.

After manufacturing of the first device, there was an incomplete seal due to the lack of pressure around the O-ring at the inlet and outlet. There were screws along the lengthwise dimension, but none on the far sides of the device length-wise. This caused the polycarbonate to slightly bend in the middle of the device width-wise at the inlet and outlet, as seen in Figure 3.1. Because of this, a new PPFC was made with two additional screws on each side of the device on the inlet and outlet sides. This caused the overall length of the device to increase to 7 inches to accommodate the additional screws. Doing this did not affect the fluid flow area, only the outer portion that serves as a rigid support that defines the fluid height of the domain. This version is longer but still fits in the incubator.

The resulting PPFC device assembly is shown in Figure 3.2, and there was no leakage detectable. This was done with hand-applied pressure with a syringe, which is most likely far more than the device will be applying with the peristaltic/syringe pump. There were also two glass slides, one in each glass slide groove, to test whether or not the slides will be stationary throughout an experiment. The device was turned

over multiple times to test the robustness of the glass slide placement. There was no movement detected. Also, it can be seen in Figure 3.3 that the bowing effect that was previously seen was no longer present due to the additional two screws on each side.

A chamfer of 0.07 inches was implemented into the inlet and outlet facing the middle of the chamber so that the flow will reach the middle of the chamber sooner (width-wise, not length-wise). This will result in a more consistent WSS in the middle area closer to the inlet and outlet. This way, the flow will be uniform over more of the length of the chamber. The chamfers are shown in Figure 3.4.

Also shown in Figure 3.4 are stainless steel threaded inserts that were put in so that there was no need for protruding wing nuts. This allows for the countersunk screws to be below the PPFC face on both sides, making the chamber more low profile. Figure 3.5 shows an image of assembled the PPFC in an incubator.

(a) Shows the slight bowing of the PPFC due to the lack of screws on the outer portion of the O-ring on the outside toward the inlet.

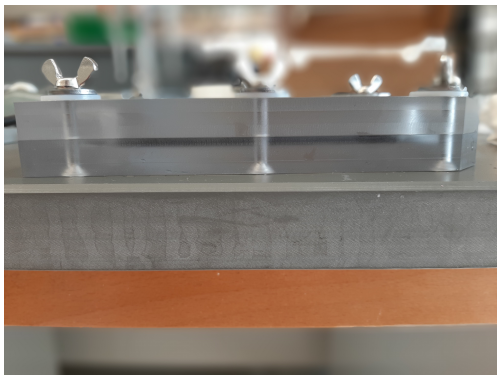

(b) Shows the side of the chamber where the O-ring is sealed properly, shown for comparison.

Figure 3.1: Warping of inlet and outlet side of O-ring.

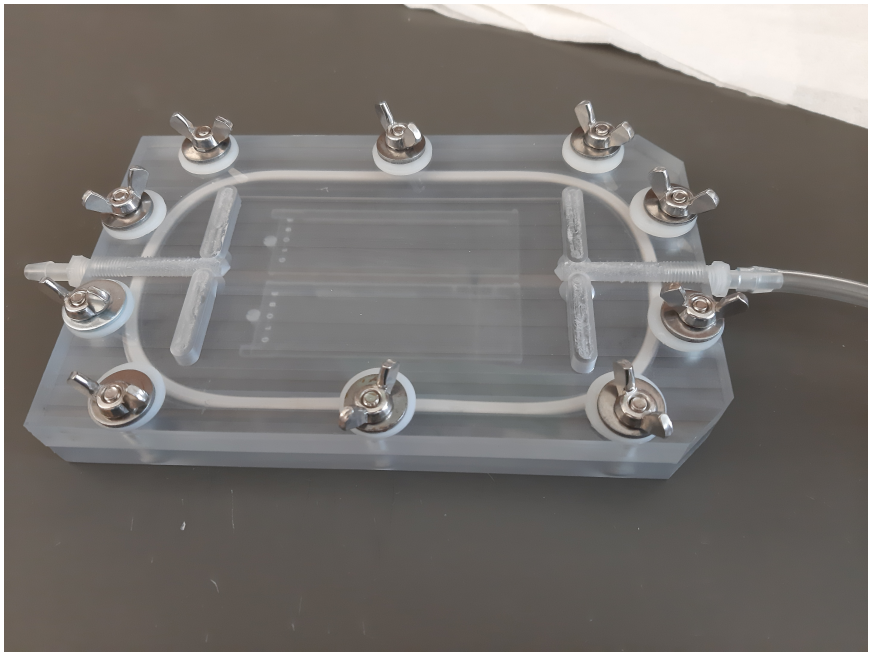

Figure 3.2: Test assembly, no leakage visible when one side is plugged and the other pressurized.

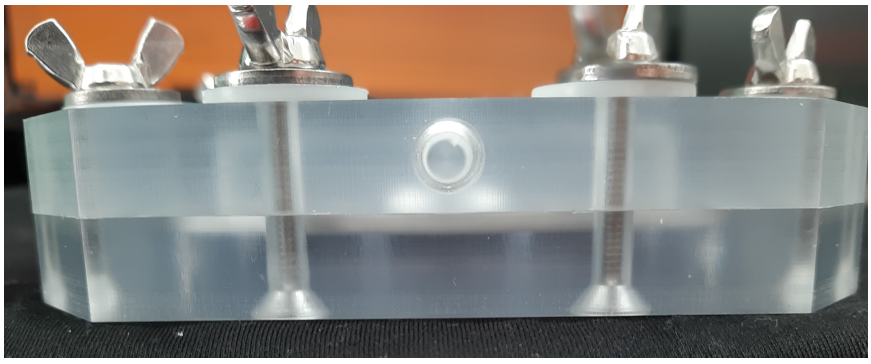

Figure 3.3: Test assembly, no gap or bowing visible.

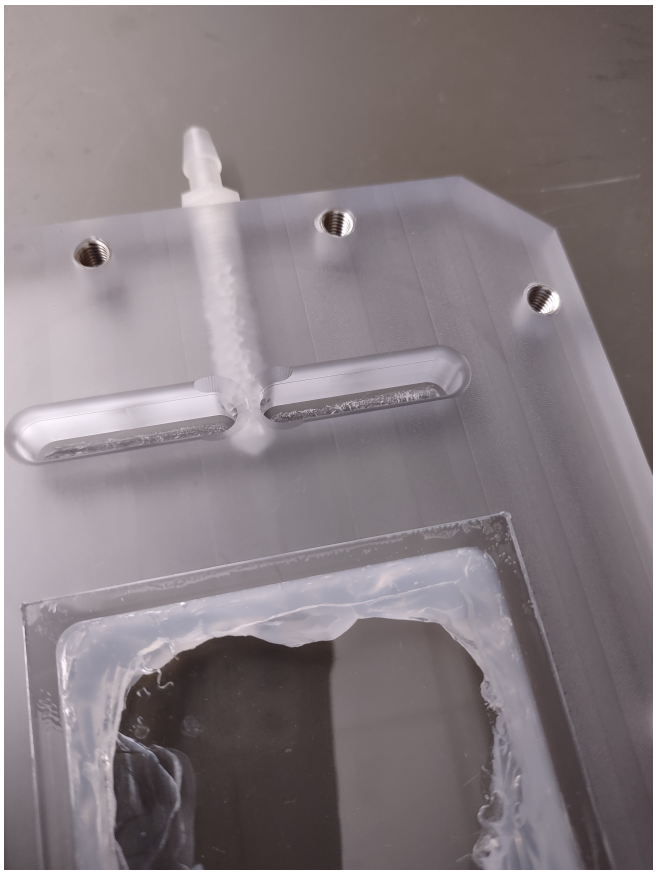

Figure 3.4: Shows the chamfered areas in the center of the inlet/outlet flow diverter region. This allows for the flow to more smoothly enter the chamber, decreasing the entrance length. Also shown are stainless steel threaded inserts which replace the wing nuts for a lower profile PPFC.

Figure 3.5: Designed PPFC in an incubator with fluid flowing through.

3.2 PIV Testing

PIV is conducted to verify the predictability of the flow rate inside the flow chamber. A syringe pump drives steady flow into the device, and a high-speed camera is used to image the particles. Silver-coated glass particles were used. The location of this point with respect to the PPFC geometry is shown in Figure 3.6.

Given a 3 mL/min constant flow rate driven by a syringe pump, the average velocity measured with PIV was 0.0012 m/s. Based on the equation $Q = AV$, which yielded a theoretical average velocity of 0.0011 m/s, there is a 7.5% error. It is desirable to determine whether there are large errors temporally, axially, or width-wise for the PIV measurements. First, to determine the transient error at each measurement point, a time-averaged vector field was created and is shown in Figure 3.9. The average transient standard deviation between all 210 measurement points was 4.6e-5 m/s. There is certainly an expected error in PIV over time, as there will be changes in seeding density throughout different images in the imaging interrogation area. That is a reason why having many images (100 for this study) to obtain an average is desirable.

Then, the data are averaged axially with a corresponding standard deviation to determine if there are differences spatially along the flow direction (axially). The average standard deviation for each was 2.9e-6 m/s, which is negligible. Lastly, to assess whether the flow profile changes across the flow, the average and standard deviation were calculated for the single column of averaged data, yielding an average of 0.0012 m/s with a standard deviation of 1.0e-6 m/s. This data is shown in Figure 3.10.

These data show that the flow field appears to be acting as expected, with a slightly higher average velocity measurement than expected by about 7.5%. Also, the RMS error is about 3e-5 m/s, which is only 1.6% of the final averaged velocity, which is not significant. Therefore, it can be assumed that there are no substantial sources of error from either transient or spatial dimensions. The 3 mL/min flow rate case had the highest percent difference between the PIV and theoretical average velocity among the 5 and 7 mL/min cases, which had 3.6 and 4.2% differences respectively.

The setup for the PPFC in an incubator driven by a peristaltic pump is shown in Figure 3.11. Under the white incubator, there is an electromagnetic vibration stage that drives the vibrations of the PPFC. The electromagnet has a stack of magnets glued to a long plastic 3D-printed shaft with a base that the PPFC sits on. The base that the PPFC sits on can be seen through the chamber in Figure 3.12 and the electromagnetic coil can be seen in Figure 3.13. In preliminary experiments using the peristaltic pump, cell survivability was verified and the flow chamber was able to induce both flow and vibrations onto ECs.

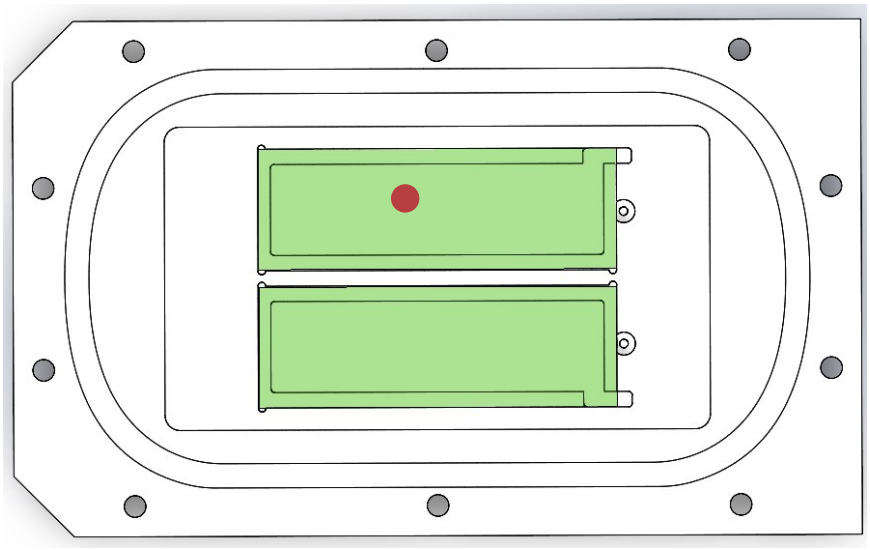

Figure 3.6: Location of PIV imaging is the red dot, at coordinates (52,15) mm, where the origin is at the center of the inlet side of the fluid domain.

Figure 3.7: PIV setup, PPFC is taped down to avoid motion during imaging. The red device on the bottom left of the image is the syringe pump.

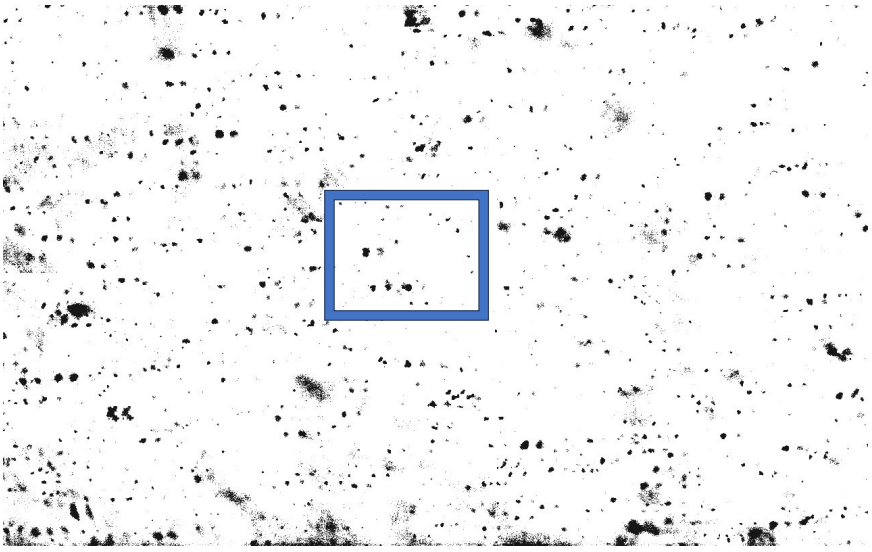

Figure 3.8: Example of one image in a set. A magnetic-base mixing station is frequently turned on throughout testing to mix particles with fluid to keep the seeding density more even throughout the tests.

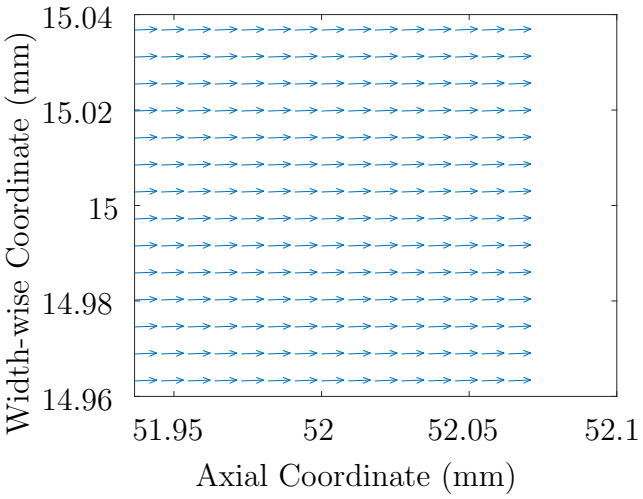

Figure 3.9: Time averaged vector field from all 100 images taken. There is little variation in any vector lengths of velocity.

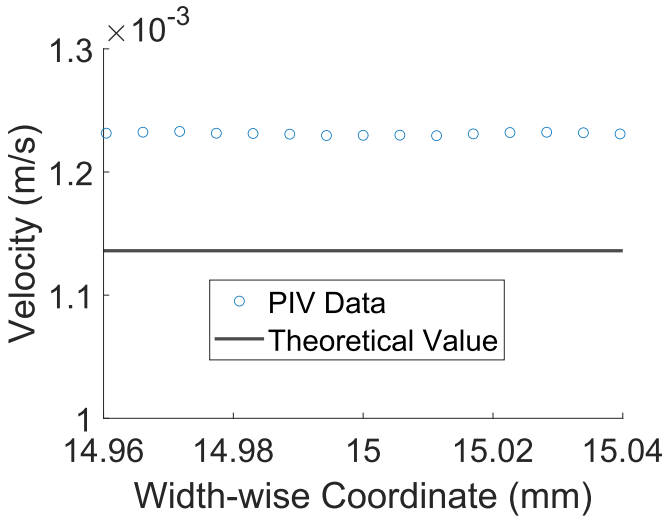

Figure 3.10: Time and axially averaged data. Although there is a difference in velocity magnitude between PIV data and the theoretical solution from $Q = AV$, it can still be seen that there is a consistent flow field across the flow field.

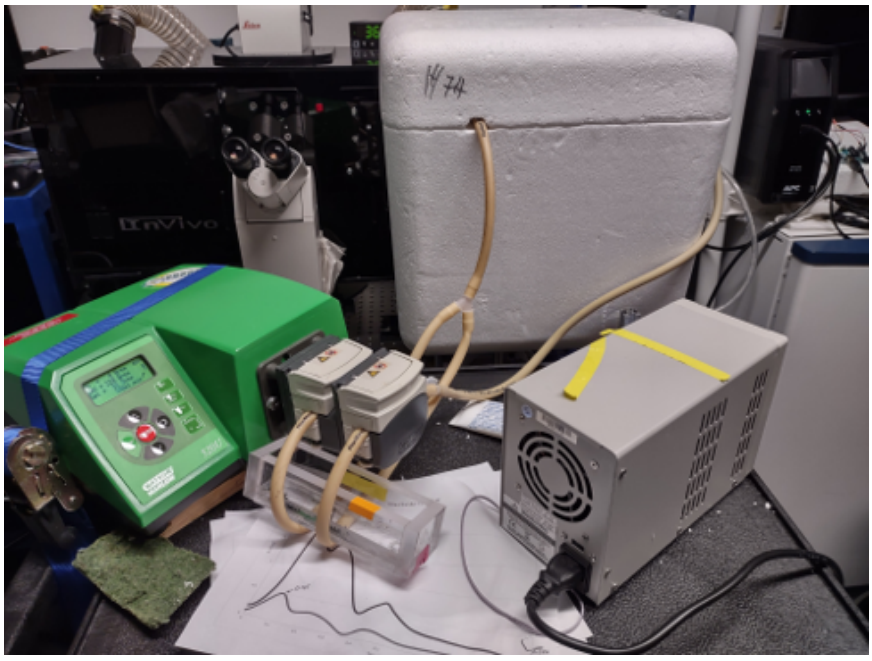

Figure 3.11: PPFC in an incubator driven by a peristaltic pump.

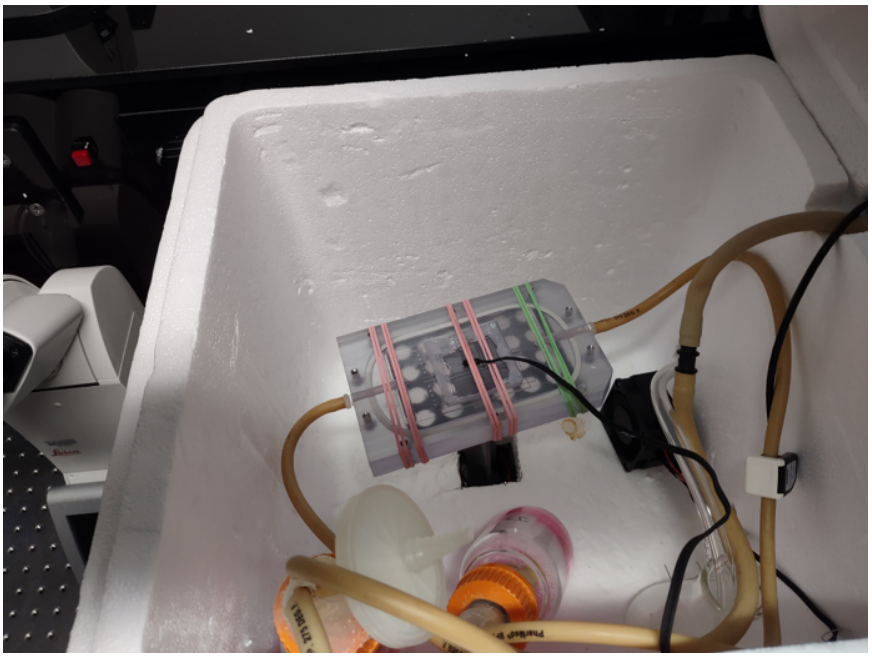

Figure 3.12: PPFC in an incubator secured to the vibration stage base.

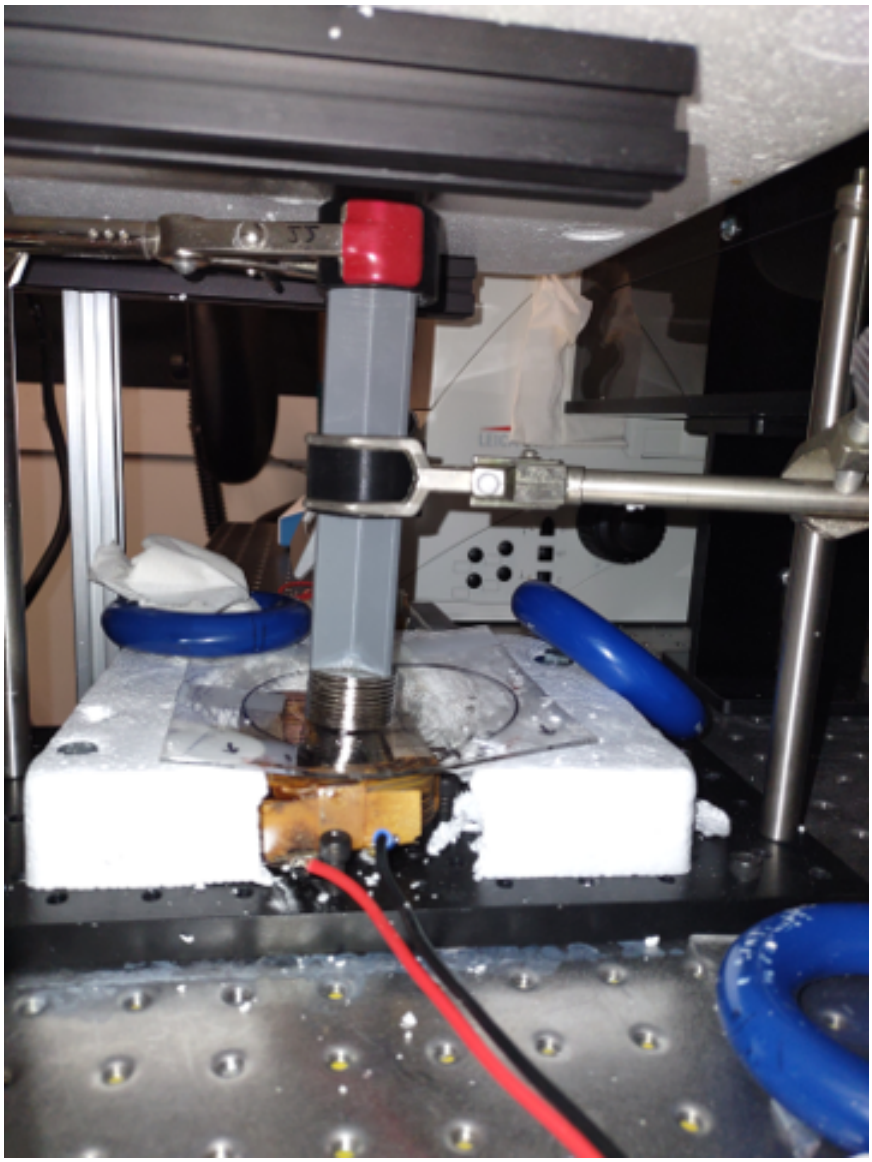

Figure 3.13: Shows the electromagnet that drives the vibrations of the PPFC. The round magnets are placed just above the top plane of the electromagnetic coil (orange at the bottom). The long vibration shaft (gray) goes through the incubator and up to the PPFC. The electromagnetic coil must be far from the ECs due to the effect of the electromagnet on the gene expression of ECs (data not shown).

Chapter 4

CONCLUSION AND FUTURE WORK

This work has demonstrated the design and use of a flow chamber to induce WSS waveforms onto ECs that mimic in vivo fluid flow conditions in vitro. The CPV was not suitable for this application as ECs in that setup could not be realistically vibrated without undesirable secondary flows. A PPFC was analyzed numerically and computationally to verify the design. The flow field tested was laminar Poiseuille flow and the cells are far from walls to avoid any high velocity gradients. A portion of the flow field was verified using PIV.

A limitation of this work is the rigid PPFC base. An artery is compliant, thus any pressure fluctuations caused by unsteady flow would vibrate the artery. In the current design, the vibrations of the flwo chamber account for this, but it would be more representative of the in vivo condition if the ECs were seeded in a cylindrical

compliant membrane, such as silicone or PDMS. This way, the pulsatile flow and the geometry of the device would induce more relevant vibrations caused by the flow. A PPFC was used due to its simple and well-defined geometry and flow field.

Another limitation of this work is using a Newtonian fluid, EGM-2. While this allows many convenient assumptions practically and mathematically, blood is a non-Newtonian fluid. Therefore this work should be expanded to incorporate the effects of non-Newtonian fluid mechanics to better mimic what occurs in vivo.

A topic that should be studied more extensively is the effect of secondary flows on a cone and plate where there is a defined gap height between the cone apex and the bottom plate. This would give a more accurate model for a typical CPV used in this context.

Rather than putting a flw chamber in an incubator for thermal control, Kriesi et al. developed a heating system within a flow chamber that does not require tools to assemble or exchange the cell area.[68] This is advantageous because using an incubator forces the entire flow chamber along with the rest of the assembly to fit and be hosted in the incubator during an experiment. Kriesi's solution was an innovative method where an incubator was replaced with a feedback-controlled heater. The fact that there is little interaction required, hence ease of use, makes it more advantageous. Also, the ease of observing the cells over the course of an experiment is a large benefit of Kriesi's device due to its small size. The trouble in implementing some of these features, such as continuous observability under a microscope, is the fact that the current device must be vibrated, and this would be very challenging to keep in focus

under a microscope.

Hence, for the current model, there still remains a need to have a live cell observation method that does not require removal from the apparatus. Although Kriesi et al. did not demonstrate pulsatile flow, they still defined a comprehensive design model that was well implemented, and their heating, assembly design, and live observation methods are worth taking note of and should be implemented into a future model of this work.

In terms of observation, the polycarbonate was not as favorable as predicted due to the lower tolerance in the stock material. Since the material had to be machined to be squared off, there was a foggy appearance on the surface from the machine marks. Therefore, the cells were not able to be clearly observed as intended. Overall, having a cutout for a glass window for observation is preferable so that the focal lens of the microscope used for PIV can be closer to the particles observed. Also, polycarbonate is very scratchable and soft, so the lifetime of the material is questionable when compared to a more robust yet more expensive material like PEEK. Although it is expensive, it is a great material candidate for this application. Also, since the driving reason for using polycarbonate was the benefit of transparency, and in the end, a window groove was cut out, there is no longer a beneficial reason to use polycarbonate over a material like PEEK or aluminum. Overall polycarbonate is a passable option but may not be ideal.

Nowicki et al. implemented a more physiologically relevant geometry for an aneurysm application to a pseudo-PPFC. This idea may be beneficial to understand how var-

ious geometries effect EC response. A useful expansion of their work would be to implement pulsatile flow in their device.[85] The geometry was slightly different, thus diverging from the theoretical solution for a typical PPFC, but the concept of implementing concepts of a PPFC to a relevant pro-aneurysmal geometry is appealing.

Another fascinating finding that should be expanded on more is the work of Salman et al., where an acoustic pressure sensor was designed to sense the acoustic vibrations, tracking them by frequency, and using this data to interpret stenosis status in patients.[97] Something like this would enable the tracking of vibration amplitude and frequency of vibrations for ECs, which could provide patient-specific data for vibration amplitudes and frequencies.

A fascinating expansion of this work would include obtaining patient-specific data on aneurysm development and how various circle of Willis configurations may be more or less aneurysm-susceptible based on the differences in hemodynamics of such varieties. Vrselja and Kapoor concluded the primary function of the COW was to dissipate pressure rather than distribute blood to/from various parts of the COW. Based on this, Kapoor noted the critical function of these arteries to prevent extreme hemodynamic stresses. There may be much value in understanding the impact of hemodynamics on aneurysm development based on specific configurations of the circle of Willis.

Bibliography

[1] *Wall Shear Stress Fluctuations due to Flow Instability in Intracranial Aneurysms* (06 2010), vol. ASME 2010 Summer Bioengineering Conference, Parts A and B of *Summer Bioengineering Conference*.

[2] Adams, J. A., Mangino, M. J., Bassuk, J., Kurlansky, P., and Sackner, M. A. Regional blood flow during periodic acceleration. *Critical Care Medicine 29* (2001).

[3] Ailawadi, G., Moehle, C., Pei, H., Walton, S., Yang, Z., Kron, I., Lau, C., and Owens, G. Smooth muscle phenotypic modulation is an early event in aortic aneurysms. *The Journal of thoracic and cardiovascular surgery 138* (12 2009), 1392–9.

[4] Alfano, J., Kolega, J., Natarajan, S., Xiang, J., Paluch, R., Levy, E., Siddiqui, A., and Meng, H. Intracranial aneurysms occur more frequently at bifurcation sites that typically experience higher hemodynamic stresses. *Neurosurgery 73* (06 2013).

[5] ALPERS, B. J., BERRY, R. G., and PADDISON, R. M. Anatomical Studies of the Circle of Willis in Normal Brain. *A.M.A. Archives of Neurology Psychiatry 81*, 4 (04 1959), 409–418.

[6] Anwar, M., Shalhoub, J., Lim, C., Gohel, M., and Davies, A. The effect of pressure-induced mechanical stretch on vascular wall differential gene expression. *Journal of vascular research 49* (07 2012), 463–78.

[7] Arneklo-Nobin, B., Johansen, K., and Sjöberg, T. The objective diagnosis of vibration-induced vascular injury. *Scandinavian Journal of Work, Environment Health 13*, 4 (1987), 337–342.

[8] Awolesi, M. A., Sessa, W. C., and Sumpio, B. E. Cyclic strain upregulates nitric oxide synthase in cultured bovine aortic endothelial cells. *The Journal of Clinical Investigation 96*, 3 (9 1995), 1449–1454.

[9] Azuma, N., Duzgun, S., Ikeda, M., Kito, H., Akasaka, N., Sasajima, T., and Sumpio, B. E. Endothelial cell response to different mechanical forces. *Journal of Vascular Surgery 32*, 4 (2000), 789–794.

[10] Bacabac, R. G., Smit, T. H., Van Loon, J. J. W. A., Doulabi, B. Z., Helder, M., and Klein-Nulend, J. Bone cell responses to high-frequency vibration stress: does the nucleus oscillate within the cytoplasm? *The FASEB Journal 20*, 7 (2006), 858–864.

[11] Backes, D., Rinkel, G. J., Greving, J. P., Velthuis, B. K., Murayama, Y., Takao, H., Ishibashi, T., Igase, M., terBrugge, K. G., Agid, R., Jääskeläinen, J. E., Lindgren, A. E., Koivisto, T., von und zu Fraunberg, M., Matsubara, S., Moroi, J., Wong, G. K., Abrigo, J. M., Igase, K., Matsumoto, K., Wermer, M. J., van Walderveen, M. A., Algra, A., and Vergouwen, M. D. Elapss score for prediction of risk of growth of unruptured intracranial aneurysms. *Neurology 88*, 17 (2017), 1600–1606.

[12] Bataineh, K. M. Numerical investigation of secondary flow effect in cone–plate viscometer. *Computers and Fluids 101* (2014), 105–113.

[13] Bayliss, W. M. On the local reactions of the arterial wall to changes of internal pressure. *The Journal of Physiology 28*, 3 (1902), 220–231.

[14] Bearman, P., and Branković, M. Experimental studies of passive control of vortex-induced vibration. *European Journal of Mechanics - B/Fluids 23*, 1 (2004), 9–15. Bluff Body Wakes and Vortex-Induced Vibrations.

[15] Bochud, M., Bovet, P., Elston, R. C., Paccaud, F., Falconnet, C., Maillard, M., Shamlaye, C., and Burnier, M. High heritability of ambulatory blood pressure in families of east african descent. *Hypertension 45*, 3 (2005), 445–450.

[16] Bodin, P., and Burnstock, G. Increased release of atp from endothelial cells during acute inflammation. *Inflammation Research 47* (1998), 351–354.

[17] Boughner, D. R., and Roach, M. R. Effect of low frequency vibration on the arterial wall. *Circulation Research 29*, 2 (1971), 136–144.

[18] Brian, J. E., Heistad, D. D., and Faraci, F. M. Effect of carbon monoxide on rabbit cerebral arteries. *Stroke 25*, 3 (1994), 639–643.

[19] Brisman, J. L., Song, J. K., and Newell, D. W. Cerebral aneurysms. *New England Journal of Medicine 355*, 9 (2006), 928–939. PMID: 16943405.

[20] Bull, M. Wall-pressure fluctuations beneath turbulent boundary layers: Some reflections on forty years of research. *Journal of Sound and Vibration 190*, 3 (1996), 299–315.

[21] Canham, P. B., and Finlay, H. M. Morphometry of medial gaps of human brain artery branches. *Stroke 35*, 5 (2004), 1153–1157.

[22] Chalouhi, N., Chitale, R., Jabbour, P., Tjoumakaris, S., Dumont, A. S., Rosenwasser, R., and Gonzalez, L. F. The case for family screening for intracranial aneurysms. *Neurosurgical Focus FOC 31*, 6 (2011), E8.

[23] Chalouhi, N., Hoh, B. L., and Hasan, D. Review of cerebral aneurysm formation, growth, and rupture. *Stroke 44*, 12 (2013), 3613–3622.

[24] Chang, P. K. *Separation of flow*. Elsevier, 2014.

[25] Chatzizisis, Y. S., Coskun, A. U., Jonas, M., Edelman, E. R., Feldman, C. L., and Stone, P. H. Role of endothelial shear stress in the natural history of coronary atherosclerosis and vascular remodeling: Molecular, cellular, and vascular behavior. *Journal of the American College of Cardiology 49*, 25 (2007), 2379–2393.

[26] Chien, A., Castro, M., Tateshima, S., Sayre, J., Cebral, J., and Viñuela, F. Quantitative hemodynamic analysis of brain aneurysms at different locations. *American Journal of Neuroradiology 30*, 8 (2009), 1507–1512.

[27] Chiu, J.-J., Chen, L.-J., Chen, C.-N., Lee, P.-L., and Lee, C.-I. A model for studying the effect of shear stress on interactions between vascular endothelial cells and smooth muscle cells. *Journal of Biomechanics 37*, 4 (2004), 531–539.

[28] Cho, J.-G., Witting, P. K., Verma, M., Wu, B. J., Shanu, A., Kairaitis, K., Amis, T. C., and Wheatley, J. R. Tissue Vibration Induces Carotid Artery Endothelial Dysfunction: A Mechanism Linking Snoring and Carotid Atherosclerosis? *Sleep 34*, 6 (06 2011), 751–757.

[29] Curry, B. D., Bain, J. L., Yan, J.-G., Zhang, L. L., Yamaguchi, M., Matloub, H. S., and Riley, D. A. Vibration injury damages arterial endothelial cells. *Muscle & Nerve 25*, 4 (2002), 527–534.

[30] Dai, G., Kaazempur-Mofrad, M. R., Kamm, R. D., Zhang, Y., Vaughn, S., Garcia-Cardena, G., and Gimbrone, M. A. Distinct endothelial phenotypes evoked by arterial waveforms derived from atherosclerosis-prone and atherosclerosis-protected regions of the human vasculature. *Cardiovascular Pathology 13*, 3, Supplement (2004), 26. Abstract issue 13/3S.

[31] Dimmeler, S., Fleming, I., Fisslthaler, B., Hermann, C., Busse, R., and Zeiher, A. M. Activation of nitric oxide synthase in endothelial cells by akt-dependent phosphorylation. *Nature 399* (1999), 601–605.

[32] Dobrin, P. B. Mechanics of normal and diseased blood vessels. *Annals of Vascular Surgery 2*, 3 (1988), 283–294.

[33] Dobrin, P. B. Elastin, collagen, and the pathophysiology of arterial aneurysms. *Development of Aneurysms* (2000), 42–73.

[34] Dolan, J. M., Meng, H., Sim, F. J., and Kolega, J. Differential gene expression by endothelial cells under positive and negative streamwise gradients of high wall shear stress. *American Journal of Physiology-Cell Physiology 305*, 8 (2013), C854–C866. PMID: 23885059.

[35] ETHIER, C. R., PRAKASH, S., STEINMAN, D. A., LEASK, R. L., COUCH, G. G., and OJHA, M. Steady flow separation patterns in a 45 degree junction. *Journal of Fluid Mechanics 411* (2000), 1–38.

[36] Franzoni, M., Cattaneo, I., Ene-Iordache, B., Oldani, A., Righettini, P., and Remuzzi, A. Design of a cone-and-plate device for controlled realistic shear stress stimulation on endothelial cell monolayers. *Cytotechnology 68* (2016), 1885–1896.

[37] Franzoni, M., Cattaneo, I., Longaretti, L., Figliuzzi, M., Ene-Iordache, B., and Remuzzi, A. Endothelial cell activation by hemodynamic shear stress derived from arteriovenous fistula for hemodialysis access. *American Journal of Physiology-Heart and Circulatory Physiology 310*, 1 (2016), H49–H59. PMID: 26497959.

[38] Fulton, D., Gratton, J.-P., McCabe, T. J., Fontana, J., Fujio, Y., Walsh, K., Franke, T. F., Papapetropoulos, A., , and Sessa, W. C. Regulation of endothelium-derived nitric oxide production by the protein kinase akt. *Nature 399* (1999), 597–601.

[39] Garin, G., and Berk, B. C. Flow-mediated signaling modulates endothelial cell phenotype. *Endothelium 13*, 6 (2006), 375–384. PMID: 17169770.

[40] Goenka, S. Influence of higher frequency components and duration of mechanical vibration on artery and bone in a rat-tail model.

[41] Goldstein, S. *Modern Developments in Fluid Dynamics*, vol. 1. Clarendon Press, 1938.

[42] GORMAN, D., REESE, J., and ZHANG, Y. Vibration of a flexible pipe conveying viscous pulsating fluid flow. *Journal of Sound and Vibration 230*, 2 (2000), 379–392.

[43] Greving, J. P., Rinkel, G. J., Buskens, E., and Algra, A. Cost-effectiveness of preventive treatment of intracranial aneurysms. *Neurology 73*, 4 (2009), 258–265.

[44] Hahn, C., and Schwartz, M. A. Mechanotransduction in vascular physiology and atherogenesis. *Nature Reviews Molecular Cell Biology 10* (2009), 53–62.

[45] Hardesty, W. H., Roberts, B., Toole, J. F., and Royster, H. P. Studies on carotid artery flow. *Surgery 49*, 2 (1961), 251–256.

[46] HAVLIK, R. J., GARRISON, R. J., FEINLEIB, M., KANNEL, W. B., CASTELLI, W. P., and MCNAMARA, P. M. BLOOD PRESSURE AGGREGATION IN FAMILIES. *American Journal of Epidemiology 110*, 3 (09 1979), 304–312.

[47] Hele-Shaw, H. The flow of water. *Nature 58* (1898), 34–36.

[48] Hottenga, J.-J., Boomsma, D. I., Kupper, N., Posthuma, D., Snieder, H., Willemsen, G., and de Geus, E. J. C. Heritability and stability of resting blood pressure. *Twin Research and Human Genetics 8*, 5 (2005), 499–508.

[49] Howe, M. S. Surface pressures and sound produced by turbulent flow over smooth and rough walls. *The Journal of the Acoustical Society of America 90*, 2 (1991), 1041–1047.

[50] Howitt, L., Kairaitis, K., Kirkness, J. P., Garlick, S. R., Wheatley, J. R., Byth, K., and Amis, T. C. Oscillatory pressure wave transmission from the upper airway to the carotid artery. *Journal of Applied Physiology 103*, 5 (2007), 1622–1627. PMID: 17702839.

[51] Huang, J., McGirt, M. J., Gailloud, P., and Tamargo, R. J. Intracranial aneurysms in the pediatric population: case series and literature review. *Surgical Neurology 63*, 5 (2005), 424–432.

[52] Ikeda, M., Takei, T., Mills, I., Kito, H., and Sumpio, B. E. Extracellular signal-regulated kinases 1 and 2 activation in endothelial cells exposed to cyclic strain. *American Journal of Physiology-Heart and Circulatory Physiology 276*, 2 (1999), H614–H622. PMID: 29598616.

[53] Ingebrigtsen, T., Morgan, M. K., Faulder, K., Ingebrigtsen, L., Sparr, T., and Schirmer, H. Bifurcation geometry and the presence of cerebral artery aneurysms. *Journal of Neurosurgery 101*, 1 (2004), 108 – 113.

[54] Jaffe, E. A. Cell biology of endothelial cells. *Human Pathology 18*, 3 (1987), 234–239.

[55] Jalali, S., del Pozo, M. A., Chen, K.-D., Miao, H., Li, Y.-S., Schwartz, M. A., Shyy, J. Y.-J., and Chien, S. Integrin-mediated mechanotransduction requires its dynamic interaction with specific extracellular matrix (ecm) ligands. *Proceedings of the National Academy of Sciences 98*, 3 (2001), 1042–1046.

[56] Johanning, J. M., Armstrong, P. J., Franklin, D. P., Han, D. C., Carey, D. J., and Elmore, J. R. Nitric oxide in experimental aneurysm formation: Early events and consequences of nitric oxide inhibition. *Annals of Vascular Surgery 16*, 1 (2002), 65–72.

[57] Jong, de, C. *Analysis of pulsations and vibrations in fluid-filled pipe systems.* PhD thesis, Mechanical Engineering, 1994.

[58] Kanematsu, Y., Kanematsu, M., Kurihara, C., Tada, Y., Tsou, T.-L., van Rooijen, N., Lawton, M. T., Young, W. L., Liang, E. I., Nuki, Y., and Hashimoto, T. Critical roles of macrophages in the formation of intracranial aneurysm. *Stroke 42*, 1 (2011), 173–178.

[59] Kapoor, K., Singh, B., and Dewan, L. Variations in the configuration of the circle of willis. *Anatomical science international 83* (07 2008), 96–106.

[60] Karceski, S. Predicting growth of brain aneurysmsabout aneurysms. *Neurology 88*, 17 (2017), e179–e181.

[61] Katusic, Z. S., Marshall, J. J., Kontos, H. A., and Vanhoutte, P. M. Similar responsiveness of smooth muscle of the canine basilar artery to edrf and

nitric oxide. *American Journal of Physiology-Heart and Circulatory Physiology 257*, 4 (1989), H1235–H1239. PMID: 2552840.

[62] Kennedy, Khan, McLaren, and Belch. Endothelial activation and response in patients with hand arm vibration syndrome. *European Journal of Clinical Investigation 29*, 7 (1999), 577–581.

[63] Kerber, C. W., Hecht, S. T., Knox, K., Buxton, R. B., and Meltzer, H. S. Flow dynamics in a fatal aneurysm of the basilar artery. *American Journal of Neuroradiology 17*, 8 (1996), 1417–1421.

[64] Kerber, C. W., and Heilman, C. B. Application of full field optical studies for pulsatile flow in a carotid artery phantom. *American Journal of Neuroradiology 13*, 1 (Jan-Feb 1992), 173–180.

[65] Kito, H., Chen, E. L., Wang, X., Ikeda, M., Azuma, N., Nakajima, N., Gahtan, V., and Sumpio, B. E. Role of mitogen-activated protein kinases in pulmonary endothelial cells exposed to cyclic strain. *Journal of Applied Physiology 89*, 6 (2000), 2391–2400. PMID: 11090594.

[66] Krajnak, K., Dong, R. G., Flavahan, S., Welcome, D., and Flavahan, N. A. Acute vibration increases α2c-adrenergic smooth muscle constriction and alters thermosensitivity of cutaneous arteries. *Journal of Applied Physiology 100*, 4 (2006), 1230–1237. PMID: 16339346.

[67] Krejza, J., Arkuszewski, M., Kasner, S. E., Weigele, J., Ustymowicz, A., Hurst, R. W., Cucchiara, B. L., and Messe, S. R. Carotid artery diameter in men and women and the relation to body and neck size. *Stroke 37*, 4 (2006), 1103–1105.

[68] Kriesi, C., Steinert, M., Marmaras, A., Danzer, C., Meskenaite, V., and Kurtcuoglu, V. Integrated flow chamber system for live cell microscopy. *Frontiers in Bioengineering and Biotechnology 7* (2019).

[69] Ku, D. N., Giddens, D. P., Zarins, C. K., and Glagov, S. Pulsatile flow and atherosclerosis in the human carotid bifurcation. positive correlation between plaque location and low oscillating shear stress. *Arteriosclerosis: An Official Journal of the American Heart Association, Inc. 5*, 3 (1985), 293–302.

[70] Lane, W., Jantzen, A., Carlon, T., Jamiolkowski, R., Grenet, J., Ley, M., Haseltine, J., Galinat, L., Lin, F.-H., Allen, J., Truskey, G., and Achneck, H. Parallel-plate flow chamber and continuous flow circuit to evaluate endothelial progenitor cells under laminar flow shear stress. *Journal of visualized experiments : JoVE* (01 2012).

[71] Lee, M., Park, G., Park, C., and Kim, C. Improvement of grid independence test for computational fluid dynamics model of building based on grid resolution. *Advances in Civil Engineering 2020* (12 2020).

[72] Lee, S. A., Amis, T. C., Byth, K., Larcos, G., Kairaitis, K., and Robinson, Tracey D Wheatley, J. R. Heavy snoring as a cause of carotid artery atherosclerosis. *Sleep 31*, 9 (2008), 1207–1213.

[73] Leeder, M., and Bridges, P. Flow separation in meander bends. *Nature 253* (1975), 338–339.

[74] Liepsch, D. Flow in tubes and arteries–a comparison. *Biorheology 23 4* (1986), 395–433.

[75] Liu, Q., Jiang, P., Jiang, Y., Li, S., Ge, H., Jin, H., and Li, Y. Bifurcation configuration is an independent risk factor for aneurysm rupture irrespective of location. *Frontiers in Neurology 10* (2019).

[76] M, F. *Part 1: Multiple Functions of the Endothelial Cells—Focus on Endothelium-Derived Vasoactive Mediators*. Morgan and Claypool Life Sciences, San Rafael (CA), 2011.

[77] Man, H. J., Sukumar, A. N., Ku, K. H., Dubinsky, M. K., Subramaniam, N., and Marsden, P. A. Gene expression analysis of endothelial cells exposed to shear stress using multiple parallel-plate flow chambers. *Journal of Visualized Experiments 77*, 13 (2018).

[78] McCurley, A., Pires, P. W., Bender, S. B., Aronovitz, M., Zhao, M. J., Metzger, D., Chambon, P., Hill, M. A., Dorrance, A. M., Mendelsohn, M. E., and Jaffe, I. Z. Direct regulation of blood pressure by smooth muscle cell mineralocorticoid receptors. *Nature Medicine 18* (09 2012), 1429–1433.

[79] Meng, H., Wang, Z., Hoi, Y., Gao, L., Metaxa, E., Swartz, D. D., and Kolega, J. Complex hemodynamics at the apex of an arterial bifurcation induces vascular remodeling resembling cerebral aneurysm initiation. *Stroke 38*, 6 (2007), 1924–1931.

[80] Mithieux, S. M., and Weiss, A. S. Elastin. In *Fibrous Proteins: Coiled-Coils, Collagen and Elastomers*, vol. 70 of *Advances in Protein Chemistry*. Academic Press, 2005, pp. 437–461.

[81] Murata, M., and Kawanishi, S. Oxidative dna damage induced by nitrotyrosine, a biomarker of inflammation. *Biochemical and Biophysical Research Communications 316*, 1 (2004), 123–128.

[82] Naggara, O. N., White, P. M., Guilbert, F., Roy, D., Weill, A., and Raymond, J. Endovascular treatment of intracranial unruptured aneurysms: Systematic review and meta-analysis of the literature on safety and efficacy. *Radiology 256*, 3 (2010), 887–897. PMID: 20634431.

[83] Nemati, M., Loozen, G. B., van der Wekken, N., van de Belt, G., Urbach, H. P., Bhattacharya, N., and Kenjeres, S. Application of full

field optical studies for pulsatile flow in a carotid artery phantom. *Biomed. Opt. Express 6*, 10 (Oct 2015), 4037–4050.

[84] Nidadavolu, S. S. *Analysis and Comparison of Parallel Plate Flow Chambers to Determine Consistency of Fluid forces on Cells*. 2013.

[85] Nowicki, K. W., Hosaka, K., He, Y., McFetridge, P. S., Scott, E. W., and Hoh, B. L. Novel high-throughput in vitro model for identifying hemodynamic-induced inflammatory mediators of cerebral aneurysm formation. *Hypertension 64*, 6 (2014), 1306–1313.

[86] Oktar, S., Yücel, C., Karaosmanoglu, D., Akkan, K., Ozdemir, H., Tokgoz, N., and Tali, T. Blood-flow volume quantification in internal carotid and vertebral arteries: Comparison of 3 different ultrasound techniques with phase-contrast mr imaging. *American Journal of Neuroradiology 27*, 2 (2006), 363–369.

[87] Osol, G., Brekke, J. F., McElroy-Yaggy, K., and Gokina, N. I. Myogenic tone, reactivity, and forced dilatation: a three-phase model of in vitro arterial myogenic behavior. *American Journal of Physiology-Heart and Circulatory Physiology 283*, 6 (2002), H2260–H2267. PMID: 12388265.

[88] Palmer, R., Ashton, D., and Moncada, S. Vascular endothelial cells synthesize nitric oxide from l-arginine. *Nature 333* (1988), 664–666.

[89] Pearson, J. D. Endothelial cell function and thrombosis. *Best Practice and Research Clinical Haematology 12*, 3 (1999), 329–341.

[90] Predescu, D., Predescu, S., Shimizu, J., Miyawaki-Shimizu, K., and Malik, A. B. Constitutive enos-derived nitric oxide is a determinant of endothelial junctional integrity. *American Journal of Physiology-Lung Cellular and Molecular Physiology 289*, 3 (2005), L371–L381. PMID: 16093363.

[91] Quyyumi, A. A., Dakak, N., Andrews, N. P., Husain, S., Arora, S., Gilligan, D. M., Panza, J. A., and 3rd, R. O. C. Nitric oxide activity in the human coronary circulation. impact of risk factors for coronary atherosclerosis. *The Journal of Clinical Investigation 95*, 4 (4 1995), 1747–1755.

[92] Ramadan, E. *Modeling Oscillatory Flow in a Cone-and-Plate Device Using Computational Fluid Dynamics*. 2019.

[93] Rees, D. D., Palmer, R. M., and Moncada, S. Role of endothelium-derived nitric oxide in the regulation of blood pressure. *Proceedings of the National Academy of Sciences 86*, 9 (1989), 3375–3378.

[94] Roach, M. R., Scott, S., and Ferguson, G. G. The hemodynamic importance of the geometry of bifurcations in the circle of willis (glass model studies). *Stroke 3*, 3 (1972), 255–267.

[95] Ruigrok, Y. M., and Rinkel, G. J. Genetics of intracranial aneurysms. *Stroke 39*, 3 (2008), 1049–1055.

[96] Sacco, R. L., Wolf, P. A., Bharucha, N. E., Meeks, S. L., Kannel, W. B., Charette, L. J., McNamara, P. M., Palmer, E. P., and D'Agostino, R. Subarachnoid and intracerebral hemorrhage. *Neurology 34*, 7 (1984), 847–847.

[97] Salman, H., and Yazicioglu, Y. Experimental and numerical investigation on soft tissue dynamic response due to turbulence-induced arterial vibration. *Medical Biological Engineering Computing 57* (06 2019), 1–16.

[98] Schievink, W. I. Intracranial aneurysms. *New England Journal of Medicine 336*, 1 (1997), 28–40. PMID: 8970938.

[99] Schmidt, H. H., and Walter, U. No at work. *Cell 78*, 6 (1994), 919–925.

[100] Sdougos, H. P., Bussolari, S. R., and Dewey, C. F. Secondary flow and turbulence in a cone-and-plate device. *Journal of Fluid Mechanics 138* (1984), 379–404.

[101] Selimovic, A., Ventikos, Y., and Watton, P. N. Modelling the evolution of cerebral aneurysms: Biomechanics, mechanobiology and multiscale modelling. *Procedia IUTAM 10* (2014), 396–409. Mechanics for the World: Proceedings of the 23rd International Congress of Theoretical and Applied Mechanics, ICTAM2012.

[102] Sengupta, P. P., Pedrizzetti, G., Kilner, P. J., Kheradvar, A., Ebbers, T., Tonti, G., Fraser, A. G., and Narula, J. Emerging trends in cv flow visualization. *JACC: Cardiovascular Imaging 5*, 3 (2012), 305–316.

[103] Skoglund, C. R. Vasodilatation in human skin induced by low-amplitude high-frequency vibration. *Clinical Physiology 9*, 4 (1989), 361–372.

[104] Song, J. W., Gu, W., Futai, N., Warner, K. A., Nor, J. E., and Takayama, S. Computer-controlled microcirculatory support system for endothelial cell culture and shearing. *Analytical Chemistry 77*, 13 (2005), 3993–3999. PMID: 15987102.

[105] Stehbens, W. E. Turbulence of blood flow. *Quarterly Journal of Experimental Physiology and Cognate Medical Sciences 44*, 1 (1959), 110–117.

[106] Stehbens, W. E. Histopathology of Cerebral Aneurysms. *Archives of Neurology 8*, 3 (03 1963), 272–285.

[107] Stehbens, W. E. *The Pathology of Intracranial Arterial Aneurysms and Their Complications*. Springer US, New York, NY, 1983, pp. 272–357.

[108] Stoner, L., Young, J. M., Fryer, S., and Sabatier, M. J. The importance of velocity acceleration to flow-mediated dilation. *International Journal of Vascular Medicine 2012* (2012).

[109] Straatman, A. G., Khayat, R. E., Haj-Qasem, E., and Steinman, D. A. On the hydrodynamic stability of pulsatile flow in a plane channel. *Physics of Fluids 14*, 6 (2002), 1938–1944.

[110] Sucosky, P., Padala, M., Elhammali, A., Balachandran, K., Jo, H., and Yoganathan, A. P. Design of an Ex Vivo Culture System to Investigate the Effects of Shear Stress on Cardiovascular Tissue. *Journal of Biomechanical Engineering 130*, 3 (04 2008). 035001.

[111] Sundström, E., Jonnagiri, R., Little, I., Gutmark, E., Critser, P., Taylor, M., and Tretter, J. Effects of normal variation in the rotational position of the aortic root on hemodynamics and tissue biomechanics of the thoracic aorta. *Cardiovascular Engineering and Technology* (11 2019), 1–12.

[112] SURANA, A., GRUNBERG, O., and HALLER, G. Exact theory of three-dimensional flow separation. part 1. steady separation. *Journal of Fluid Mechanics 564* (2006), 57–103.

[113] Symonds, C. The circle of willis. *BMJ 1*, 4906 (1955), 119–124.

[114] Thoumine, O., Ott, A., and Louvard, D. Critical centrifugal forces induce adhesion rupture or structural reorganization in cultured cells. *Cell Motility 33*, 4 (1996), 276–287.

[115] Tousoulis, D., Kampoli, A.-M., Papageorgiou, T. N., Costas, and Stefanadis, C. The role of nitric oxide on endothelial function. *Current Vascular Pharmacology 10*, 1 (2012), 4–18.

[116] Touyz, R. M., Alves-Lopes, R., Rios, F. J., Camargo, L. L., Anagnostopoulou, A., Arner, A., and Montezano, A. C. Vascular smooth muscle contraction in hypertension. *Cardiovascular Research 114*, 4 (01 2018), 529–539.

[117] Uryash, A., Wu, H., Bassuk, J., Kurlansky, P., Sackner, M. A., and Adams, J. A. Low-amplitude pulses to the circulation through periodic acceleration induces endothelial-dependent vasodilatation. *Journal of Applied Physiology 106*, 6 (2009), 1840–1847. PMID: 19325024.

[118] van Tuijl, R. J., Ruigrok, Y. M., Velthuis, B. K., van der Schaaf, I. C., Rinkel, G. J. E., and Zwanenburg, J. J. M. Velocity pulsatility and arterial distensibility along the internal carotid artery. *Journal of the American Heart Association 9*, 16 (2020), e016883.

[119] Vestweber, D. Ve-cadherin. *Arteriosclerosis, Thrombosis, and Vascular Biology 28*, 2 (2008), 223–232.

[120] Villablanca, J. P., Duckwiler, G. R., Jahan, R., Tateshima, S., Martin, N. A., Frazee, J., Gonzalez, N. R., Sayre, J., and Vinuela, F. V. Natural history of asymptomatic unruptured cerebral aneurysms evaluated at ct angiography: growth and rupture incidence and correlation with epidemiologic risk factors. *Radiology 269*, 1 (2013).

[121] Vlak, M. H., Algra, A., Brandenburg, R., and Rinkel, G. J. Prevalence of unruptured intracranial aneurysms, with emphasis on sex, age, comorbidity,

country, and time period: a systematic review and meta-analysis. *The Lancet Neurology 10*, 7 (2011), 626–636.

[122] Vrselja, Z., Brkic, H., Mrdenovic, S., Radic, R., and Curic, G. Function of circle of willis. *Journal of Cerebral Blood Flow & Metabolism 34*, 4 (2014), 578–584. PMID: 24473483.

[123] Wang, L., Gorgey, A. S., Hsu, H.-Y., Li, X., and Xian, C. J. Effects of frequency and acceleration amplitude on osteoblast mechanical vibration responses: A finite element study. *BioMed Research International* (2016).

[124] Wehland, M., Ma, X., Braun, M., Hauslage, J., Hemmersbach, R., Bauer, J., Grosse, J., Infanger, M., and Grimm, D. The impact of altered gravity and vibration on endothelial cells during a parabolic flight. *Cellular physiology and biochemistry : international journal of experimental cellular physiology, biochemistry, and pharmacology 31* (03 2013), 432–51.

[125] White, C. R., Haidekker, M. A., Stevens, H. Y., and Frangos, J. A. Extracellular signal-regulated kinase activation and endothelin-1 production in human endothelial cells exposed to vibration. *The Journal of Physiology 555*, 2 (2004), 565–572.

[126] Willmarth, W. W. Pressure fluctuations beneath turbulent boundary layers. *Annual Review of Fluid Mechanics 7*, 1 (1975), 13–36.

[127] Wong, A., Llanos, P., Boroda, N., Rosenberg, S., and Rabbany, S. A parallel-plate flow chamber for mechanical characterization of endothelial cells exposed to laminar shear stress. *Cellular and Molecular Bioengineering 9* (10 2015).

[128] Xiao, Z., Zhang, Z., and Diamond, S. L. Shear stress induction of the endothelial nitric oxide synthase gene is calcium-dependent but not calcium-activated. *Journal of Cellular Physiology 171*, 2 (1997), 205–211.

[129] Xu, D., Varshney, A., Ma, X., Song, B., Riedl, M., Avila, M., and Hof, B. Nonlinear hydrodynamic instability and turbulence in pulsatile flow. *Proceedings of the National Academy of Sciences 117*, 21 (2020), 11233–11239.

[130] Yamaguchi, R., Tanaka, G., Liu, H., and Hayase, T. Fluid vibration induced in t-junction with double side branches. *World Journal of Mechanics 06* (01 2016), 169–179.

[131] Yamamoto, K., Akita, T., Ikeuchi, H., and Kita, Y. Experimental study of the flow in a helical circular tube. *Fluid Dynamics Research 16*, 4 (sep 1995), 237–249.

[132] Yang, S. T., Mayhan, W. G., Faraci, F. M., and Heistad, D. D. Endothelium-dependent responses of cerebral blood vessels during chronic hypertension. *Hypertension 17*, 5 (1991), 612–618.

[133] Yang, Z., Ge, H., Wang, C., Li, Z., Zhang, Q., and Wang, J. Repeated positive acceleration exposure exacerbates endothelial dysfunction in high-fat-diet-induced hyperlipidemic rats. *Archives of Medical Science 13*, 4 (2017), 937–946.

[134] Zhao, J., Hourigan, K., and Thompson, M. C. Flow-induced vibration of d-section cylinders: an afterbody is not essential for vortex-induced vibration. *Journal of Fluid Mechanics 851* (2018), 317–343.